GAS-PHASE THERMODYNAMICS OF HYDRAZINE CONTAINING COMPOUNDS AND IRON CLUSTER CATIONS: GUIDED ION BEAM AND THEORETICAL INVESTIGATIONS

by

Christopher Patrick McNary

A dissertation submitted to the faculty of
The University of Utah
in partial fulfillment of the requirements for the degree of

Doctor of Philosophy

Department of Chemistry

The University of Utah

December 2017

The University of Utah Graduate School

STATEMENT OF DISSERTATION APPROVAL

The dissertation of **Christopher Patrick McNary**

has been approved by the following supervisory committee members:

Peter B. Armentrout	, Chair	**8/18/2017** Date Approved
Michael D. Morse	, Member	**8/18/2017** Date Approved
Scott L. Anderson	, Member	**8/18/2017** Date Approved
Henry S. White	, Member	Date Approved
Ravi Chandran	, Member	**8/18/2017** Date Approved

and by **Cynthia J. Burrows**, Chair/Dean of

the Department/College/School of **Chemistry**

and by David B. Kieda, Dean of The Graduate School.

ABSTRACT

Guided ion beam tandem mass spectrometry (GIBMS) is used to probe the kinetic energy dependences of protonated hydrazine colliding with Xe, proton-bound hydrazine and unsymmetrical 1,1–Dimethylhydrazine (UDMH) clusters and protonated hydrazine and UDMH clustered with water colliding with Ar. The resulting cross sections are analyzed using a statistical model after accounting for internal and kinetic energy distributions, multiple collisions, and kinetic shifts to obtain 0 K bond dissociation energies (BDEs) for the threshold collision induced dissociation (TCID). The dominant dissociation pathways for protonated hydrazine ($N_2H_5^+$) and its perdeuterated variant ($N_2D_5^+$) were the observed endothermic non-adiabatic homolytic and heterolytic N–N bond cleavages forming $NH_3^+(^2A_2'') + NH_2(^2A_1)$ and $NH_2^+(^1A_1) + NH_3(^1A_1)$, respectively. For the proton-bound clusters, the primary dissociation pathways for $(N_2H_4)_nH^+$ where n = (2–4) and $(UDMH)_2H^+$ consists of a loss of hydrazine or UMDH unit, followed by the sequential loss an additional hydrazine at higher energies for $n > 2$. As to be expected, a similar trend is observed for the primary dissociation pathways for $(N_2H_4)H^+(H_2O)_n$ where n = (2 and 3) and $(UDMH)H^+(H_2O)$ where the losses of a water unit are followed by the sequential loss of a water unit for $n \geq 2$.

A larger GIBMS is used to probe the association reactions below 1 eV, of Fe_n^+ + CO where n = 4–17. All clusters where $n \geq 4$ form the Fe_nCO^+ association complex; the resulting cross sections are analyzed using a statistical model after accounting for internal

and kinetic energy distributions, multiple collisions, and kinetic shifts to obtain 0 K binding energies for CO binding to iron cluster cations. The probability of this reaction increases with cluster size until the absolute cross sections equal the collision limit for $n > 10$, with those for $n = 12$ and 14 exceeding the collision limit. For the largest clusters, the binding energies approach that of an extended Fe(111) surface, whereas the prominent higher energy feature correlates to binding energies for dissociatively chemisorbed C and O on an iron surface.

In Loving Memory of my Father, Sammy Allen McNary

TABLE OF CONTENTS

ACKNOWLEDGEMENTS

First and foremost, I thank my advisor, Dr. Peter B. Armentrout, for giving me space to learn on my own and direction when I needed help. Under his guidance, I developed a sense of professional confidence and an understanding that most problems can be solved with enough attention to detail, intelligence, and hard work.

I thank all the past and present members of the Armentrout group, especially Chris Hinton and Murat Citir, for giving me guidance my first couple of years in the group and for selflessly taking time to ensure I was properly trained on the instruments, Andrew F. Sweeney for being one of the best friends/co-workers a guy could ask for, and Rebecca Coates for always being there to talk to in dark times. I also thank my family, for their continued support over these long years. There is no doubt in my mind that had I not been blessed with a father who pushed me as hard as he did, or a mother who constantly made sure I was doing well over the years, I wouldn't be at the place I am in my life right now. I thank all the personnel in the machine and electronic shops for their hard work and tutelage, especially Dennis Romney, Tom Gudmundson, Dale Heisler, and Ron Jones. I would not have been able to accomplish this without their guidance. I also thank Dr. Anita M. Orendt for continuous help and support with the supercomputing nodes at the Center for High-Performance Computing (CHPC) at the University of Utah. Finally, I want to express my gratitude for being able to travel Europe in the name of science. France, Germany, and The Netherlands are all great places to visit and perform

world class science. I have experienced fruitful collaborations, lasting friendships, and learned the Dutch really like pickled herring.

Funding for this work came from the National Science Foundation, Grant CHE-1359769, CHE-1049580 and the Chemical Sciences, Geo-sciences, and Biosciences Division, Office of Basic Energy Science, U.S. Department of Energy, independent contracted work for ENSCO INC., and Extreme Science and Engineering Discovery Environment (XSEDE), Grant TG-CHE170012 for allocations on the large memory nodes at Pittsburgh Supercomputing Center at Carnegie Mellon University and San Diego Supercomputer Center at University of California San Diego.

CHAPTER 1

INTRODUCTION

1.1 Background

The first few chapters of this dissertation describe a comprehensive examination of protonated hydrazine and unsymmetrical 1,1–dimethylhydrazine (commonly known as UDMH), which was a successful project originating from the Air Force. Hydrazine and UDMH are used as fuels in some types of mono- and bipropellant rocket engines[1] and can have a deleterious effect on the environment when released into the atmosphere during rocket burns.[2] Protonated hydrazine, $N_2H_5^+$, is found to readily form in ion/molecule reactions in the ionosphere during launch and reentry of some spacecrafts.[1] Likewise, UDMH that is released into the atmosphere during rocket burns has been shown to exothermically react with atmospheric gases, such as ozone and hydroxyl radical, creating potentially toxic compounds such as methylhydroperoxide, methyldiazene, and diazomethane.[3] Hydrazine has potential as a clean liquid fuel storage system for hydrogen devices,[4,5] an oxygen scavenger in some boiler applications to protect against corrosion,[6] and a blowing agent in preparing polymer foams, and acts as a precursor to catalysts and pharmaceuticals.[7] Therefore, it is important to explore fundamental properties of the protonated monomers and clusters of hydrazine and UDMH in order to understand what impact these systems might have on the environment.

Previous studies to understand the monomers and clustering behaviors of these species have mostly focused on hydrazine,[8-14] whereas little information is known about the behavior of UMDH. Most of these studies are computational from which quantitative thermodynamics cannot be obtained, although mass-analyzed ion kinetic energy spectrometry (MIKES) was used to examine the metastable fragments of $(N_2H_4)_nH^+$ where n = 2–7. In that study, the average kinetic energy releases for the $(N_2H_4)_nH^+$ systems were obtained from the MIKES analysis of the Maxwell-Boltzmann-like kinetic energy release distributions (KERD). Further analysis of the KERDs yielded bond dissociation energies (BDEs) for each system. In addition, MIKES was utilized once again to examine the metastable fragments of $N_2H_5^+$ formed in the chemical ionization process, $H_3^+ + N_2H_4 \rightarrow N_2H_5^+ + H_2$ (exothermic by 4.43 ± 0.01 eV),[9] observing the dominant losses of H_2 and H, weak loss of NH, and homolytic N–N bond cleavage. Unfortunately, again no quantitative thermodynamics were obtained from this study.

In this work, we use guided ion beam tandem mass spectrometry (GIBMS) to quantitatively measure the kinetic energy dependence of protonated hydrazine colliding with Xe, the proton-bound hydrazine and UDMH clusters and protonated hydrazine and UMDH clustered with water colliding with Ar. GIBMS is a powerful technique for measuring thermodynamic properties of small molecules and hydrated species, as demonstrated previously in our lab.[15-24] The advantage of using the GIBMS technique over other methods is its precise control of the internal and kinetic energies of the reactant ion and neutral gas.[25-27] The resulting product intensities are converted to cross sections, which can effectively be thought of as reaction probabilities. The apparent threshold is defined as the minimum energy at which the product cross section gains

intensity. With the internal and kinetic energies of the reactants known, the 0 K BDEs can be extracted from these measured thresholds.

In the last chapter, we pivot from the hydrazine and UDMH systems to present another aspect of the GIBMS technique involving the kinetic energy dependences of the association reactions of iron cluster cations (Fe_n^+ where n = 4–17) with carbon monoxide (CO). The interaction of carbon monoxide with iron is technologically important for diverse reasons, including synthetic fuel production using Fischer-Tropsch (F-T) chemistry,[28] and for the catalytic growth of multi- and single-walled carbon nanotubes (SWNT).[29] In F-T synthesis, syngas (CO and H_2) reacts on the metal catalyst with alkanes being the most desirable products, although alkenes and alcohols are often formed as well. For SWNT synthesis, Smalley and co-workers[29] used a gas-phase reactor utilizing $Fe(CO)_5$ in the presence of a flow of carbon monoxide. At the catalytic conditions for nanotube growth, $Fe(CO)_5$ decomposes and forms iron clusters that serve as the catalytic centers for disproportionation of the CO feedstock in the Boudouard reaction, $Fe_n + 2\ CO \rightarrow Fe_nC + CO_2$.[30]

For this work, we found at energies below 1 eV, the n = 4–17 systems react exclusively to form Fe_nCO^+ complexes, even under single collision conditions. The observation of this reaction is interesting because the Fe_nCO^+ association complex always has sufficient energy to decompose back to reactants. Thus, the Fe_nCO^+ complexes have lifetimes that exceed their flight time through the instrument. Unlike TCID of a preformed Fe_nCO^+ complex, where collision with a nonreactive partner deposits a broad distribution of internal energies leading to dissociation, the association process forms Fe_nCO^+ complexes with well-defined distributions of internal energy and

angular momenta, and a cross section for formation determined by the ion-molecule collision probability. Thus, the dissociation lifetime of the association complex is governed primarily by only one adjustable parameter, the 0 K binding energy, $D_0(Fe_n^+\text{-CO})$.

1.2 Overview

An overview of the various instrumentation used in the present work is given in each chapter. An overview of the major modifications made to the instrumentation is given in Chapter 2. This includes a detailed description of the harsh-environment electrospray ionization source (HE-ESI) and the electrospray ionization–ion funnel–tandem hexapole (ESI/IF/T-HEX) source designed for the larger of the two GIBMS instruments. The experimental procedures, methods for converting the raw data into cross sections, statistical methods used to model those cross sections, and theoretical methods utilized are presented in each chapter.

Chapter 3 presents the non-adiabatic behavior in the homolytic and heterolytic bond dissociation of protonated hydrazine and its perdeuterated variant. The dominant dissociation pathways observed were the endothermic homolytic and heterolytic cleavages of the N–N bond. The analyses of the data used a statistical model that accounted for the internal and kinetic energy distributions, multiple collisions, and kinetic shifts to obtain 0 K BDEs for these covalently bonded species. Comparison with literature thermochemistry demonstrates that heterolytic bond cleavage yields the spin restricted excited NH_2^+ ($^1A_1$) + NH_3 ($^1A_1$) products and not the spin-forbidden ground NH_2^+ ($^3B_1$) + NH_3 ($^1A_1$) products, whereas homolytic bond cleavage leads to

dissociation to the excited NH_3^+ ($^2A_2''$) + NH_2 ($^2A_1$) product asymptote rather than the energetically favored NH_3^+ ($^2A_2''$) + NH_2 ($^2B_1$) asymptote. The rationale for the non-adiabatic behavior observed in the homolytic bond cleavage is revealed by detailed theoretical calculations of the relevant potential energy surfaces.

Chapter 4 presents the TCID studies of $(N_2H_4)_nH^+$ where n = 2−4 and $(UDMH)_2H^+$ colliding with Ar. The primary dissociation pathway for all reactants consists of loss of a single hydrazine (or UDMH) molecule followed by the sequential loss of additional hydrazine molecules at higher collision energies for n = 3 and 4. The experimental BDEs are compared to theoretical values determined at the B3LYP, M06, mPW1PW91, PBE0, MP2(full), and CCSD(T) levels of theory with and without empirical dispersion with a 6-311+G(2d,2p) basis set. The structures of all clusters are explored and exhibit extensive hydrogen bonding.

Chapter 5 presents the TCID of $(N_2H_4)H^+(H_2O)_n$, where n = 1 and 2, and of $(UDMH)H^+(H_2O)$. The primary dissociation pathway for all clusters is a loss of a single water molecule, which for n = 2 is followed by the sequential loss of an additional water molecule at higher collision energies. The experimental BDEs compare favorably to theoretical values determined at the B3LYP, M06, mPW1PW91, PBE0, MP2(full), and CCSD(T) levels of theory with a 6-311+G(2d,2p) basis set both with and without empirical dispersion. These calculations also allow visualization of the structures of these complexes, which are simple hydrogen bonded donor-acceptors.

Chapter 6 presents the energy dependences of size-selected Fe_n^+ cluster ions (n = 1–17) reacting with CO at low energies using a GIBMS equipped with a laser vaporization/supersonic expansion source. Below about 1 eV, all clusters with $n \geq 4$ form

the Fe_nCO^+ association complex. The probability of this reaction increases with cluster size until the absolute cross sections equal the collision limit for $n > 10$, with those for $n = 12$ and 14 exceeding the collision limit. The kinetic energy dependence and absolute magnitudes of these cross sections are analyzed to extract cluster–CO binding energies, which are found to progressively decrease with increasing cluster size, consistent with a simple Coulomb model. For the largest clusters, these binding energies approach that of an extended surface at shallow hollow sites, whereas a prominent higher energetic pathway correlates to the binding energies for dissociatively chemisorbed C and O on an iron surface.

1.3 Collaborative Work

An important aspect of obtaining a Ph.D. that is often overlooked in a competitive peer-reviewed environment is the ability to be collaborative with said peers. Even though second and co-authored journal articles are not included in this dissertation, it is important to reflect on those journal articles. As we all know, there are different levels of collaborative work, where countless hours could be spent mentoring a new co-worker to working side-by-side with a co-worker. These might consist of collecting data, performing high level calculations, or even finishing a stalled journal article. Throughout my graduate studies, publishing four first author[31-34] articles in journals of notable impact and being a part of five second or third author[27,35-38] journal articles reflects my achievements in graduate school and my commitment to friends, to peers, and to the Armentrout group. Of the non-first author journal articles, the most intriguing article is titled “How hot are your ions really? A threshold collision-induced dissociation study of

substituted benzylpyridinium ‘thermometer’ ions.”[27] Where the first absolute experimental BDEs for the main heterolytic bond cleavages of four benzylpyridinium ions were measured using TCID in a GIBMS and a very intuitive survival yield method was applied to determine the characteristic temperature of the ESI source prior to the thermalization region, confirming efficient thermalization of ions created from our ESI source. From that study, a follow-up examination of weaker bound para-substituted benzylpyridinium ions will be examined by similar methods, possibly obtaining a more accurate characteristic temperature of the ESI source. Next, infrared multiphoton dissociation (IRMPD) was utilized to spectroscopically identify predicted ground conformations of cysteine, methylated-cysteine,[35] serine,[36] or aspartic acid[37] bound to Zn^{2+} and Cd^{2+} at room temperatures. Finally, TCID of protonated azobenzene with Xe in a GIBMS was examined, where the analyses of the data are still going on.[38]

1.4 References

[1]J. A. Gardner, R. A. Dressler, R. H. Salter *et al.*, J. Phys. Chem. **96**, 4210 (1992).

[2]G. Lunn, E. B. Sansone, and L. K. Keefer, Environ. Sci. Technol. **17**, 240 (1983).

[3]E. C. Tuazon, W. P. L. Carter, A. M. Winer *et al.*, Environ. Sci. Technol. **15**, 823 (1981).

[4]M. Zhang, R. Cheng, Z. Chen *et al.*, Int. J. Hydrogen Energy **30**, 1081 (2005).

[5]S. G. Pakdehi, M. Salimi, and M. Rasoolzadeh, Res. Appl. Mech. Eng. **3**, 21 (2014).

[6]G. V. Buxton, and C. R. Stuart, J. Chem. Soc., Faraday Trans. **92**, 1519 (1996).

[7]J.-P. Schirmann, and P. Bourdauducq, in *Ullmann's Encyclopedia of Industrial Chemistry* (Wiley-VCH Verlag GmbH & Co. KGaA, 2000).

[8]W. Y. Feng, V. Aviyente, T. Varnali *et al.*, J. Phys. Chem. **99**, 1776 (1995).

[9]E. L. Øiestad, and E. Uggerud, Int. J. Mass Spectrom. Ion Processes **165-166**, 39 (1997).

[10]T. A. Beu, U. Buck, J. G. Siebers *et al.*, J. Chem. Phys. **106**, 6795 (1997).

[11]T. A. Beu, U. Buck, I. Ettischer *et al.*, J. Chem. Phys. **106**, 6806 (1997).

[12]E. M. Cabaleiro-Lago, and M. A. Ríos, J. Phys. Chem. A **103**, 6468 (1999).

[13]V. Dyczmons, J. Phys. Chem. A **106**, 5031 (2002).

[14]V. Dyczmons, J. Mol. Struct. **766**, 9 (2006).

[15]F. Muntean, and P. B. Armentrout, J. Chem. Phys. **115**, 1213 (2001).

[16]F. Muntean, and P. B. Armentrout, J. Phys. Chem. B **106**, 8117 (2002).

[17]F. Muntean, L. Heumann, and P. B. Armentrout, J. Chem. Phys. **116**, 5593 (2002).

[18]F. Muntean, and P. B. Armentrout, J. Phys. Chem. A **107**, 7413 (2003).

[19]D. R. Carl, R. M. Moision, and P. B. Armentrout, Int. J. Mass Spectrom. **265**, 308 (2007).

[20]T. E. Cooper, D. R. Carl, and P. B. Armentrout, J. Phys. Chem. A **113**, 13727 (2009).

[21]D. R. Carl, B. K. Chatterjee, and P. B. Armentrout, J. Chem. Phys. **132**, 044303 (2010).

[22]T. E. Cooper, and P. B. Armentrout, Chem. Phys. Lett. **486**, 1 (2010).

[23]A. F. Sweeney, and P. B. Armentrout, J. Phys. Chem. A **118**, 10210 (2014).

[24]A. F. A. Sweeney, P. B., Eur. J. Mass Spectrom. **21**, 497 (2015).

[25]K. M. Ervin, and P. B. Armentrout, J. Chem. Phys. **83**, 166 (1985).

[26]D. R. Carl, R. M. Moision, and P. B. Armentrout, J. Am. Soc. Mass Spectrom. **20**, 2312 (2009).

[27]J. E. Carpenter, C. P. McNary, A. Furin *et al.*, J. Am. Soc. Mass Spectrom. **28**, 1876 (2017).

[28]M. E. Dry, Catal. Today **71**, 227 (2002).

[29]M. J. Bronikowski, P. A. Willis, D. T. Colbert *et al.*, J. Vac. Sci. Technol., A **19**, 1800 (2001).

[30]P. Plonjes, P. Palm, G. B. Viswanathan *et al.*, Chem. Phys. Lett. **352**, 342 (2002).

[31]C. P. McNary, and P. B. Armentrout, Phys. Chem. Chem. Phys. **16**, 26567 (2014).

[32]C. P. McNary, and P. B. Armentrout, J. Chem. Phys. **145**, 214311 (2016).

[33]C. P. McNary, and P. B. Armentrout, J. Phys. Chem. A **120**, 9690 (2016).

[34]C. P. McNary, and P. B. Armentrout, J. Chem. Phys. **147**, 124306 (2017).

[35]R. A. Coates, C. P. McNary, G. C. Boles *et al.*, Phys. Chem. Chem. Phys. **17**, 25799 (2015).

[36]R. A. Coates, G. C. Boles, C. P. McNary *et al.*, Phys. Chem. Chem. Phys. **18**, 22434 (2016).

[37]G. C. Boles, R. A. Coates, C. P. McNary *et al.*, **submitted for publication** (2017).

[38]R. Mohammadreza, C. P. McNary, and P. B. Armentrout, **submitted for publication** (2017).

CHAPTER 2

INSTRUMENTATION AND INSTRUMENT MODIFICATIONS

2.1 Instrumentation

The instruments used in the present works are guided ion beam tandem mass spectrometers (GIBMS), shown in Figures 2.1 (EFRIM) and 2.2 (FREIDA), described in detail in each chapter and elsewhere.[1,2] Briefly, ions generated in the source regions of either instrument are then focused into the magnetic sector momentum analyzer for initial mass/charge (*m/z*) selection of the reactant ion of interest (EFRIM < 125 *m/z*, FREIDA < 4000 *m/z*) The reactant ions are then decelerated to a well-defined kinetic energy and injected into the rf octopole ion guide, which utilizes rf electric fields to create a potential well to trap ions in the transverse direction without affecting their axial energy. While the reactant ions are in the octopole, they pass through a collision cell that surrounds the octopole and contains the collisional gas at a low pressure. Products and remaining reactant ions are guided to the end of the octopole, where they are extracted and focused into a quadrupole mass filter for mass analysis (Extrel 3/4" Tri-Filter, 880 kHz, FREIDA; Extrel 3/4", 1.2 MHz, EFRIM). Finally, ions are detected by a 23 kV conversion dynode, secondary electron scintillation ion detector,[3] and the signal is processed using standard pulse counting techniques. In the present works, the ions are generated by either using electrospray ionization (ESI) of 10^{-2}–10^{-4} M solutions or by a laser ablation/vaporization

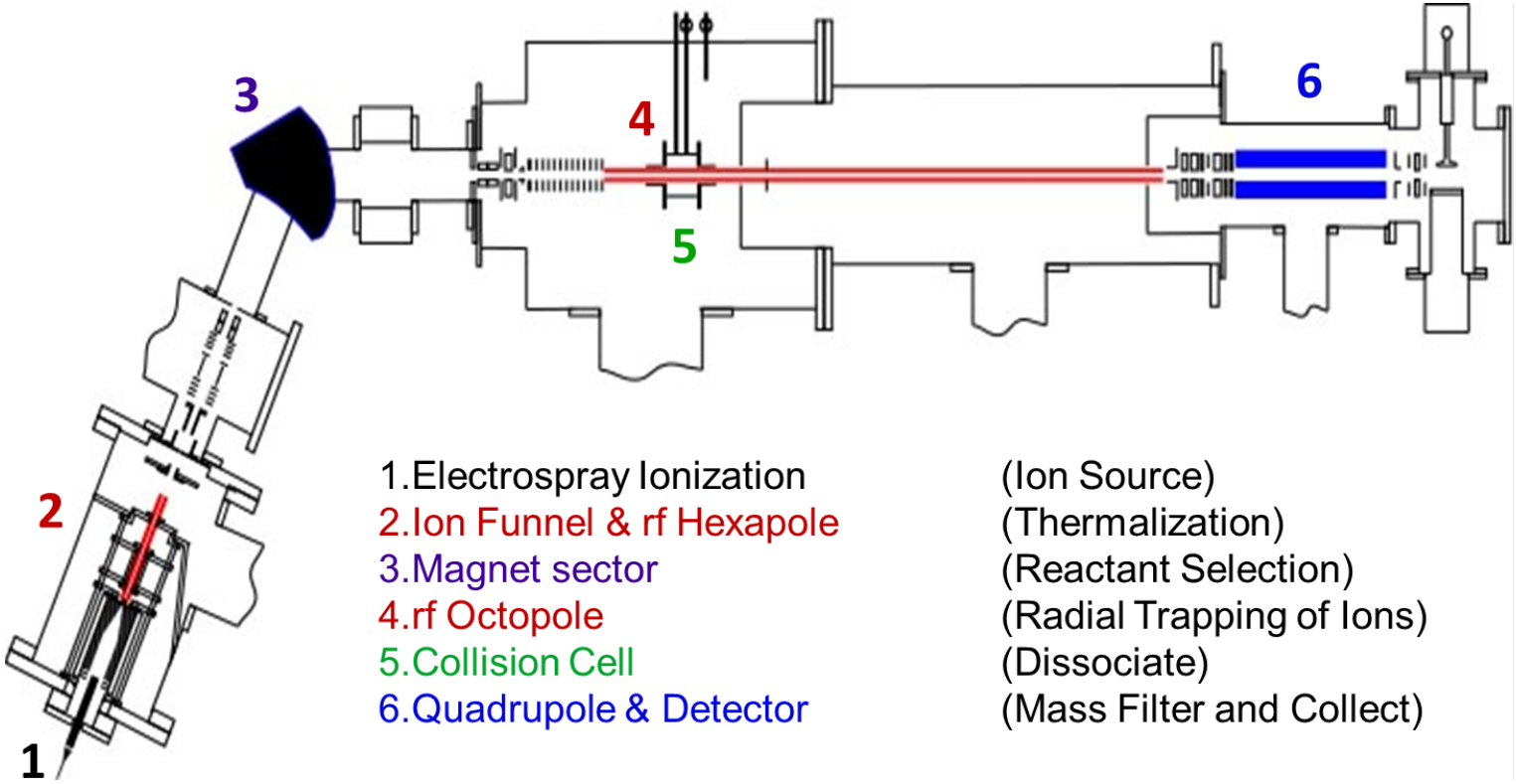

Figure 2.1. Schematic diagram of EFRIM, operating as an ESI-GIBMS.

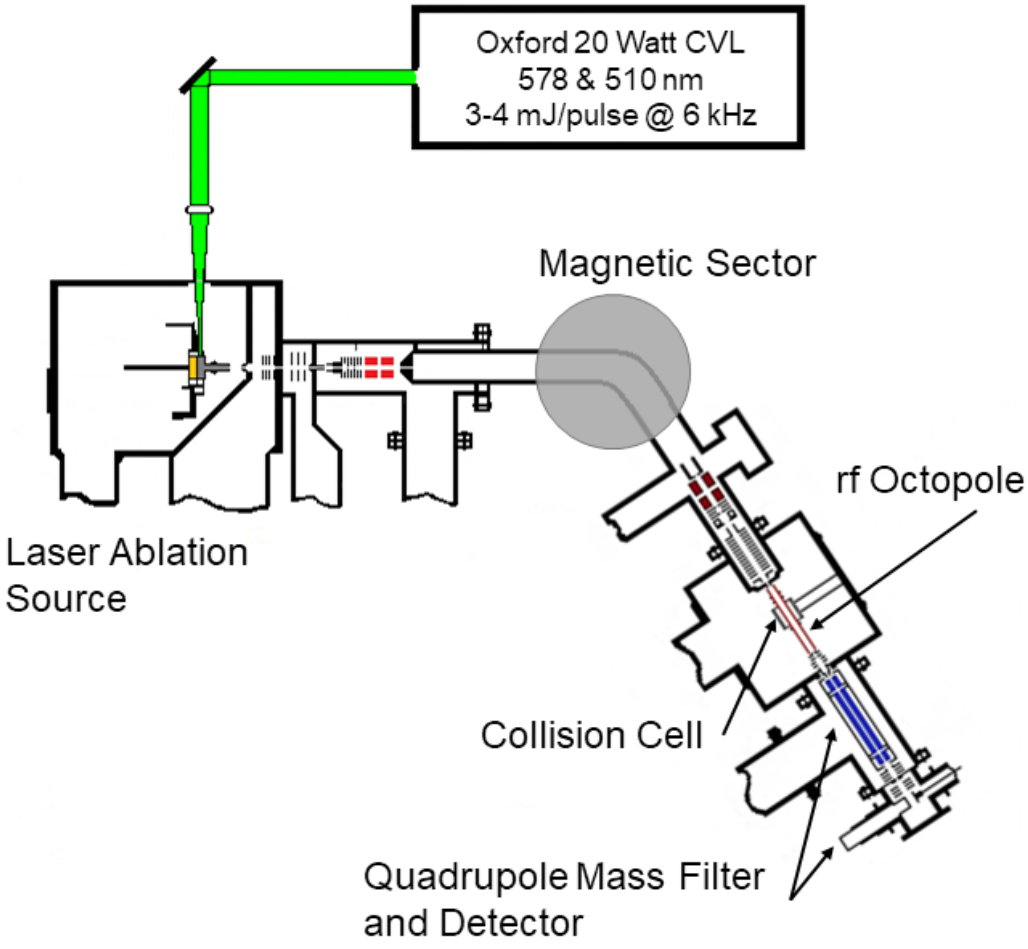

Figure 2.2. Schematic diagram of FREIDA, with the laser ablation/vaporization source attached.

source. This section describes the modifications made to the previous ESI source and provides details about the ESI–ion funnel–tandem hexapole source developed for the larger of the two instruments, FREIDA. The former modification was essential to accomplish the research performed for this Ph.D. dissertation.

2.2 Harsh Environment Electrospray Ionization Source

A harsh environment (HE) ESI source developed for use with the GIBMSs is described. The presented modifications to the existing ESI source were designed to protect the user from potentially toxic compounds and by-products that can be formed from nebulizing aqueous compounds, such as the ones used in Chapters 3–5. Emphasis was placed on maintaining the four important ESI characteristics: 1) high intensity, 2) stable signal, 3) well-defined energies, kinetic and internal, and 4) usability. In order to accomplish these objectives, the internal components of the existing ion funnel–hexapole assemblies were not altered,[4] whereas ESI support flange, capillary entrance cap (EC), capillary , and capillary heater (internal) were modified to accept a concentric designed ESI needle carrier, shown in Figure 2.3. The key element to the HE-ESI is the concentric Lexan shroud that protects the users from potentially toxic vapor. Here, the volume of gas contained within the shroud is constantly evacuated into the exhaust system at a rate of 10 L/min by a media transfer pump.

2.2.1 Supports and Housing

Starting from the ESI flange, two machined holes were drilled and bottom tapped to 3/8" - 16 threads per inch (TPI) at ±30º off vertical centerline with 3.0" between

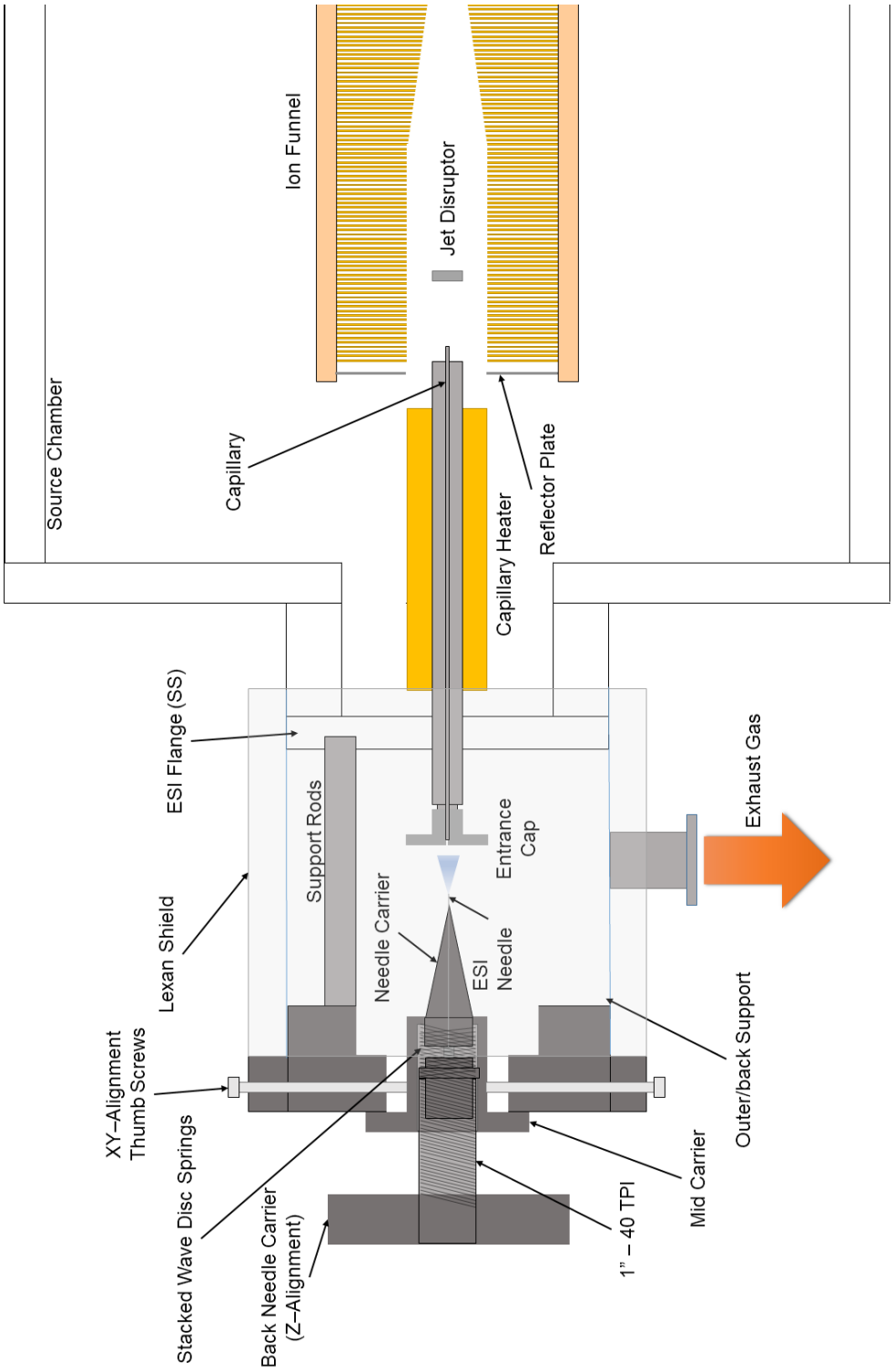

Figure 2.3. Schematic diagram of the harsh environment electrospray ionization source designed for the GIBMS.

centers (BC). These tapped holes accept two machined 6061 grade 3/8" aluminum support rods that hold the outer/back support as rigid as possible. Using these supports, the outer/back support is mounted with two 1/4"–20 TPI bolts and kept parallel to the EC, ensuring concentric alignment between the ESI needle and EC. The outer/back support for the HE-ESI was designed out of PVC because the material is inexpensive, easy to machine, and has excellent insulating properties, $> 10^{16}$ Ω/cm, while retaining structural rigidity. To control the XYZ translations, a spring loaded mid carrier was designed to allow a maximum of ~0.78" of XY circular movement around the EC and a maximum of ~1.9" of travel in the Z direction (distance between the ESI needle and EC). The XY translations are controlled by nylon thumb screws while the Z-axis is adjusted by a custom 1"–40 TPI PVC bolt (back needle carrier). These adjustments allow fine spatial tuning of the needle relative to the EC. The use of stacked wave disc springs, available from McMaster-Carr, ensures the needle carrier is under tension in the Z-direction, which removes any vibrational noise that could affect the experiment.

2.2.2 Electrospray Needle Carriers

There is one PVC and three 3-D printed Nylon versions of the needle carriers available; the latter versions include drying and/or nebulizing gas ports. The PVC version is of a tool-less design where the front and back halves are internally supported by 316 stainless steel (SS) VALCO fittings available from VICI (Valco Instruments Company Inc.). Figure 2.4 shows a detailed cross sectional view of the PVC needle carrier. A custom double ended Microtight™ to 1/16" Valco ferrule was designed and machined in-house. This ferrule bridges the gap between the Microtight™ 0.005" ID sleeve and the

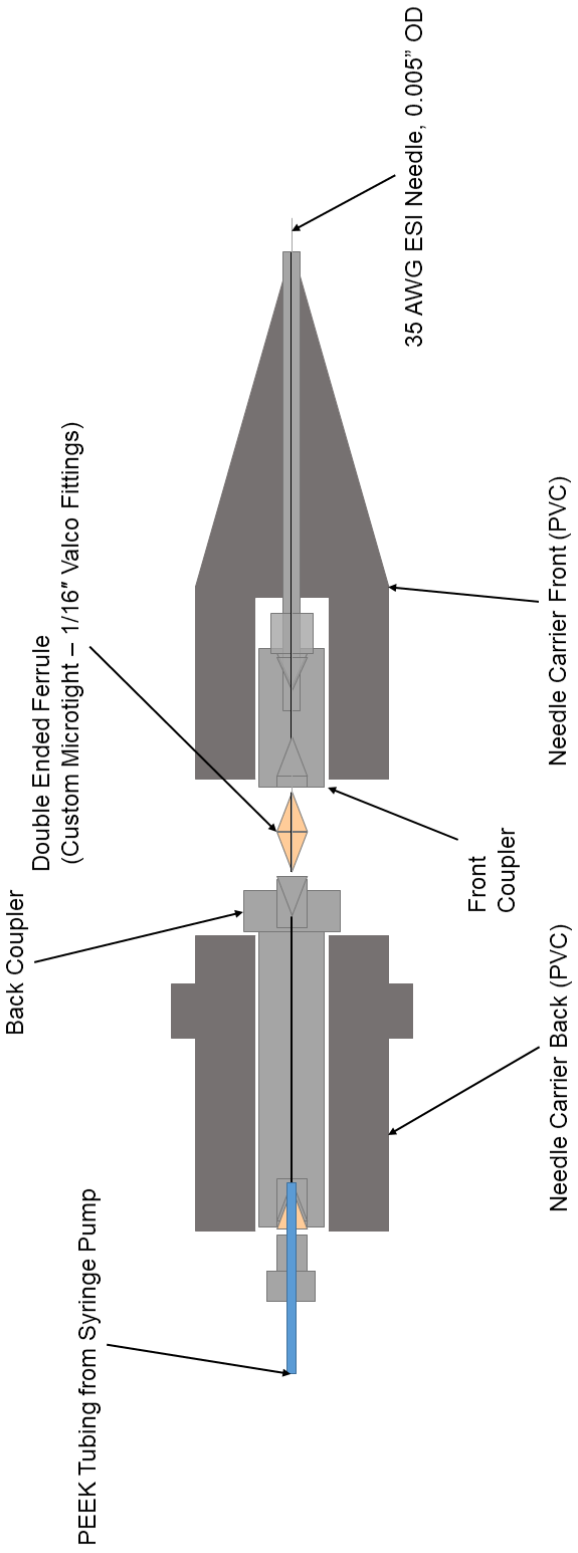

Figure 2.4. Cross sectional view of the PVC needle carrier

1/16" Valco fittings that are used to secure the 35 gauge 316 SS, 0.005" OD: 0.002" ID, ESI needle (ESN) in the assembled PVC needle carrier. Using this idea of an internal Valco support, three 3-D printed needle carriers were designed and printed in-house at the J. Willard Marriot Library at $3–$10 per carrier; this price difference was largely dependent on internal wall density of the carriers. The three different needle carrier versions are shown in Figure 2.5. The first version (V1) has no gas ports, while the second and third versions (V2 and V3) have gas ports, which were made possible by 3-D printing technologies. The internal Valco fittings are similar to that of the PVC version, where the Valco fittings support and hold the needle, while the outer nylon jacket is kept in place by the mid carrier. The addition of the drying and nebulizing gas ports add versatility to the system. Some biological systems may require the added benefit of a nebulizing and/or drying gas. Yet, these were not required for the research performed in Chapters 3–5.

Using one of the needle carriers, the ESI solution is then sprayed and transferred into the vacuum region by applying a 2–4 kV positive potential between the ESN and a 316 grade stainless steel EC with an inlet diameter of 0.010" followed directly by a 6.125" long by 0.040" ID electro-formed nickel capillary with an OD of 0.063". Such tubing is readily available from VICI, comes in standard ID's ranging from 0.005"–0.040," and has a near mirror inner finish. The 0.063" OD capillary tubing is held in place by a capillary holder, which is electrically isolated from earth and serves as a mount for the capillary heater. The capillary heater is a custom-machined 1/2" OD copper sleeve with a 0.375" ID through hole offset by 0.125" from center to allow placement of the 1/8" 24 Watt resistive heater, readily available from ThorLabs. An OMEGA thermocouple

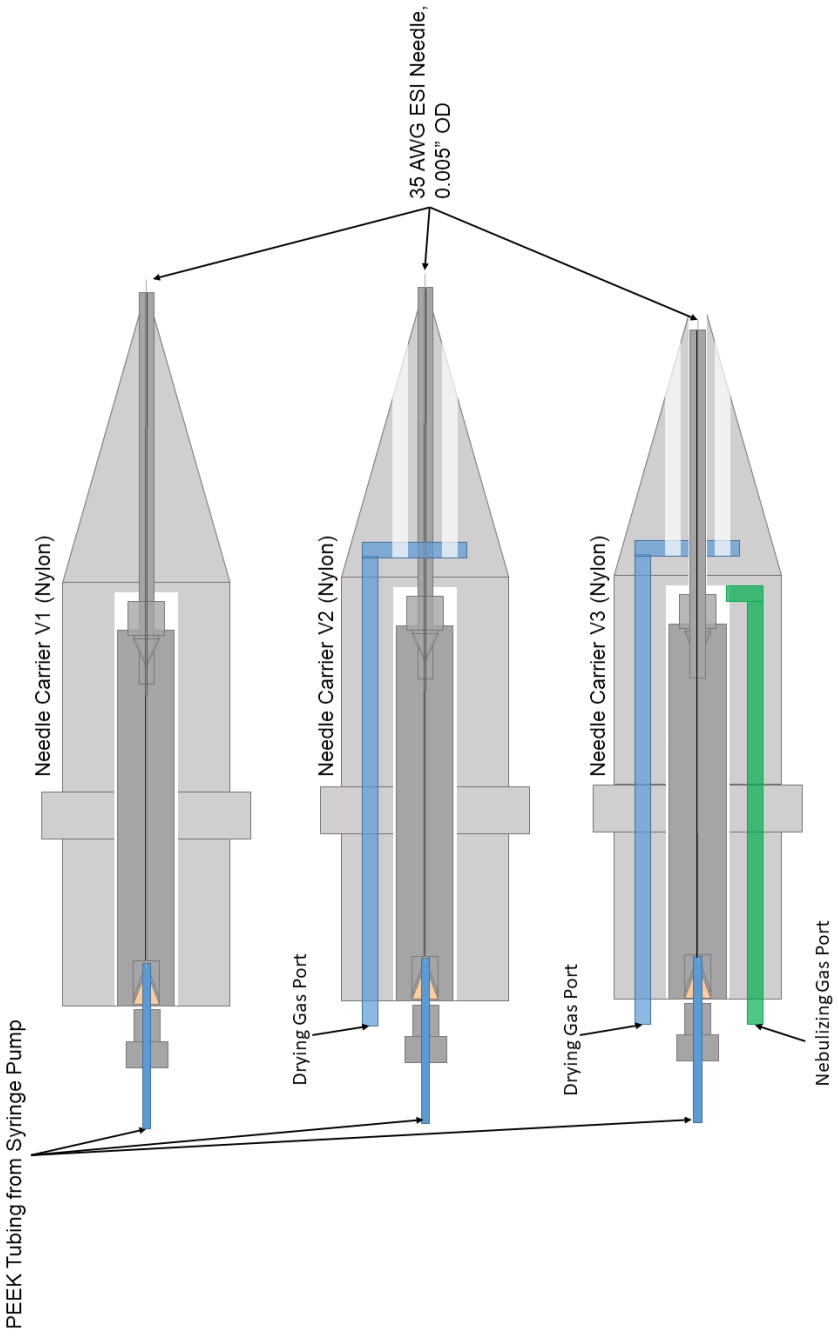

Figure 2.5. Cross sectional view of the three 3D printed versions of the needle carriers.

controller with a precision of 0.1 ºC controls a 0–140 VAC Variac (set at 24VAC), thus allowing the capillary to be heated from room temperature to 200 ºC. At the end capillary, an 88-plate ion funnel and a hexapole ion guide operating at 5.5 MHz collect and focus the ions into the GIBMS where the ions of interest undergo the experiments, as presented in Chapters 3–5.

2.3 Electrospray Ionization–Ion Funnel–Tandem Hexapole Source

2.3.1 Overview

A schematic overview of the ESI/ion funnel/hexapole/hexapole (ESI/IF/T-HEX) source developed for use with the larger of the two GIBMS instruments is shown in Figure 2.6. This source was designed after and improved upon the existing ESI/IF/HEX source on EFRIM, which is described elsewhere.[4,5] Similar to the HE-ESI described above, this source was designed to reproduce four key characteristics: high intensity, signal stability, well-defined energies, kinetic and internal, and usability, while retaining exchangeability between the two instruments. From atmosphere, four 304 SS alignment pins were designed to allow easy alignment between the rear flange and the skimmer gate valve when installing the ESI/IF/T-HEX apparatus into the instrument's source box. Identical mounting holes to that of EFRIM's source were drilled and tapped into the rear flange, allowing the in-house built ESI sources to be easily exchanged between the two instruments. The ions emitted from the spray are transferred into the vacuum region through a 316 grade SS inlet cap with an inlet diameter of 0.010" followed directly by a 6.125" long by 0.020" ID 316 SS capillary with an OD of 0.063". Such tubing is readily available through the Vita Needle Company. The 0.063" capillary tubing is placed within

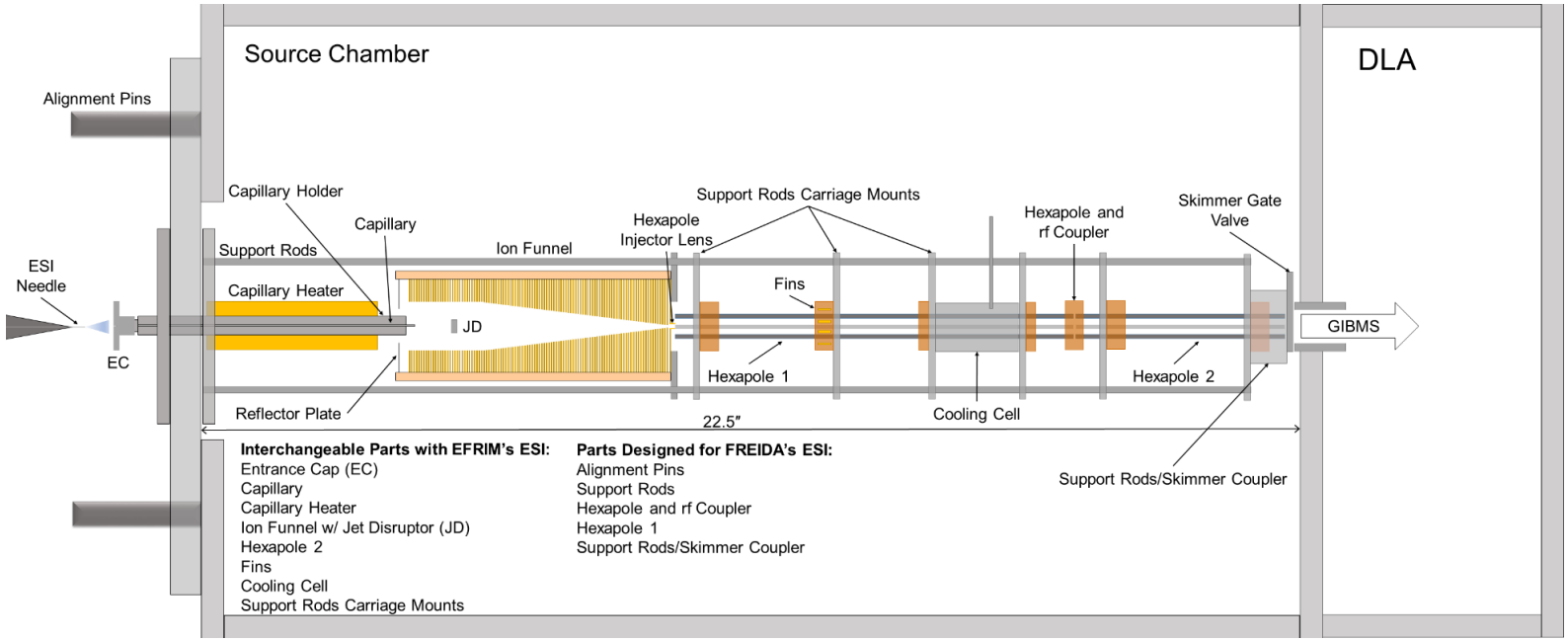

Figure 2.6. Schematic diagram of the electrospray ionization–ion funnel–tandem hexapole (ESI/IF/T-HEX) source designed for the larger of the two GIBMSs: ESI needle consisting of 35 gauge 316 stainless steel tubing. Ions emitted by the ESI are transferred into the first vacuum region, through a 0.020" ID 316 stainless steel capillary tubing held in place by the capillary holder. Ions are collected by the ion funnel and transferred into the first hexapole by the hexapole injector lens, where the ions are trapped radially and drift to the second hexapole where they are extracted by the skimmer and transferred into the second vacuum region (DLA) and enter the GIBMS.

the capillary tubing holder, machined from 0.375" OD and 0.0625" ID by 6.00" length, (high pressure tubing from VICI). The capillary holder is then held in place by fittings made of PEEK thermoplastic. The use of PEEK allows the entire capillary to be biased independently and heated to a temperature around 200 ºC. The temperature of the capillary and capillary holder is controlled similar to the method described above. At the end of the capillary, prior to the IF, sits a reflector plate that is independently electrically controlled and designed to keep ions from escaping out of the entrance of the IF.

2.3.2 Ion Funnel and its Power Source

Each plate of the IF requires a combination of rf and dc voltages. These voltages are applied through a custom printed circuit board (PCB) from an inexpensive vender (ExpressPCB), previously designed in house to fit on a double sided PCB board.[4] Both rf and DC components are applied to each plate of the IF through a single electrical connection. The surface mounted resistors (200 kΩ, 1/8 Watt, Size 1206, Allied Electronics) and capacitors (C, 0.01 μF, 100 V, Size 1206, Allied Electronics) are affixed to the PCB. The linear voltage gradient across the IF plates are controlled by resistors and the DC voltages applied to the first plate (DC^+) and last plate (DC^-). Note, both DC^+ and DC^- voltages are positive with respect to earth where the voltage applied to $DC^+ > DC^-$, in essence "pulling" the ions towards the last plate (more negative) of the IF. The typical ion funnel conditions are DC^+ = +15–20 VDC and DC^- = +5–10 VDC.

The rf voltages that are applied to the IF is created using a sine wave output from a 25 MHz arbitrary wave form generator (Agilent, model 33210A) and amplified with an rf amplifier (Mini Circuits, model LZY-22+). The rf signal from the amplifier is split into

equal and opposite phases with a custom designed 50 ohm trifilar-wound ferrite-core impedance matched balun transformer. The balun consists of two stacked T-350-77 toroids (Amidon Associates) wrapped with 16 gauge copper core magnet pickup wire. An adjustable 10–1000 μH (L) inductor was added to impedance match the capacitance generated by the parallel plates of the IF and to that of ground. Without the added inductor, the power generated by the amplifier would be reflected back to the output of the amplifier, causing the protection circuit of the amplifier to trigger and decrease power output. The use of a different rf amplifier (ENI, model 2100L) can be implemented with or without the impedance matching inductor because the ENI amplifier is a simply designed to handle reflected power better. Note, if the impedance matching inductor is used with the ENI amplifier, the IF might heat up due to power sloshing between the L and C components of the circuit. With either of the rf amplifiers, this circuit is capable of driving the IF at roughly 80 V peak to peak at 1.2 MHz and 35 V peak to peak at 2.0 MHz. Typical operating rf peak to peak voltage is around 20 V at 1.2 MHz.

2.3.3 Tandem Hexapole Ion Guide

The tandem hexapole ion guide (6-pole) consists of six 0.0125" centerless ground 303 SS rods (McMaster-Carr), 8.750" in length (hex 1) and 6.00" in length (hex 2), equally spaced on a 0.375" BC, and capacitively coupled together via two 0.01 μF 1 kV ceramic vacuum grade capacitors. Each rod has several 0-80 tapped holes in various locations, center-lined over the length of each rod. These rods are held in place and centered using custom sized 0-80 screws inserted through several machined nylon disks and two sets of 316 SS disks that supply the rf and DC voltages to the sets of hexapoles.

Both nylon and SS disks are relief cut and encircle roughly 0.015" of the rod diameter to allow axial and electrical tolerances between the six rods. The nylon disks serve two purposes; they hold the hexapoles concentric to the support carriage mounts and hold each of the six rods exactly 0.375" BC. A special nylon coupler between the hexapoles holds the exit of the first hexapole and entrance of the second hexapole to within 0.005" of the centerline, ensuring proper alignment, and minimizing the possibility of rf phase-mismatch between the set of hexapoles. The nylon coupler also serves as a place to mount the capacitors and allows the hexapoles to be independently biased. At the end of the second hexapole sits another special nylon coupler that serves as a limiting aperture between the source region and the first differential region (DLA).The coupler also ensures proper alignment for the entire tandem hexapole assembly with 0.010" spacing from the skimmer gate valve. The skimmer gate valve is electronically isolated from ground by a PVC coupler and, if needed, can be treated as a DC “extraction” lens into DLA. From there, the remaining lens train guides the ions into the GIBMS.

2.4 References

[1]K. M. Ervin, and P. B. Armentrout, J. Chem. Phys. **83**, 166 (1985).

[2]F. Muntean, and P. B. Armentrout, J. Chem. Phys. **115**, 1213 (2001).

[3]N. R. Daly, Rev. Sci. Instrum. **31**, 264 (1960).

[4]R. M. Moision, and P. B. Armentrout, J. Am. Soc. Mass Spectrom. **18**, 1124 (2007).

[5]D. R. Carl, R. M. Moision, and P. B. Armentrout, J. Am. Soc. Mass Spectrom. **20**, 2312 (2009).

CHAPTER 3

NON-ADIABATIC BEHAVIOR IN THE HOMOLYTIC AND HETEROLYTIC BOND DISSOCIATION OF PROTONATED HYDRAZINE: A GUIDED ION BEAM AND THEORETICAL INVESTIGATION

3.1 Abstract

Threshold collision-induced dissociation (TCID) using a guided ion beam tandem mass spectrometer was performed on protonated hydrazine and its perdeuterated variant. The dominant dissociation pathways observed were endothermic homolytic and heterolytic cleavages of the N–N bond. The data were analyzed using a statistical model after accounting for internal and kinetic energy distributions, multiple collisions, and kinetic shifts to obtain 0 K bond dissociation energies (BDEs). Comparison with literature thermochemistry demonstrates that both channels behave non-adiabatically. Heterolytic bond cleavage yields $NH_2^+ + NH_3$ products but the NH_2^+ fragment is in the spin-restricted excited $^1A_1$ state and not the spin-forbidden ground $^3B_1$ state; whereas homolytic bond cleavage leads to dissociation to the $NH_3^+ + NH_2$ product asymptote with NH_2 in its excited $^2A_1$ state rather than the energetically favored $^2B_1$ state. The rationale for the non-adiabatic behavior observed in the homolytic bond cleavage is revealed by

---

Reprinted from C. P. McNary, and P. B. Armentrout, J. Chem. Phys. 147, 124306 (2017).
With permission from AIP Publishing.

detailed theoretical calculations of the relevant potential energy surfaces and the relevant occupied valence molecular orbitals. These calculations suggest that the non-adiabatic behavior results from conservation of the s and p character of the lone pair and binding electrons on the nitrogen atoms.

3.2 Introduction

Hydrazine, used as a fuel for some types of mono- and bi-propellant rocket engines,[1] can have a deleterious effect on the environment when released into the atmosphere during successful and unsuccessful rocket burns.[2] In addition, protonated hydrazine, $N_2H_5^+$, forms readily in ion/molecule reactions in the ionosphere and during launch and reentry of some spacecraft.[1] Interestingly, hydrazine has also been used as an oxygen scavenger in boiler applications to protect against corrosion,[3] has potential as a clean liquid fuel storage system for hydrogen devices,[4,5] has been used as a blowing agent in preparing polymer foams, and acts as a precursor to catalysts and pharmaceuticals.[6] Therefore, it is of interest to explore the stability and chemistry of $N_2H_5^+$ at the fundamental level to understand fully its chemical properties.

Øiestand and Uggerud used mass-analyzed ion kinetic energy spectrometry (MIKES) to examine the metastable fragments of $N_2H_5^+$ formed in the chemical ionization process, $H_3^+ + N_2H_4 \rightarrow N_2H_5^+ + H_2$ (exothermic by 4.43 ± 0.01 eV).[7] They observed the dominant losses of H_2 and H, weak loss of NH, and homolytic N–N bond cleavage, given by reactions (3.1)–(3.4), respectively, where each reaction includes its heat of reaction, Δ_rH_0 (eV) calculated from the heats of formation (Δ_fH_0) listed in Table 3.1.[8-16]

Table 3.1. Standard enthalpies of formation at standard state, proton affinities (PA), and ionization energies (IE) for select species found in literature in eV.

Species	Δ_fH_0[a]	Δ_fH_{298}[a]	PA[b]	IE[c]
$(N_2H_4)H^+$ ($^1A'$)	8.16 ± 0.03[d]	8.03 ± 0.03[d]		
$N_2H_4^+$	9.198 ± 0.005	9.055 ± 0.005		
N_2H_4 ($^1A'$)	1.159 ± 0.005	1.012 ± 0.005	8.84 ± 0.03	8.039 ± 0.007
$N_2H_3^+$	10.042 ± 0.009	9.925 ± 0.009		
N_2H_3	2.439 ± 0.009	2.328 ± 0.009		7.603 ± 0.012
N_2H_2	2.149 ± 0.005	2.075 ± 0.005	8.32 ± 0.03	
NH_4^+ ($^1A_1$)	6.665 ± 0.002 6.59 ± 0.03[d]	6.548 ± 0.002 6.54 ± 0.03[d]		
NH_3 ($^1A_1$)	-0.3997 ± 0.0003	-0.4721 ± 0.0003	8.85 ± 0.03 8.873 ± 0.002[e]	10.186 ± 0.001
NH_3^+ ($^2A_2''$)	9.7867 ± 0.0003	9.7146 ± 0.0003		
NH_2 ($^2B_1$)	1.958 ± 0.001	1.928 ± 0.001	8.10 ± 0.03 8.009 ± 0.001[e]	11.168 ± 0.001 ($^3B_1$) 12.436 ± 0.001 ($^1A_1$)[f]
NH_2 ($^2A_1$)	3.38 ± 0.01[g]	3.35 ± 0.01[g]		
NH_2^+ ($^3B_1$)	13.127 ± 0.001	13.105 ± 0.001		
NH_2^+ ($^1A_1$)	14.394 ± 0.002[h]	14.364 ± 0.002[h]		
NH ($^3\Pi$)	3.718 ± 0.002	3.718 ± 0.002		13.476 ± 0.003
NH ($^1\Pi$)	5.279 ± 0.002	5.279 ± 0.002		11.915 ± 0.003
NH^+	17.194 ± 0.003	17.204 ± 0.003		
H (^2S)	2.239035	2.259390		13.598434
H^+	15.83747	15.85782		

[a] Values taken from Refs. 8-10 unless otherwise specified. [b] Proton affinities from Ref. 14 unless otherwise specified. [c] Derived using the $\Delta_fH_0(A^+)$ - $\Delta_fH_0(A)$, unless otherwise specified. [d] Derived using the $\Delta_fH(A)$ + $\Delta_fH(H^+)$ – PA(A), with PA from Ref 14. [e] Derived using $\Delta_fH(H^+)$ - $\Delta_fH(AH^+)$ + $\Delta_fH(A)$ with values from Ref. 8-10. [f] IE from Ref. [16]. [g] Derived using $\Delta_fH(NH_2)$ + excitation energy of 1.42 ± 0.01 eV from Ref. [15]. [h] Derived using $\Delta_fH(NH_2(^2B_1))$ + IE from Ref. [16].

$N_2H_5^+ \rightarrow N_2H_3^+ + H_2$	(1.88 ± 0.03)	(3.1)
$\rightarrow N_2H_4^+ + H$	(3.28 ± 0.03)	(3.2)
$\rightarrow NH_4^+ + NH\ (^3\Pi)$	(2.22 ± 0.03)	(3.3a)
$\rightarrow NH_4^+ + NH\ (^1\Pi)$	(3.78 ± 0.03)	(3.3b)
$\rightarrow NH_3^+\ (^2A_2'') + NH_2\ (^2B_1)$	(3.58 ± 0.03)	(3.4a)
$\rightarrow NH_3^+\ (^2A_2'') + NH_2\ (^2A_1)$	(5.01 ± 0.03)	(3.4b)
$\rightarrow NH_2^+\ (^3B_1) + NH_3\ (^1A_1)$	(4.57 ± 0.03)	(3.5a)
$\rightarrow NH_2^+\ (^1A_1) + NH_3\ (^1A_1)$	(5.83 ± 0.03)	(3.5b)

Note that because the $N_2H_5^+$ ions are formed with an internal energy near 4.43 eV, the heterolytic N–N bond cleavage pathways, reactions (3.5a) and (3.5b), were not observed. In addition to the experimental work, extensive *ab initio* quantum chemical calculations including the potential energy surfaces (PESs) for the observed reactions were conducted by these authors.

In previous studies, we used threshold collision-induced dissociation (TCID) in a guided ion beam tandem mass spectrometer (GIBMS) to quantitatively investigate the thermochemistry of proton-bound hydrazine and unsymmetrical 1,1–dimethylhydrazine (UDMH) clusters, and $N_2H_5^+$ and (UDMH)H^+ bound to water.[17,18] Analyses of the kinetic energy dependent TCID cross sections successfully yielded 0 K bond dissociation energies (BDEs) for those noncovalently bound complexes. Building on those efforts, the present work uses GIBMS to measure the kinetic energy dependences of the TCID cross sections for $N_2H_5^+$ and $N_2D_5^+$, which are analyzed to yield thresholds for dissociation. This thermochemistry is then compared to literature values and to results computed at several levels of theory, which are also used to thoroughly explore the possible reaction

pathways of these simple species.

3.3 Experimental and Theoretical Methods

3.3.1 Instrumentation

$N_2H_5^+$ and $N_2D_5^+$ were created from a 0.1 M solution of hydrazine in HPLC grade water (hydrazine in D_2O for $N_2D_5^+$) using electrospray ionization (ESI) techniques. The solution was advanced at a rate of 100–300 μL/h through a 35 gauge 304 stainless steel needle that had an applied voltage of ~2.5 kV. Once in the gas phase, ions entered the vacuum system through a stainless steel inlet cap with an inlet diameter of 0.010″ followed directly by a 6.125″ long by 0.040″ diameter electro-formed nickel capillary that was heated to a temperature of 120 ºC in order to desolvate large droplets. An 88 plate radio frequency (rf) ion funnel (IF) with superimposed DC gradient field, copied from a design described in detail elsewhere,[19-21] collected and focused the ions to increase signal intensity.[22] The voltage bias between the first and last plate of the ion funnel was kept below 20 V to minimize heating of the ions. At the end of the funnel, the ions entered an rf-only hexapole with rf amplitudes typically set at 250 V peak to peak centered around ground. Here, the ions underwent cooling by $>10^5$ thermalizing collisions with ambient gas (largely air and the water solvent). This ensured ions beyond the hexapole were well-defined by a Maxwell–Boltzmann distribution of rovibrational states at room temperature, as verified by previous work.[22-29]

Ions generated in the ESI/IF/hexapole source then entered the guided ion beam tandem mass spectrometer[30] where they were focused into a magnetic sector momentum analyzer for initial mass selection. These reactant ions were decelerated to a well-defined

kinetic energy and injected into a rf octopole ion guide[31] where they passed through a collision cell containing Xe at low pressures. The product and remaining reactant ions were guided to the end of the octopole, where they were extracted, mass selected using a quadrupole mass filter in high resolution mode, and detected using a Daly detector.[32]

3.3.2 Data Analysis

Acquiring accurate thermodynamic information from TCID data requires diligent consideration of many experimental factors that convolute the raw data. These factors include the internal and kinetic energy distributions of the ionic and neutral reactants, lifetime effects that arise from a finite experimental time window, the probability of multiple collisions, and competition from other chemical processes.

Measured intensities of the reactant and product ions were first corrected for dissociation outside the collision cell as well as background noise by measuring their intensities with and without gas in the collision cell. The intensities were then converted to absolute cross sections using a Beer–Lambert equation analogue, as described elsewhere.[30] The energy of the reactants was converted from the lab frame voltage of the ion, V_{lab}, to the center-of-mass energy, E_{CM}, using $E_{CM} = V_{lab}m/(m+M)$ where m is the mass of the reactant neutral and M is the mass of the reactant ion. The kinetic energy distribution of the ions was determined using a retarding potential analysis,[30,33] which also allows the absolute zero of the energy to be obtained. Experiments were conducted at three pressures of Xe gas, ~0.1, 0.2, and 0.4 mTorr. The cross sections at each pressure were used to linearly extrapolate to a zero pressure cross section, which rigorously represents a single collision event.[34]

The kinetic energy dependent CID cross sections for reaction channel *j* were modeled using the empirical model shown as follows:

$$\sigma_j(E) = \sigma_{0,j} \sum_i g_i (E + E_i - E_{0,j})^N / E \quad (3.6)$$

where E is the relative collision energy, $\sigma_{0,j}$ is an energy independent scaling factor, $E_{0,j}$ is the reaction threshold at 0 K, N describes the energy deposition function,[33] and the summation is over the rovibrational states of the reactant ion having energies E_i and populations g_i, where $\Sigma g_i = 1$. Rovibrational states taken from quantum chemical calculations of the ground states were directly counted using the Beyer–Swinehart–Stein–Rabinovitch algorithm[35-37] and were assigned populations on the basis of a Maxwell–Boltzmann distribution at 300 K. For large reactants, the number of accessible rovibrational states can be large enough that dissociation lifetimes near the threshold energy can be longer than the experimental time-of-flight, $\tau \sim 5 \times 10^{-4}$ s,[33] which shifts the apparent dissociation thresholds to higher energies. This kinetic shift was accounted for using Rice–Ramsperger–Kassel–Marcus (RRKM) statistical theory[38-40] for unimolecular dissociation and is incorporated into the cross section model, as follows:

$$\sigma_j(E) = \left(\frac{N\sigma_{0,j}}{E}\right) \sum_i g_i \int_{E_{0,j}-E_i}^{E} P_d \left[\frac{k_j(E^*)}{k_{tot}(E^*)}\right] (E - \varepsilon)^{N-1} d\varepsilon \quad (3.7)$$

Here, ε is the energy that is deposited into internal modes of the reactant ion complex during collision, such that the energy available to the energized molecule is $E^* = E_i + \varepsilon$, and $P_d = 1 - \exp[-k_{tot}(E^*)\tau]$ is the dissociation probability, where $k_{tot}(E^*)$ is the unimolecular rate constant for the dissociation of the energized molecule into all product channels. If the dissociative lifetime of the energized molecule is shorter than the average experimental time-of-flight, the integration in Eq. (3.7) recovers Eq. (3.6). Eq. (3.7) also accounts for the competition between multiple dissociation pathways using the

$k_j(E^*)/k_{tot}(E^*)$ ratio, which uses statistical theory[41,42] to estimate the rate for each reaction channel j. The rate coefficient, $k_j(E^*)$, is defined by RRKM theory as follows:

$$k_{tot}(E^*) = \sum_j k_j(E^*) = \sum_j d_j N_j^{\dagger}(E^* - E_{0,j})/h\rho(E^*) \quad (3.8)$$

where the reaction degeneracy, d_j, is calculated from the ratio of the rotational symmetry numbers of reactants and products for channel j, $N_j^{\dagger}(E^* - E_{0,j})$ is the sum of rovibrational states of the transition state (TS), and $\rho(E^*)$ is the density of states of the energized molecule at E^*. In the present work, the heterolytic and homolytic bond cleavages can be characterized as proceeding over loose TSs equivalent to the product asymptotes.[43] Thus, these TSs are treated at the phase space limit (PSL) in which the transitional modes are rotors.[41] All molecular parameters for the TSs and energized molecules were taken from quantum chemical calculations described below.

The model cross sections of Eq. (3.7) were convoluted over the kinetic energy distributions of the neutral and ion reactants before comparison to experimental data. The fitting parameters in these equations ($\sigma_0, N,$ and $E_{0,j}$) were then optimized using a nonlinear least-squares criterion to reproduce the experimental data throughout the threshold region. The $E_{0,j}$ threshold energies obtained are equivalent to 0 K bond energies for forming the fragment ions from the reactant ions. The uncertainties in these bond energies were determined from the range of parameters obtained from modeling four independent data sets, scaling the vibrational frequencies of reactants and products by ± 10%, varying the best fit N value by ±0.1, changing the experimental time-of-flight up and down by a factor of 2, and including the uncertainty in the energy scale, ± 0.05 eV (lab).

3.3.3 Computational Details

To obtain stable geometries, vibrational frequencies, and energies for $N_2H_5^+$, $N_2D_5^+$, and their fragments, theoretical calculations were performed using the Gaussian 16 Rev. A03[44] suite of programs. Initial optimizations were performed at the B3LYP/6-31G(d) level of theory[45,46] utilizing the opt = loose criterion (maximum step size of 0.01 au and an RMS force of 0.0017 au). Final geometry optimizations and vibrational calculations were performed at the MP2/6-311+G(d,p) level of theory. Vibrational frequencies were scaled by 0.989 for the zero-point energy and thermal (298 K) corrections that use a harmonic oscillator/rigid rotor model.[47] Using optimized geometries, single-point energy calculations were performed at the B3LYP-GD3BJ and restricted open-shell (RO) MP2(full) (where full indicates correlation of all electrons)[48-52] levels with a 6-311+G(2d,2p) basis set. The empirical dispersion function was set to the D3 version of Grimme dispersion[53] (GD3) with Becke–Johnson (BJ) damping for the B3LYP level of theory. In addition, single point ROCCSD(T)[54-58] (where T indicates perturbative triple excitations) calculations were performed using the correlation consistent basis sets, aug-cc-pV*n*Z (*n* = D, T, and Q), to formulate two complete basis set (CBS) extrapolation limits, as detailed by Schwartz[59] and Feller,[60] and outlined in previous work.[61] The restricted open-shell approach was employed to eliminate the effects of spin contamination,[62,63] which is particularly important in determination of bond energies at the MP2(full) and CCSD(T) levels resulting from homolytic bond dissociations, as discussed below. For these systems, the restricted open-shell corrections were relatively small for the MP2(full) and CCSD(T) levels, 0.002–0.01 eV. The results also include the basis set superposition error corrections determined at the full

counterpoise (cp) level.[64,65] As is often the case, counterpoise corrections are relatively small for the B3LYP-GD3BJ and ROCCSD(T) levels, 0.001–0.03 eV, whereas corrections for the ROMP2(full) level were larger in general, 0.15–0.18 eV.

3.4 Results and Discussion

3.4.1 Experimental Cross Sections. CID of $N_2H_5^+$

Experimental cross sections for TCID with Xe were measured for $N_2H_5^+$ and a typical data set is shown in Figure 3.1 after extrapolation to zero pressure. Here, TCID of $N_2H_5^+$ led to N–N bond cleavages at energies > 5 eV, with the charge being retained by either fragment, reactions (3.4) and (3.5). The apparent thresholds for the homolytic and heterolytic N–N bond cleavages are well above the Δ_rH_0 for formation of the ground state asymptotes of reactions (3.4a) and (3.5a), 3.58 ± 0.03 and 4.57 ± 0.03 eV, but seem similar to the Δ_rH_0 for the excited state asymptotes of reactions (3.4b) and (3.5b), 5.01 ± 0.03 and 5.83 ± 0.03 eV, respectively.

Notably, we only observed these two pathways with TCID, whereas Øiestand and Uggerud observed the dominant losses of H_2 and H (yielding $N_2H_3^+$ and $N_2H_4^+$, respectively) along with $NH_3^+ + NH_2$ and $NH_4^+ + NH$ utilizing MIKES.[7] Their result seems reasonable because the loss of H_2 in reaction (3.1) is the lowest energy decomposition pathway available. Therefore, we spent a significant amount of time searching for evidence of these additional pathways, which required operating the quadrupole mass filter in a high-resolution mode that also decreases the overall signal intensity. Even in this high-resolution mode, possible signals for reactions (3.1) and (3.2) forming $N_2H_3^+ + H_2$ and $N_2H_4^+ + H$ still overlap strongly with that of the intense $N_2H_5^+$

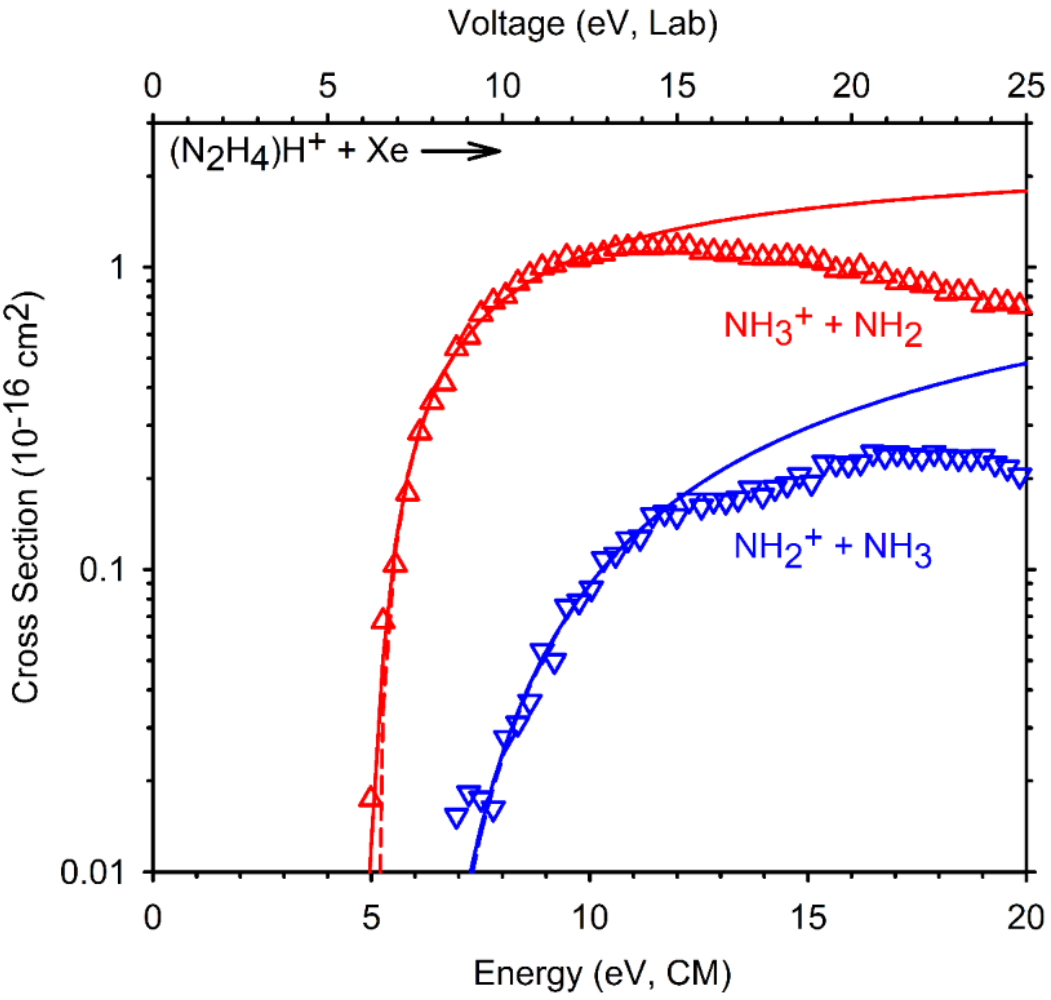

Figure 3.1. Zero pressure TCID cross sections for $N_2H_5^+$ as a function of kinetic energy in the center-of-mass frame (lower x-axis) and laboratory frame (upper x-axis). The solid lines represent the model of Eq. (3.7) convoluted with the internal and kinetic energy distributions of the reactants. Dashed lines represent the model cross sections in the absence of kinetic energy broadening for reaction having an internal energy of 0 K.

reactant ion such that their cross sections needed to be greater than about 1.5 and 8 $Å^2$, respectively, to be observed clearly. (Note that these limits are larger than the maximum cross sections for the channels that were observed, Figure 3.1, indicating that our sensitivity to these channels is quite low.) Within these constraints, we observed no evidence for these channels nor for the formation of NH_4^+, where its cross section needed to be greater than 0.01 $Å^2$ to be observed under our TCID conditions.

In comparing the qualitative observations of the TCID and MIKES experiments, the available energy explains why reaction (3.5) was not observed by Øiestand and Uggerud but is observed here. It is possible that the failure to observe the formation of NH_4^+ is related to the shorter experimental time window of our instrument post collision, which presumes that the formation of NH_4^+ requires a longer-lived intermediate because it requires an additional hydrogen atom transfer from one nitrogen to the other. Another difference in the two experiments is the rotational distribution of the energized $N_2H_5^+$ molecule. In the metastable decompositions, the reactant ions probably have a rotational energy distribution that is near thermal, whereas the collisional excitation utilized in the present experiments certainly creates rotationally excited species. (In actuality, there is a broad but unknown distribution of rotational energies dependent on the impact parameter of the reactants, which prevents quantitative evaluation of this effect.) Because of angular momentum conservation, rotationally excited $N_2H_5^+$ molecules will not efficiently form product channels that have a small reduced mass (μ), like reactions (3.1, ~1.9 amu) and (3.2, ~1.0 amu), because this limits how large their orbital angular momentum ($L \propto \mu$) can be. The NN bond cleavage reactions with $\mu \sim 9.3$ amu are much less affected. This effect diminishes the probability of these channels in the TCID study compared to the

MIKES work, which may explain why they were not readily observed in the current study.

3.4.2 Experimental Cross Sections. CID of $N_2D_5^+$

To better explore whether reactions (3.1) and (3.2) could be observed, experimental cross sections were collected for the perdeuterated analogue of protonated hydrazine ($N_2D_5^+$), as illustrated in Figure 3.2, after extrapolation to zero pressure. Under our experimental conditions, $N_2D_5^+$ also dissociates by homolytic and heterolytic N–N bond cleavage, forming $ND_3^+ + ND_2$ and $ND_2^+ + ND_3$, respectively. Comparisons of the results in Figures 3.1 and 3.2 show that the cross sections for the lower energy homolytic N–N bond cleavage, reaction (3.4), and higher energy heterolytic N–N bond cleavage, reaction (3.5), have similar magnitudes and energy dependences in both the perprotio and perdeutero systems.

The examination of the deuterated analogues allows better mass separation between the fragments, which greatly reduces the mass overlap in the quadrupole mass filter. Again operating in a high resolution mode, we spent a significant amount of time searching for evidence of the D_2 and D losses but these were still not observed, nor was ND_4^+. Because of the better mass separation, the upper limits to these cross sections are now about 0.2, 1.5, and 0.01 $Å^2$, respectively. The former cross section should have been observable, suggesting that the angular momentum argument made above is probably limiting the efficiency of these reactions under TCID conditions. Likewise, ND_4^+ (as well as NH_4^+) should have been observed easily in our experiments.

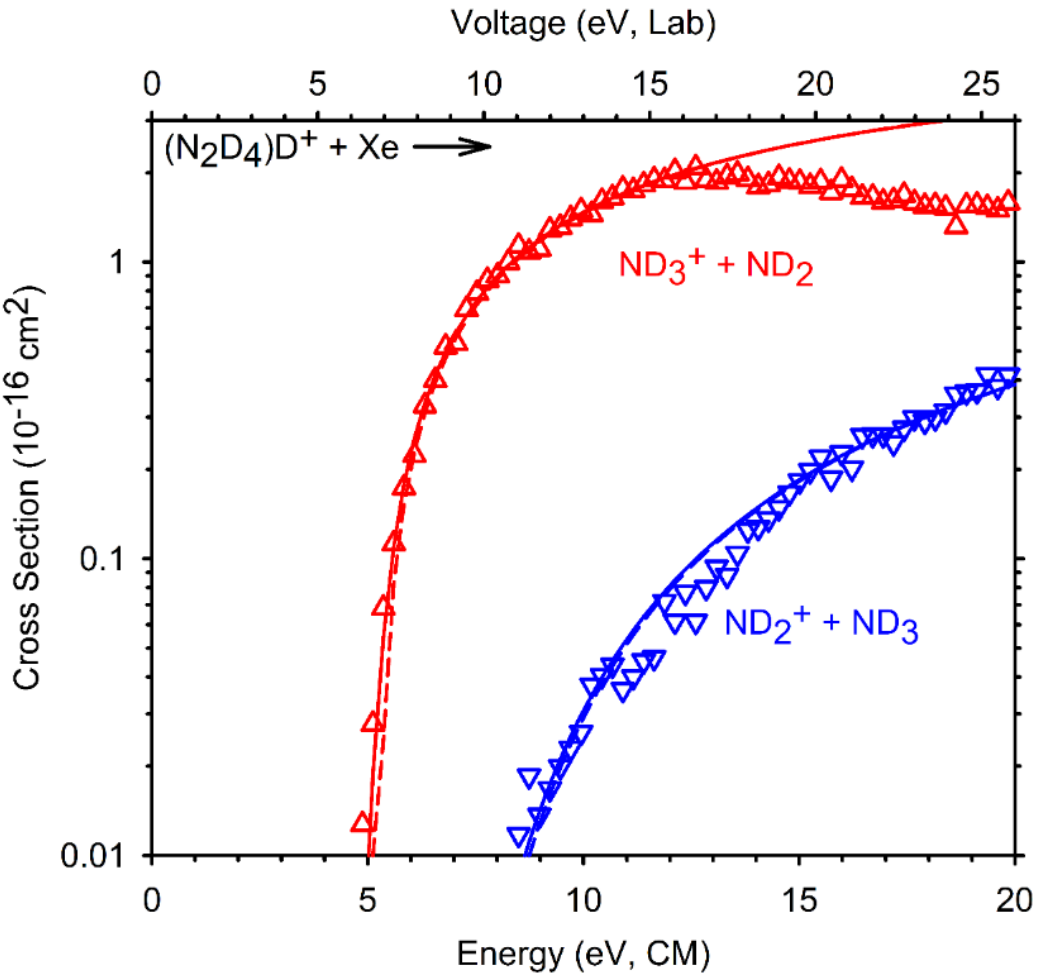

Figure 3.2. Zero pressure TCID cross sections for $N_2D_5^+$ as a function of kinetic energy in the center-of-mass frame (lower x-axis) and laboratory frame (upper x-axis). The solid lines represent the model of Eq. (3.7) convoluted with the internal and kinetic energy distributions of the reactants. Dashed lines represent the model cross sections in the absence of kinetic energy broadening for reaction having an internal energy of 0 K.

3.4.3 Experimental Results. Modeled Cross Sections

Analyses of all fragmentation channels, using Eq. (3.7) yielded models illustrated in Figures 3.1 and 3.2 with optimized parameters (σ_0, N, and E_0) that are given in Table 3.2. The figures show the models reproduce the cross sections of all products with fidelity throughout the threshold regions and up to at least 11 eV in the CM frame for $N_2H_5^+$ and $N_2D_5^+$, alike. Entropies of dissociation at 1000 K, $\Delta S^{\dagger}_{1000}$, are also listed for these analyses and are strongly positive, as expected for loose PSL transition states. If the total cross section is modeled using Eq. (3.6) (without lifetime or competitive effects), the thresholds are 0.09 and 0.08 eV higher in energy than those obtained by including lifetime effects. These small kinetic shifts are reasonable for the small molecular systems explored here.

For both the perprotio and perdeutero systems, the models treated reactions (3.4) and (3.5) as proceeding over loose PSL transition states with measured 0 K thresholds for the perprotio system of 5.22 ± 0.16 and 5.98 ± 0.22 eV, respectively, where the average difference between the two thresholds is 0.77 ± 0.07 eV. For the perdeutero system, the measured 0 K thresholds are 5.15 ± 0.11 and 5.95 ± 0.13 eV, respectively, with the average difference between the two thresholds being 0.80 ± 0.06 eV. In addition, we attempted to include reactions (3.1)–(3.3) (observed by Øiestand and Uggerud) as dark channels into our modeling scheme but were unsuccessful. If reaction (3.1), $N_2H_3^+ + H_2$, or reactions (3.1) and (3.2) were included (using literature thermochemistry for their thresholds), we could not reproduce our experimental cross sections over any energy range. When reaction (3.2), $N_2H_4^+ + H$, alone was included, we could reproduce our experimental cross sections, as shown in Figure 3.S1 of the Supplementary Material.

Table 3.2. Optimized parameters of Eq. (7) from analysis of CID cross sections for $N_2H_5^+$ and $N_2D_5^+$[a]

products	σ_0[b]	N[b]	E_0 (eV)[b]	E_0 (PSL, eV)[c]	$\Delta S^{\dagger}_{1000}$ (J/mol K)
$NH_3^+ + NH_2$	1.8 (0.2)	1.2 (0.1)	5.31 (0.13)	5.22 (0.16)	57 (4)
$NH_2^+ + NH_3$	0.6 (0.1)			5.98 (0.22)	53 (4)
$ND_3^+ + ND_2$	1.1 (0.1)	1.4 (0.1)	5.23 (0.08)	5.15 (0.11)	77 (4)
$ND_2^+ + ND_3$	0.3 (0.1)			5.95 (0.13)	73 (3)

[a] Uncertainties in parentheses. [b] Parameter without RRKM included. [c] Parameters for modeling where lifetime effects are taken into account.

Here, competition with the $N_2H_4^+$ + H low-energy dark channel shifted the 0 K thresholds for reactions (3.4) and (3.5) to 4.55 ± 0.10 and 5.65 ± 0.15 eV, respectively. Despite being able to produce our experimental cross sections in this case, we do not believe that this modeling scheme represents the experimental results well because a) we did not observe either experimental channel (despite a careful search), b) including only one dark channel (and not the major one) would be inconsistent with the previous results, and c) the thresholds measured *without* including the dark channels match known experimental onsets for reactions (3.4b) and (3.5b), as discussed further below. Thus, the 0 K thresholds modeled as proceeding over loose PSL transition states without the dark channels included represent our best experimental thresholds for reactions (3.4) and (3.5).

3.4.4 Theoretical Results: $N_2H_5^+$ and $N_2D_5^+$

As noted above, several levels of theory were applied to calculate the thermodynamic properties of protonated hydrazine and its N–N bond cleavage products, as listed in Table 3.3. For reaction (3.4), the planar NH_3^+ product has a $^2A_2''$ ground state, which is isoelectronic with CH_3, whereas NH_2 has a $^2B_1$ ground state with the $^2A_1$ first excited state lying 1.33–1.38 eV higher in energy. Thus, reactions (3.4a) and (3.4b), $NH_3^+(^2A_2'') + NH_2(^2B_1)$ and $NH_3^+(^2A_2'') + NH_2(^2A_1)$, are predicted to require 3.47–3.64 and 4.80–5.02 eV at 0 K, respectively, in good agreement with the experimental values from Table 3.1, 3.58 ± 0.03 and 5.01 ± 0.03 eV. For reaction (3.5), the NH_3 ground state is $^1A_1$ and that of NH_2^+ is $^3B_1$, with the lowest singlet state being $^1A_1$, and the next excited singlet state having a $^1B_1$ configuration. Thus, reactions (3.5a) and (3.5b) are predicted to be endothermic by 4.36–4.64 and 5.90–6.03 eV at 0 K, respectively, which again agrees

Table 3.3. Comparison of experimental 0 K bond energies (eV) to theoretical values for $(N_2H_4)H^+$ and $(N_2D_4)D^+$[a]

Product ion	Product Neutral	expt[b]	Literature[c]	B3LYP-GD3BJ[d]	ROMP2(full)[d]	ROCCSD(T)[e]	ROCCSD(T)[f]
NH_3^+ ($^2A_2''$)	NH_2 ($^2B_1$)		3.58 ± 0.03	3.47	3.50	3.64	3.63
	NH_2 ($^2A_1$)	5.22 ± 0.16	5.01 ± 0.03	4.80	4.87	5.02	5.01
NH_2^+ ($^3B_1$)	NH_3 ($^1A_1$)		4.57 ± 0.03	4.62	4.36	4.64	4.63
NH_2^+ ($^1A_1$)		5.98 ± 0.22	5.83 ± 0.03	6.03	5.98	5.91	5.90
ND_3^+ ($^2A_2''$)	ND_2 ($^2B_1$)		3.68 ± 0.03[g]	3.57	3.60	3.74	3.73
	ND_2 ($^2A_1$)	5.15 ± 0.11	5.11 ± 0.03[g]	4.89	4.97	5.11	5.10
ND_2^+ ($^3B_1$)	ND_3 ($^1A_1$)		4.67 ± 0.03[g]	4.72	4.46	4.74	4.73
ND_2^+ ($^1A_1$)		5.95 ± 0.13	5.93 ± 0.03[g,h]	6.12	6.08	6.00	5.99
	MAD[i]		1.45	1.43	1.60	1.39	1.40
	MAD[j]		0.11	0.23	0.17	0.09	0.10

[a] Theoretical values with counterpoise corrections. [b] Primary threshold energies from Table 3.2. [c] Values taken from Table 3.1 unless otherwise specified. [d] BDEs calculated at the indicated level using a 6-311+G(2d,2p) basis set and MP2/6-311+G(d,p) optimized geometries. [e] BDEs calculated at the ROCCSD(T)/Swartz-CBS//MP2/6-311+G(d,p) level of theory. [f] BDEs calculated at the ROCCSD(T)/Feller-CBS//MP2/6-311+G(d,p) level of theory. [g] ZPE corrected for isotope effects. [h] Ionization energy from Ref. [16] [i] Mean absolute deviation between experiment and the adiabatic asymptotes. [j] Mean absolute deviation between experiment and the non-adiabatic asymptotes.

with the experimental values of 4.57 ± 0.03 and 5.83 ± 0.03 eV, respectively. For the perdeutero system, reactions (3.4a), (3.4b), (3.5a), and (3.5b) are predicted to require 3.57–3.74, 4.89–5.11, 4.46–4.74, and 5.99–6.12 eV at 0 K once corrected for the zero-point differences between the isotopes.

3.4.5 Comparison of Experimental and Theoretical Bond Enthalpies

Table 3.3 lists the experimental and theoretical 0 K BDEs with counterpoise corrections. Here, the theoretical values with counterpoise agree very well with our experimental BDEs and literature Δ_rH_0 values for the homolytic and heterolytic N–N bond cleavages leading to the excited state asymptotes, reactions (3.4b) and (3.5b), but are well above those for the ground state asymptotes of reactions (3.4a) and (3.5a), respectively. In addition, the differences between our measured BDEs for the perprotio and perdeutero analogues, 0.77 ± 0.07 and 0.80 ± 0.06 eV, align well with the differences in the existing endothermicities for reactions (3.4b) and (3.5b), 0.82 ± 0.01 and 0.82 ± 0.01 eV, respectively. Notably, only the ROCCSD(T) calculations reproduce this difference, Table 3.3. With these comparisons, we can safely conclude that the 0 K threshold energies for the homolytic and heterolytic N–N bond cleavages of $N_2H_5^+$ and $N_2D_5^+$ can be equated to the 0 K BDEs for dissociation to their non-adiabatic asymptotes. The non-adiabatic behavior for reaction (3.5) can be simply explained by the spin-forbidden transition from the ground state of $N_2H_5^+(^1A')$ to the ground state asymptote of NH_2^+ ($^3B_1$) + NH_3 ($^1A_1$), whereas the non-adiabatic behavior for reaction (3.4) is more complicated and discussed below.

3.4.6 Understanding the Observed Non-adiabatic Behavior

Armentrout and Simons[43] have previously considered the qualitative aspects of homolytic and heterolytic dissociations of polyatomic heteronuclear species, such as the ones presented here. An adiabatic heterolytic bond cleavage of a covalent or noncovalent bond occurs when one fragment retains both bonding electrons while leaving both fragments in their ground electronic states. In an adiabatic homolytic bond cleavage, both ground state fragments retain a single "bonding electron". For protonated hydrazine, adiabatic cleavage of the N–N bond should proceed along reaction (3.4a), yielding NH_3^+ ($^2A_2''$) + NH_2 ($^2B_1$). This dissociation is spin-allowed and appears to correspond directly to simple heterolytic bond cleavage. The failure to observe this process experimentally must therefore be associated with some other constraint.

In an attempt to further understand why the homolytic and heterolytic N–N bond cleavages of $N_2H_5^+$ behave non-adiabatically, we included the lone-pair electrons on the unprotonated nitrogen in the correlation diagram for dissociation of a heteronuclear species, as previously outlined by Armentrout and Simons,[43] where only the sigma electrons were considered. In this view, the $^1A'$ ground state of $N_2H_5^+$ has a $\sigma^2\pi^2$ configuration, where the σ molecular orbital (MO) is the N–N bond and the π MO is the lone pair orbital on the unprotonated nitrogen. These orbitals are illustrated in Figure 3.3. As per Armentrout and Simons, such a species has several electronic surfaces corresponding to configurations having $\sigma^2\pi^2$ (singlet spin), $\sigma^1\sigma^{*1}\pi^2$ (singlet and triplet spin), and $\sigma^{*2}\pi^2$ (singlet spin) character. Because of the addition of the π orbitals, protonated hydrazine also has electronic surfaces having $\sigma^2\sigma^{*1}\pi^1$ (singlet and triplet spin), $\sigma^2\sigma^{*2}$ (singlet spin), and $\sigma^1\sigma^{*2}\pi^1$ (singlet and triplet spin) character. To explore

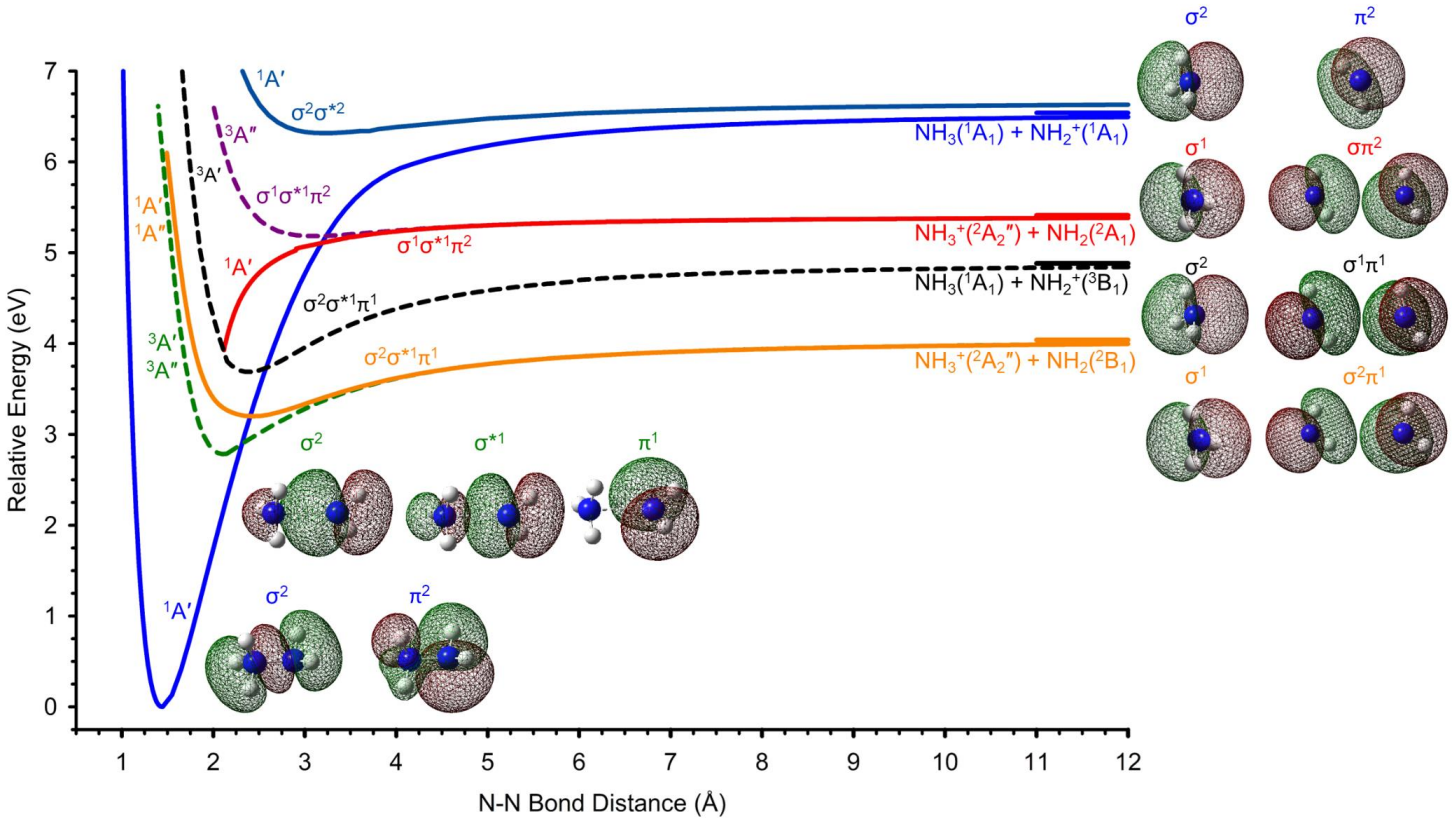

Figure 3.3. $^1A'(\sigma^2\pi^2)$ (solid blue line), $^3A'$ and $^3A''(\sigma^2\sigma^{*1}\pi^1)$ (short-dashed green line), $^1A'$ and $^1A''(\sigma^2\sigma^{*1}\pi^1)$ (solid orange line), $^3A'(\sigma^2\sigma^{*1}\pi^1)$ (short-dashed black line), $^1A'(\sigma^1\sigma^{*1}\pi^2)$ (solid red line), $^3A''(\sigma^1\sigma^{*1}\pi^2)$ (short-dashed purple line), and $^1A'(\sigma^2\sigma^{*2})$ (solid teal line) reaction coordinate surfaces for $N_2H_5^+$ as a function of N–N bond distance calculated at the MP2/6-311+G(d,p) level of theory. The asymptotic limits are indicated as solid bars at N–N bond distances > 11 Å.

these surfaces of $N_2H_5^+$, several relaxed PES scans as a function of N–N bond distance were performed, as calculated at the MP2/6-311+(d,p) level of theory utilizing the opt = loose and SCF = DM criterion to minimize surface jumping. These surfaces are shown in Figure 3.3 along with the MOs for reactants and products

Interestingly, these calculations find that ground state $N_2H_5^+$ ($\sigma^2\pi^2$) dissociates smoothly by heterolytic dissociation to the excited state asymptote of reaction (3.5b), $NH_2^+(^1A_1,\pi^2) + NH_3(^1A_1,\sigma^2)$. Here, the lone-pair electrons on the NH_2^+ species are located in the out-of-plane b_1 MO, with the a_1 orbital being empty, such that when the two nitrogens approach one another, the lone-pair electrons on ammonia donate into the empty a_1 MO on NH_2^+. Thus, the $\sigma^2\pi^2$ character of ground state $N_2H_5^+$ is preserved. Notably, if the occupied b_1 MO on NH_2^+ approaches the NH_3, another $^1A'$ surface having $\sigma^2\sigma^{*2}$ character is formed, Figure 3.3.

If one starts with the ground state product asymptote, $NH_3^+(^2A_2'') + NH_2(^2B_1)$, the ionized ammonia product clearly has a single σ electron, whereas the NH_2 product has three electrons, one in the b_1 MO and two in the a_1 MO. Figure 3.3 shows that when these species approach one another, the calculations find both singlet and triplet surfaces (as expected) but the negative end of the dipole moment of the NH_2 group points towards the nitrogen of the NH_3 fragment, leading to a ($\sigma^2\sigma^{*1}\pi^1$) electron configuration. Both $^{1,3}A'$ and $^{1,3}A''$ surfaces were located, are degenerate because of the three-fold symmetry of the NH_3 group, and have minima that lie 2.45–2.97 and 2.20–2.62 eV above the $N_2H_5^+(^1A')$ ground state. Because the antibonding σ^* MO is occupied, these surfaces are only weakly bonding (largely ion-induced dipole potential). Similar surfaces are generated when the $NH_2^+(^3B_1, \sigma^1\pi^1) + NH_3(^1A_1, \sigma^2)$ species approach one another. Because both the a_1 and b_1

MOs on NH_2^+ are singly occupied, $N_2H_5^+$ ($\sigma^2\sigma^{*1}\pi^1$) is formed regardless of the molecular alignment.

Starting with the $NH_3^+(^2A_2'', \sigma^1)$ + $NH_2(^2A_1, \sigma^1\pi^2)$ asymptote, the NH_2 now has the b_1 MO doubly occupied and the a_1 MO singly occupied. As the two nitrogens approach, they form singlet and triplet spin state surfaces because the valence electrons evolve into a $\sigma^1\sigma^{*1}\pi^2$ configuration of $N_2H_5^+$. The excited $^1A'$ surface located is attractive but at short N-N separations, the calculation collapsed to the ground state $^1A'$ surface. Note that these $\sigma^2\pi^2$ and $\sigma^1\sigma^{*1}\pi^2$ surfaces are two components of the qualitative surfaces identified by Armentrout and Simons.[43] The remaining $\sigma^{*2}\pi^2$ surface dissociates to NH_3^{2+} + NH_2^- (heterolytic cleavage such that NH_2 retains both σ electrons), which is much higher in energy than the asymptotes shown. At the MP2/6-311+G(d,p) level, this asymptote lies over 20 eV above ground state $N_2H_5^+$.

Clearly, these calculations correspond to single configurations and the "real" adiabatic surfaces will allow mixing associated with multiconfiguration effects. However, the surfaces shown in Figure 3.3 are probably representative of the diabatic surfaces, which permit a qualitative explanation for the observed experimental behavior. Namely, $N_2H_5^+(^1A', \sigma^2\pi^2)$ does not dissociate to either $NH_3^+(^2A_2'', \sigma^1)$ + $NH_2(^2B_1, \sigma^2\pi^1)$ in reaction (3.4a) nor $NH_2^+(^3B_1, \sigma^1\pi^1)$ + $NH_3(^1A_1, \sigma^2)$ in reaction (3.5a) because this requires shifting one of the two π electrons into a σ MO. The observed dissociations to $NH_3^+(^2A_2'', \sigma^1)$ + $NH_2(^2A_1, \sigma^1\pi^2)$, reaction (3.4b), and $NH_2^+(^1A_1, \pi^2)$ + $NH_3(^1A_1, \sigma^2)$, reaction (3.5b), both conserve the $\sigma^2\pi^2$ orbital occupations, indicating they are both diabatic dissociations. As the cleavage of the N–N bond is a high-energy process, the lifetime of the energized $N_2H_5^+$ molecule must be short, such that non-adiabatic (non-Born-Oppenheimer)

behavior is preferentially observed.

3.4.7 Comparison to Existing PESs

As noted above, Øiestand and Uggerud calculated several reaction pathways for the observed fragmentations of $N_2H_5^+$ utilizing MIKES.[7] Here, we explored similar PESs for variations in the ∠H-N–N–H angle of $N_2H_5^+(^1A')$, with results listed in Table 3.4 and shown in Figure 3.4. Øiestand and Uggerud found TS1/15 between the $N_2H_5^+$ ground state and the proton-bound NH_2 dimer (INT15) by using complete active space multiconfiguration SCF (CASSCF) calculations. In their results, the proton is located unsymmetrically between the two nitrogen atoms (presumably in a double well potential), whereas our MP2 level calculations find similar TS1/15 and INT15 structures with the proton positioned symmetrically between the two NH_2 groups, Figure 3.4. Explicit calculations of the proton motion in this case indicate that the two-well potential has merged into a single potential well. Notably, their calculations and our MP2(full) and ROCCSD(T) calculations predict that TS1/15 is lower in energy than the $NH_3^+(^2A_2'') + NH_2(^2B_1)$ ground state asymptote (although our B3LYP calculations predict INT15 lies 0.89 eV higher in energy than TS1/15 in part because this level of theory leads to a different geometry, the asymmetric two-well potential). In addition to this reaction pathway, we also relocated TS1/1, which corresponds to proton transfer between the nitrogen centers, Figure 3.4,[7] where our calculations predict similar energetics to that of Øiestand and Uggerud. We also located TS1/3, which corresponds to rotation about the N–N bond and is predicted to lie only 0.06–0.07 eV higher in energy than the ground state of $N_2H_5^+$ at 0 K.

Table 3.4. Relative energies at 0 K (free energies at 298 K) in eV for species along the potential energy surfaces of protonated hydrazine transformations[a]

Structure	B3LYP-GD3BJ	ROMP2(full)	ROCCSD(T)[b]	Literature[c]
$N_2H_5^+$ ($^1A'$)	0.0 (0.0)	0.0 (0.0)	0.0 (0.0)	0.0
TS1/15	3.85 (3.83)	3.74 (3.71)	2.85 (2.82)	1.94
INT15	4.74 (4.70)	3.38 (3.34)	2.70 (2.66)	1.61
TS1/1	1.90 (1.90)	1.96 (1.95)	1.95 (1.94)	2.10
TS1/3	0.06 (0.07)	0.07 (0.08)	0.06 (0.07)	

[a] Free energies in parenthesis. All values calculated at the level of theory indicated using the 6-311+G(2d,2p) basis set with optimized structures, zero-point energies, and thermal corrections calculated at MP2/6-311+G(d,p) level of theory.
[b] ROCCSD(T)/Feller CBS//MP2/6-311+G(d,p). [c] Values from Ref. 7.

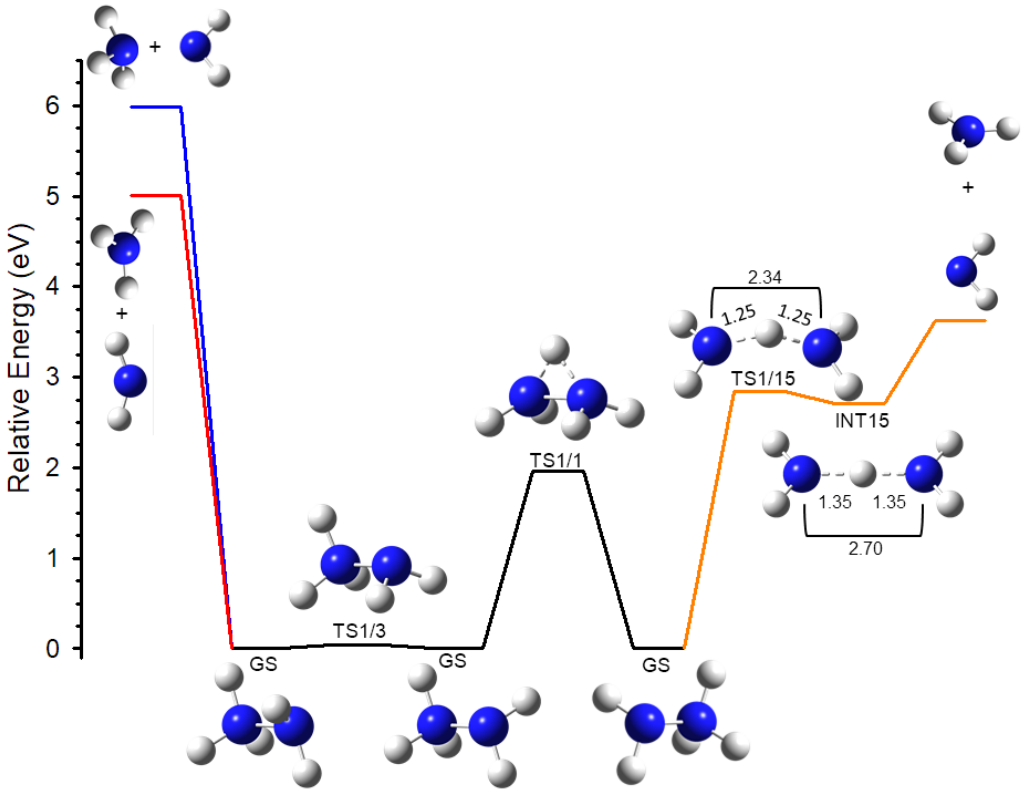

Figure 3.4. Reaction coordinate surface for rearrangement of $N_2H_5^+$ and its adiabatic homolytic (orange curve), diabatic homolytic (red curve), and non-adiabatic heterolytic (blue curve) cleavage reactions. N–N and N–H (in Å) bond distances are included for TS1/15 and INT15.

As noted above, Øiestand and Uggerud observed that the homolytic N–N cleavage was a minor product channel in their MIKES experiments for $N_2H_5^+$ ions formed by chemi-ionization of hydrazine by H_3^+. Given the observations here, it seems plausible that this channel is a minor product in their system because it is also limited by the diabatic behavior, which cannot begin until 5.01 ± 0.03 eV, reaction (3.4b). This hypothesis suggests that excited H_3^+ could form the excited $N_2H_5^+$ species needed to access this product asymptote.

3.5 Conclusion

Energy-resolved threshold collision-induced dissociation with Xe was performed on protonated hydrazine and its perdeuterated variant. The primary dissociation pathway of $N_2H_5^+$ led to homolytic and heterolytic N–N bond cleavages, $NH_3^+ + NH_2$ and $NH_2^+ + NH_3$, with analogous results for the perdeuterated system. Statistical analysis of the TCID data was used to obtain 0 K bond energies for the dissociation pathways. The experimental results are then compared against theoretical calculations performed here, at the B3LYP-GD3BJ and ROMP2(full) levels with a 6-311+(2d,2p) basis set and at the ROCCSD(T) level using two methods for the CBS extrapolation. The comparison between this work, existing experimental, and theoretical 0 K BDEs shows the homolytic and heterolytic N–N bond cleavages of $N_2H_5^+$ and $N_2D_5^+$ behave non-adiabatically and are limited by the asymptotic energies of $NH_3^+(^2A_2'') + NH_2(^2A_1)$ and $NH_2^+(^1A_1) + NH_3(^1A_1)$, respectively. The latter case can be attributed to simple spin conservation, whereas an analysis of the occupied valence molecular orbitals indicates that both

reactions behave diabatically in terms of conserving the σ and π character of the lone pair electrons on the nitrogen atoms.

3.6 Supporting Information

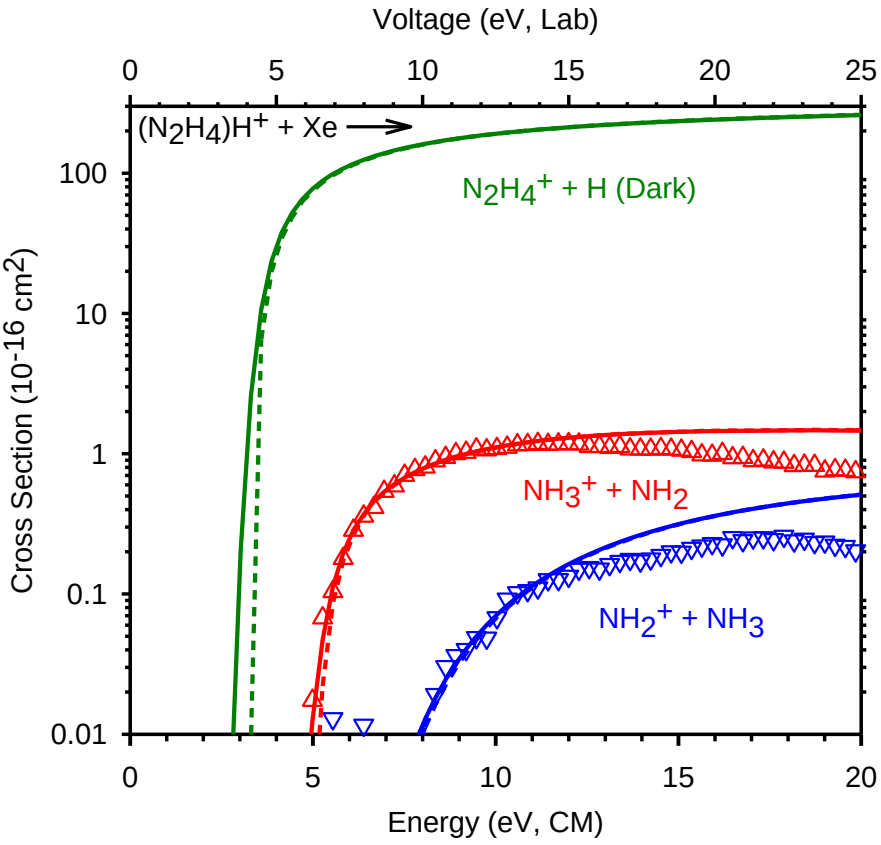

Figure 3.S1. Zero pressure TCID cross sections for $N_2H_5^+$ as a function of kinetic energy in the center-of-mass frame (lower x-axis) and laboratory frame (upper x-axis). The solid lines represent the model of Eq. (3.7) convoluted with the internal and kinetic energy distributions of the reactants. Dashed lines represent the model cross sections in the absence of kinetic energy broadening for reaction having an internal energy of 0 K. The solid and dashed green lines indicate the dark channel, $N_2H_4^+$ + H. The experimental cross sections were modeled using a loose PSL TS model, see text.

3.7 References

[1]J. A. Gardner, R. A. Dressler, R. H. Salter *et al.*, J. Phys. Chem. **96**, 4210 (1992).

[2]G. Lunn, E. B. Sansone, and L. K. Keefer, Environ. Sci. Technol. **17**, 240 (1983).

[3]G. V. Buxton, and C. R. Stuart, J. Chem. Soc., Faraday Trans. **92**, 1519 (1996).

[4]M. Zhang, R. Cheng, Z. Chen *et al.*, Int. J. Hydrogen Energy **30**, 1081 (2005).

[5]S. G. Pakdehi, M. Salimi, and M. Rasoolzadeh, Res. Appl. Mech. Eng. **3**, 21 (2014).

[6]J.-P. Schirmann, and P. Bourdauducq, in *Ullmann's Encyclopedia of Industrial Chemistry* (Wiley-VCH Verlag GmbH & Co. KGaA, 2000).

[7]E. L. Øiestad, and E. Uggerud, Int. J. Mass Spectrom. Ion Processes **165-166**, 39 (1997).

[8]R. Branko, E. P. Reinhardt, L. Gregor von *et al.*, Journal of Physics: Conference Series **16**, 561 (2005).

[9]B. Ruscic, D. Feller, and K. A. Peterson, Theor. Chem. Acc. **133**, 1415 (2013).

[10]B. Ruscic, and D. H. Bross, (ATcT.anl.gov, 2016).

[11]D. Feller, D. H. Bross, and B. Ruscic, J. Phys. Chem. A **121**, 6187 (2017).

[12]S. J. Dunlavey, J. M. Dyke, N. Jonathan *et al.*, Mol. Phys. **39**, 1121 (1980).

[13]S. T. Gibson, J. P. Greene, and J. Berkowitz, J. Chem. Phys. **83**, 4319 (1985).

[14]E. P. L. Hunter, and S. G. Lias, J. Phys. Chem. Ref. Data **27**, 413 (1998).

[15]J. Biesner, L. Schnieder, G. Ahlers *et al.*, J. Chem. Phys. **91**, 2901 (1989).

[16]S. Willitsch, J. M. Dyke, and F. Merkt, Mol. Phys. **102**, 1543 (2004).

[17]C. P. McNary, and P. B. Armentrout, J. Chem. Phys. **145**, 214311 (2016).

[18]C. P. McNary, and P. B. Armentrout, J. Phys. Chem. A **120**, 9690 (2016).

[19]S. A. Shaffer, D. C. Prior, G. A. Anderson *et al.*, Anal. Chem. **70**, 4111 (1998).

[20]S. A. Shaffer, A. Tolmachev, D. C. Prior *et al.*, Anal. Chem. **71**, 2957 (1999).

[21]T. Kim, A. V. Tolmachev, R. Harkewicz *et al.*, Anal. Chem. **72**, 2247 (2000).

[22]R. M. Moision, and P. B. Armentrout, J. Am. Soc. Mass Spectrom. **18**, 1124 (2007).

[23]D. R. Carl, R. M. Moision, and P. B. Armentrout, Int. J. Mass Spectrom. **265**, 308

(2007).

[24]A. L. Heaton, S. J. Ye, and P. B. Armentrout, J. Phys. Chem. A **112**, 3328 (2008).

[25]A. L. Heaton, R. M. Moision, and P. B. Armentrout, J. Phys. Chem. A **112**, 3319 (2008).

[26]D. R. Carl, R. M. Moision, and P. B. Armentrout, J. Am. Soc. Mass Spectrom. **20**, 2312 (2009).

[27]T. E. Cooper, and P. B. Armentrout, Chem. Phys. Lett. **486**, 1 (2010).

[28]D. R. Carl, B. K. Chatterjee, and P. B. Armentrout, J. Chem. Phys. **132**, 044303 (2010).

[29]J. E. Carpenter, C. P. McNary, A. Furin *et al.*, J. Am. Soc. Mass Spectrom. **28**, 1876 (2017).

[30]K. M. Ervin, and P. B. Armentrout, J. Chem. Phys. **83**, 166 (1985).

[31]E. Teloy, and D. Gerlich, Chem. Phys. **4**, 417 (1974).

[32]N. R. Daly, Rev. Sci. Instrum. **31**, 264 (1960).

[33]F. Muntean, and P. B. Armentrout, J. Chem. Phys. **115**, 1213 (2001).

[34]D. A. Hales, L. Lian, and P. B. Armentrout, Int. J. Mass Spectrom. Ion Processes **102**, 269 (1990).

[35]S. E. Stein, and B. S. Rabinovitch, J. Chem. Phys. **58**, 2438 (1973).

[36]T. Beyer, and D. F. Swinehart, Comm. ACM **16**, 379 (1973).

[37]S. E. Stein, and B. S. Rabinovitch, Chem. Phys. Lett. **49**, 183 (1977).

[38]R. G. Gilbert, and S. C. Smith, *Theory of Unimolecular and Recombination Reactions* (Blackwell Scientific, London, 1990).

[39]D. G. Truhlar, B. C. Garrett, and S. J. Klippenstein, J. Phys. Chem. **100**, 12771 (1996).

[40]K. A. Holbrook, M. J. Pilling, and S. H. Robertson, *Unimolecular Reactions* (Wiley, New York, 1996), 2nd edn.

[41]M. T. Rodgers, K. M. Ervin, and P. B. Armentrout, J. Chem. Phys. **106**, 4499 (1997).

[42]M. T. Rodgers, and P. B. Armentrout, J. Chem. Phys. **109**, 1787 (1998).

[43]P. B. Armentrout, and J. Simons, J. Am. Chem. Soc. **114**, 8627 (1992).

[44]M. J. Frisch, G. W. Trucks, H. B. Schlegel *et al.*, (Gaussian, Inc., Wallingford, CT,

USA, 2016).

[45]R. Ditchfield, W. J. Hehre, and J. A. Pople, J. Chem. Phys. **54**, 724 (1971).

[46]A. D. Becke, J. Chem. Phys. **98**, 5648 (1993).

[47]M. K. Kesharwani, B. Brauer, and J. M. L. Martin, J. Phys. Chem. A **119**, 1701 (2015).

[48]C. Møller, and M. S. Plesset, Physical Review **46**, 618 (1934).

[49]M. J. Frisch, M. Head-Gordon, and J. A. Pople, Chem. Phys. Lett. **166**, 275 (1990).

[50]M. J. Frisch, M. Head-Gordon, and J. A. Pople, Chem. Phys. Lett. **166**, 281 (1990).

[51]M. Head-Gordon, and T. Head-Gordon, Chem. Phys. Lett. **220**, 122 (1994).

[52]M. Head-Gordon, J. A. Pople, and M. J. Frisch, Chem. Phys. Lett. **153**, 503 (1988).

[53]S. Grimme, S. Ehrlich, and L. Goerigk, J. Comput. Chem. **32**, 1456 (2011).

[54]J. Cizek, *Advances in Chemical Physics* (Wiley Interscience, New York, 1969), Vol. 14.

[55]G. D. Purvis III, and R. J. Bartlett, J. Chem. Phys. **76**, 1910 (1982).

[56]J. A. Pople, M. Head-Gordon, and K. Raghavachari, J. Chem. Phys. **87**, 5968 (1987).

[57]G. E. Scuseria, C. L. Janssen, and H. F. Schaefer III, J. Chem. Phys. **89**, 7382 (1988).

[58]G. E. Scuseria, and H. F. Schaefer III, J. Chem. Phys. **90**, 3700 (1989).

[59]C. Schwartz, *Methods in Computational Physics* (Academic Press, New York, 1963), Vol. 2.

[60]D. Feller, D. A. Dixon, and J. B. Nicholas, J. Phys. Chem. A **104**, 11414 (2000).

[61]M. T. Rodgers, and P. B. Armentrout, Int. J. Mass Spectrom. **267**, 167 (2007).

[62]C. J. Parkinson, P. M. Mayer, and L. Radom, J. Chem. Soc., Perkin Trans. **2**, 2305 (1999).

[63]A. S. Menon, and L. Radom, J. Phys. Chem. A **112**, 13225 (2008).

[64]S. F. Boys, and R. Bernardi, Mol. Phys. **19**, 553 (1970).

[65]F. B. van Duijneveldt, J. G. C. M. van Duijneveldt-van de Rijdt, and J. H. van Lenthe, Chem. Rev. **94**, 1873 (1994).

CHAPTER 4

THRESHOLD COLLISION-INDUCED DISSOCIATION OF PROTON-BOUND HYDRAZINE AND DIMETHYLHYDRAZINE CLUSTERS

4.1 Abstract

Threshold collision-induced dissociation (TCID) using a guided ion beam tandem mass spectrometer is performed on $(N_2H_4)_nH^+$ where n = 2–4 and on the proton-bound unsymmetrical 1,1-dimethylhydrazine (UDMH) dimer complex. The primary dissociation pathway for all reactants consists of loss of a single hydrazine molecule (or UDMH) followed by the sequential loss of additional hydrazine molecules at higher collision energies for n = 3 and 4. The data were analyzed using a statistical model after accounting for internal and kinetic energy distributions, multiple collisions, and kinetic shifts to obtain 0 K bond dissociation energies (BDEs). These are also converted to values at room temperature by using a rigid rotor/harmonic oscillator approximation and theoretical molecular constants. Experimental BDEs are compared to theoretical BDEs determined at the B3LYP, M06, mPW1PW91, PBE0, MP2(full), and CCSD(T) levels of theory with and without empirical dispersion with a 6-311+G(2d,2p) basis set. The structures of all clusters are explored and exhibit extensive hydrogen bonding.

Reprinted from C. P. McNary, and P. B. Armentrout, J. Phys. Chem. A 120, 9690 (2016).

4.2 Introduction

Hydrazine and unsymmetrical 1,1-dimethylhydrazine (commonly known as UDMH) are used as fuels for some types of mono- and bipropellant rocket engines[1] and have been suggested as possible chemical hydrogen storage systems.[2] These rocket fuels can be released into the atmosphere during successful and unsuccessful rocket burns, such that they can have deleterious effects on the environment.[3] For instance, they can exothermically react with atmospheric gases such as ozone and hydroxyl radicals, creating potentially toxic compounds such as methyl hydroperoxide, methyldiazene, and diazomethane.[4] In addition, it is known that protonated hydrazine, $(N_2H_4)H^+$, is formed in ion/molecule reactions that can occur in the ionosphere or during launch and reentry[1] and upon ionization of neutral clusters of hydrazine in water.[5] It is therefore of interest to explore fundamental properties of the ionic clusters of hydrazine and UDMH in order to understand what impact these systems might have on the environment.

Hydrazine has six hydrogen-bonding sites, four NH donors and two nitrogen lone pair acceptors, and its neutral clusters tend to form cyclic configurations,[6-10] whereas the proton-bound hydrazine clusters have been suggested to form open chain motifs.[11] The structures, energetics, and dynamics of the proton-bound UDMH dimer are unexplored, to the best of our knowledge.

Beu and co-workers[6, 7] developed an intermolecular potential model to determine theoretical structures for $(N_2H_4)_n$ where n = 2–6. With this model, they determined binding energies and the shift, relative to the monomer, in the antisymmetric NH_2 wagging modes for three dimer and four trimer structures of neutral hydrazine. Building on this work, Dyczmons found an additional three dimer[12] and 24 trimer[9] conformations,

including a single saddle point transition state (TS) between two conformations of the dimer.

Lifshitz and co-workers[11] used mass-analyzed ion kinetic energy spectrometry (MIKES) and collision-induced dissociation (CID) to examine the metastable fragmentations of $(N_2H_4)_nH^+$ where n = 2–7. Using MIKES, they found the $(N_2H_4)_nH^+$ clusters would lose a single hydrazine molecule, whereas CID induces sequential loss of hydrazine molecules with increasing translational energy. The kinetic energy release distributions (KERDs) obtained by the MIKES analysis found a Maxwell–Boltzmann-like distribution of the average kinetic energy release for the $(N_2H_4)_nH^+$ systems. From the KERDs, Lifshitz and co-workers extracted bond dissociation energies (BDEs) for these systems. Not surprisingly, clusters of increasing size have decreasing BDEs.[11, 13-15] Lifshitz and co-workers also performed semi-empirical and low level *ab initio* calculations on the proton-bound hydrazine clusters to compare to their BDEs. These calculations suggested an open chain binding motif for $(N_2H_4)_nH^+$ systems where $n > 2$.

In the current study, we use threshold collision-induced dissociation (TCID) in a guided ion beam tandem mass spectrometer (GIBMS) to quantitatively investigate the thermochemistry of the $(N_2H_4)_nH^+$ systems for n = 2–4 and the proton-bound UDMH dimer complex. Analysis of kinetic energy dependent TCID cross sections yields 0 K BDEs for these complexes. These BDEs are then compared to theoretical values from 17 levels of theory, which are also used to thoroughly explore the possible structures of these clusters.

4.3 Experimental and Theoretical Methods

4.3.1 Instrumentation

The proton-bound hydrazine clusters and proton-bound UDMH dimer are created from a 0.1 M solution of hydrazine or UDMH in HPLC grade water using electrospray ionization (ESI) techniques. The solution is advanced at a rate of 100–300 μL/h through a 35 gauge 304 stainless steel needle that has an applied voltage of ~2.5 kV. Once in the gas phase, ions enter the vacuum system through a stainless steel inlet cap with an inlet diameter of 0.010 in. followed directly by a 6.125 in. long by 0.040 in. diameter electro-formed nickel capillary that is heated to a temperature of 120 ºC in order to desolvate large droplets. An 88-plate radio frequency (rf) ion funnel (IF) with superimposed DC gradient field, copied from a design described in detail elsewhere,[16] collects and focuses the ions to increase signal intensity.[17, 18] The voltage bias between the first and last plate of the ion funnel is kept below 20 V to minimize heating of the ions. At the end of the funnel, the ions enter an rf-only hexapole with rf amplitudes typically set at 250 V peak to peak centered around ground. Here, they undergo cooling by $>10^5$ thermalizing collisions with ambient gas (largely air and water).[19] This ensures that ions beyond the hexapole are well-defined by a Maxwell–Boltzmann distribution of rovibrational states at room temperature, as verified by previous work.[19-25]

Ions generated in the ESI/IF/hexapole source[19] then enter the guided ion beam tandem mass spectrometer[26] where they are focused into a magnetic momentum analyzer for initial mass selection. These reactant ions are decelerated to a well-defined kinetic energy and injected into an rf octopole ion guide[27] where they pass through a collision cell containing Ar at low pressures. Although xenon is commonly used in our laboratory,

for reasons described elsewhere,[28, 29] argon is used in the present experiment because preliminary results with xenon showed a significant amount of back scattered reactant ions at low collision energy. As will be seen below, for these weakly bound systems, the use of Ar still permits good collisional energy transfer such that accurate threshold energies can be obtained. Product and remaining reactant ions are extracted from of the octopole, mass selected using a quadrupole mass filter, and detected using a Daly detector.[30]

4.3.2 Data Analysis

Acquiring accurate thermodynamic information from TCID data requires diligent consideration of many experimental factors that convolute the raw data. These factors include the internal and kinetic energy distributions of the ionic and neutral reactants, lifetime effects that arise from a finite experimental time window, the probability of multiple collisions, and competition from other chemical processes.

The measured intensities of the reactant and product ions are first corrected for dissociation outside the collision cell as well as background noise by measuring their intensities with and without gas in the collision cell. They are then converted to absolute cross sections using a Beer–Lambert analogue, as described elsewhere.[26] The energy of the reactants is converted from the lab frame voltage of the ion, V_{lab}, to the center-of-mass energy, E_{CM}, using $E_{\mathrm{CM}} = V_{\mathrm{lab}} m/(m + M)$ where m is the mass of the reactant neutral and M is the mass of the reactant ion. The kinetic energy distribution of the ions is determined using a retarding potential analysis,[26] which also allows the absolute zero of the energy to be obtained. Experiments are performed at three different pressures of the

Ar gas, typically ~0.1, 0.2, and 0.4 mTorr. The cross sections at each pressure are used to linearly extrapolate to a zero pressure cross section, which rigorously represents a single collision event.[31]

The kinetic energy dependent CID cross sections are modeled using the empirical model shown in eq 4.1

$$\sigma(E) = \sigma_0 \sum_i g_i (E + E_i - E_0)^N / E \quad (4.1)$$

where σ_0 is an energy independent scaling factor, E is the relative collision energy, E_0 is the reaction threshold at 0 K, N describes the energy deposition function,[32] and the summation is over the rovibrational states of the reactant ion having energies E_i and populations g_i, where $\Sigma g_i = 1$. Rovibrational states taken from quantum chemical calculations of the ground state structures are directly counted using the Beyer–Swinehart–Stein–Rabinovitch algorithm[33-35] and are assigned populations on the basis of a Maxwell–Boltzmann distribution at 300 K. As the size of the reactants increases, the number of accessible rovibrational states increases such that dissociation lifetimes near the threshold energy can be longer than the experimental time-of-flight, $\tau \sim 5 \times 10^{-4}$ s.[32] For this reason, the apparent dissociation thresholds for larger reaction complexes shift to higher energies. This kinetic shift is accounted for using Rice–Ramsperger–Kassel–Marcus (RRKM) statistical theory[36-38] for unimolecular dissociation and is incorporated into the cross section model, as seen in eq 4.2:

$$\sigma(E) = \left(\frac{N\sigma_0}{E}\right) \sum_i g_i \int_{E_0 - E_i}^{E} (E - \varepsilon)^{N-1} P_{D1} \, d\varepsilon \quad (4.2)$$

Here, ε is the energy that is deposited into internal modes of the reactant ion complex during collision, such that the energy available to the energized molecule is $E^* = E_i + \varepsilon$, and $P_{D1} = 1 - \exp(-k(E^*)\tau)$ is the dissociation probability. If the dissociative lifetime of

the energized molecule is shorter than the average experimental time frame, the integration in eq 4.2 recovers eq 4.1. The rate coefficient, $k(E^*)$, is defined by RRKM theory as in eq 4.3

$$k(E^*) = dN^\dagger(E^* - E_0)/h\rho(E^*) \quad (4.3)$$

where the reaction degeneracy, *d,* is calculated from the ratio of the rotational symmetry numbers of reactants and products, $N^\dagger(E^* - E_0)$ is the sum of rovibrational states of the transition state (TS), and $\rho(E^*)$ is the density of states of the energized molecule at E^*. In the present work, the dissociation channels observed are heterolytic bond cleavages that can be characterized as proceeding over loose TSs equivalent to the product asymptotes.[39] Thus, the TSs are treated at the phase space limit (PSL) in which the transitional modes are rotors.[40] All molecular parameters for the TS and energized molecule are taken from quantum chemical calculations described below.

Cross sections for the loss of an additional hydrazine ligand are modeled by multiplying eq 4.2, which reproduces the cross section of the primary dissociation product, by the probability for further dissociation[41] given by eq 4.4

$$P_{D2} = 1 - e^{-k_2(E_2^*)\tau} \quad (4.4)$$

where $E_2^* = E^* - E_0 - T_1 - E_L$ is the internal energy of the product ion undergoing further dissociation and k_2 is defined analogously to eq 4.3 where the TS corresponds to the second dissociation starting at $E_{0,2}$. Statistical assumptions are used to assign the distributions for T_1 and E_L, which represent the translational energy of the primary products and the internal energy of the neutral product, respectively.

For both primary and secondary processes, the model cross sections of eq 4.2 and eq 4.2 × eq 4.4 are convoluted over the kinetic energy distributions of the neutral and ion

reactants before comparison to experimental data. The fitting parameters in these equations ($\sigma_0, N, and\ E_0$) are then optimized using a nonlinear least-squares criterion to reproduce the experimental data throughout the threshold region. The E_0 threshold energies obtained are equivalent to the 0 K binding energy of the ligand to the proton-bound hydrazine-containing cluster. The uncertainties in these binding energies are determined from the range of parameters obtained from modeling multiple data sets, scaling the vibrational frequencies of reactants and products by ±10%, varying the best fit *N* value by ±0.1, changing the experimental time-of-flight up and down by a factor of 2, and including the uncertainty in the energy scale, ±0.05 eV (lab). In addition, as will be seen below, a number of isomers are potentially populated for each of the species studied. Therefore, the data were analyzed using molecular parameters for any isomer that could conceivably be populated according to one level of theory and the uncertainties in the parameters of eq 4.2 include these variations as well. It was found that changes in the threshold energies as the isomers changed were small: 1.2 kJ/mol for $(N_2H_4)_2H^+$, 1.5 kJ/mol for $(N_2H_4)_3H^+$, 0.5 kJ/mol for $(N_2H_4)_4H^+$, and 0.6 kJ/mol for $(UDMH)_2H^+$.

4.3.3 Computational Details

To obtain stable geometries, vibrational frequencies, and energies for the proton-bound hydrazine clusters and the proton-bound UDMH dimer, theoretical calculations were performed using UCSF Chimera,[42] AMBER,[43] NWChem,[44] and Gaussian 09 Rev. D[45] suites of programs. Possible low-energy conformations of these complexes were explored via a 5000 cycle simulated annealing procedure employing the Amber14SB force field. Briefly, a three-phase molecular dynamic distance-restrained simulated

annealing process was used with each cycle beginning and ending at 100 K. Each cycle lasted for 1.25 ps and achieved a maximum simulation temperature of 1600 K. Heating and cooling times for each cycle were 0.85 ps each, allowing 0.4 ps for the ions to sample conformational space at the simulation temperature. The conformations accessed at the end of each annealing cycle were subjected to a geometry optimization using molecular mechanics minimization every 0.001 ps followed by a quantum mechanics geometry optimization at the HF/6-31G level of theory. Conformations above a relative energy of ~120 kJ/mol were not included in further calculations. Further optimizations of the low-energy conformations were then performed at the B3LYP/6-31G(d) level of theory[46, 47] utilizing the opt = loose criterion (maximum step size of 0.01 au and an RMS force of 0.0017 au).[45] Final geometry optimizations and vibrational calculations were performed at the B3LYP/6-311+G(d,p) level of theory with and without empirical dispersion (ED). Frequencies were scaled by 0.989 to obtain zero-point energy (ZPE) and thermal corrections to 298 K. The ED functions were set to the D3 version of Grimme dispersion[48] (GD3) with Becke–Johnson (BJ) damping for B3LYP and PBE1PBE (PBE0), and GD3[49] for M06 levels of theory. Using ED optimized structures at the B3LYP/6-311+G(d,p) level of theory, single-point energy calculations were performed with a 6-311+G(2d,2p) basis set at B3LYP, M06,[50] PBE0,[51, 52] mPW1PW91,[53-55] MP2(full) (where full indicates correlation of all electrons),[56-60] and CCSD(T)[61-65] (where T indicates perturbative triple excitations) levels. Results with and without ED and with and without basis set superposition error (BSSE) corrections determined at the full counterpoise level[66, 67] were also obtained.

These various levels of theory were chosen for the following reasons. B3LYP and

MP2(full) levels of theory were used for consistency with previous studies of noncovalent interactions.[20-25] The M06[50] and mPW1WP91[54] functionals were included because they are designed to accurately model noncovalent interactions, such as hydrogen bonds, and PBE0 has a similar HF exchange, 25%,[52] to that of the M06 (27%), allowing an assessment of whether this property leads to consistent results. The CCSD(T) level of theory was included to provide a theoretical benchmark for accuracy. Finally, dispersion corrections were utilized when available as these also are designed to improve the description of longer range interactions such as hydrogen bonding.

4.4 Results and Discussion

4.4.1 Theoretical Structures: Dimer

Four low-lying isomers for the proton-bound hydrazine dimer were found and are shown in Figure 4.1, with energies in Table 4.1. All five levels of theory suggest the (D,D)(A,A)g_+ isomer is the ground structure (GS) at 0 K and the GS at 298 K for the M06 and MP2(full) levels of theory. This appears to reproduce the structure located by Lifshitz and co-workers (which they simply called III).[11] Here, our nomenclature indicates that the protonated hydrazine donates a hydrogen bond from both nitrogens (D,D) and the other hydrazine accepts a hydrogen bond at both nitrogens (A,A), where the first letter denotes the protonated N. In addition, the ∠NNNN dihedral angle through the shared proton is specified by using cis (c, for angles between 0°–45°), gauche (g, 45°–135°), or trans (t, 135°–180°) and + or – for the gauche angles when needed to distinguish similar isomers. The PBE0 level of theory suggests the (DD,A)(A,AD)g_- isomer is the GS at 298 K, but other levels of theory suggest this isomer is 0.2–1.5 kJ/mol

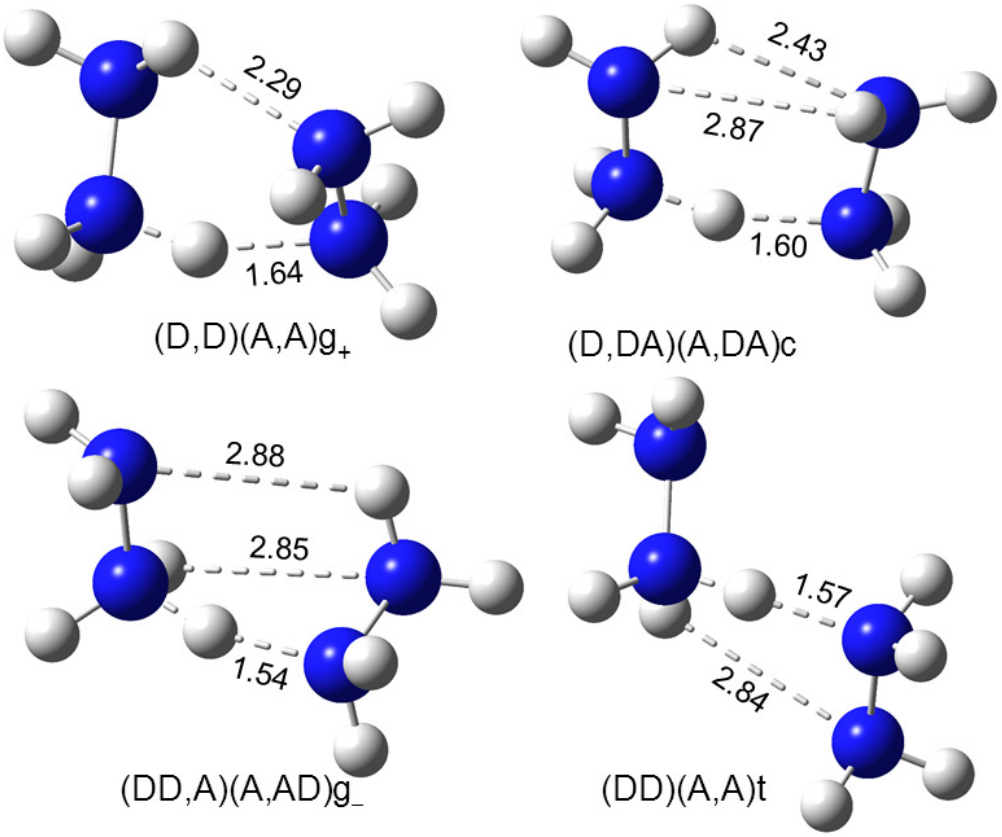

Figure 4.1. The four isomers of $(N_2H_4)_2H^+$ calculated at the B3LYP-GD3BJ/6-311+G(d,p) level of theory. Hydrogen bonds are indicated by dashed lines with distances indicated in Å. In all cases, the protonated hydrazine is located to the left.

Table 4.1. Relative energies at 0 K and free energies at 298 K (kJ/mol) of the potential energy surface coupling the four isomers of proton-bound hydrazine dimer[a]

Structures	B3LYP	M06	mPW1PW91	PBE0	MP2(full)
(D,D)(A,A)g_+	**0.0** (0.3)	**0.0 (0.0)**	**0.0** (2.1)	**0.0** (1.0)	**0.0 (0.0)**
TS g_+/g_-	-3.4 (-3.6)	-2.7 (-3.1)	-5.7 (-6.0)	-5.6 (-6.0)	-1.4 (-1.8)
(DD,A)(A,AD)g_-	1.9 (0.2)	3.6 (1.5)	0.5 (0.5)	1.0 **(0.0)**	2.1 (0.8)
TS g_-/t	11.2 (15.1)	9.3 (9.5)	11.1 (13.3)	11.7 (13.0)	10.8 (11.0)
(DD)(A,A)t	4.5 (0.6)	7.8 (3.6)	2.2 **(0.0)**	3.9 (0.7)	5.1 (0.9)
TS t/c	6.1 (5.7)	11.2 (10.5)	3.2 (4.6)	5.4 (5.7)	7.7 (7.0)
(D,DA)(A,DA)c	0.8 **(0.0)**	2.6 (1.6)	0.3 (1.3)	0.7 (0.7)	1.5 (0.5)
TS g_+/c	12.6 (12.0)	16.1 (15.3)	10.4 (11.6)	12.8 (13.0)	12.7 (11.9)

[a] Free energies in parentheses. Ground structure in bold. All values calculated at the level of theory indicated with empirical dispersion included for B3LYP, M06, and PBE0 levels of theory using the 6-311+G(2d,2p) basis set with structures, zero-point energies, and thermal energies calculated at B3LYP-GD3BJ/6-311+G(d,p) level of theory.

higher in energy at 298 K. The B3LYP level of theory suggests the (D,DA)(A,DA)c isomer is the GS at 298 K, but it is 0.5–1.6 kJ/mol higher in energy at 298 K at other levels of theory. Finally, mPW1PW91 indicates the last isomer located, (D,D)(A,A)t, is the 298 K GS, an isomer 0.6–3.6 kJ/mol higher at other levels of theory. In these four isomers, the average short NH bond to the bound proton is 1.11 Å, whereas the average long NH bond is 1.58 Å. All four isomers have additional H-bonding interactions ranging in length from 2.29 to 2.88 Å.

Because the relative energies of all four isomers at 298 K are small, a Maxwell–Boltzmann population distribution at 298 K for the (D,D)(A,A)g_+, (DD,A)(A,AD)g_-, (D,DA)(A,DA)c, and (DD)(A,A)t, isomers is 15%–43%, 22%–31%, 21%–28%, and 10%–35%, respectively. Thus, it seems likely that all four isomers are populated at room temperature. The difference in relative energies from 0 to 298 K is linked to the entropy and extent of hydrogen bonding. As mentioned above, Dyczmons[12] found six conformations for the neutral hydrazine dimer, whereas we locate only four for the proton-bound analogue. This difference is simplistically accounted for by the protonation site, which can only donate a hydrogen bond, restricting the number of isomers. Prior to protonation, this site could either donate or accept a hydrogen bond.

Because population of all four isomers of $(N_2H_4)_2H^+$ at room temperature seems likely, we explored the potential energy surface (PES) that allows these isomers to interconvert. This PES is shown in Figure 4.2, where the names of the four isomers have been simplified to designating the ∠NNNN dihedral angle. Table 4.1 lists 0 and 298 K energies for all TSs. Interestingly, after ZPE and thermal corrections, TS g_+/g_- becomes lower in energy than either g_+ or g_-. This TS corresponds primarily to proton exchange

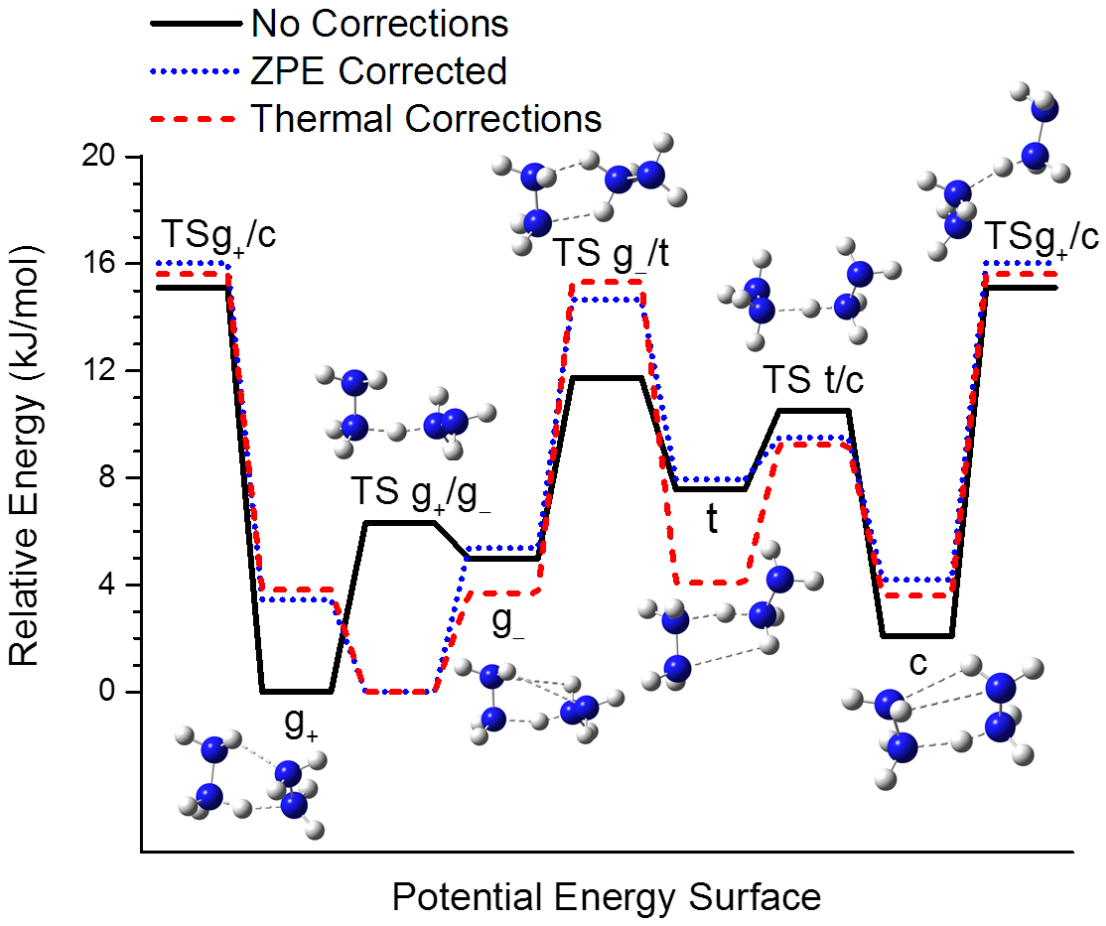

Figure 4.2. Potential energy surfaces for interconversion of the four isomers of $(N_2H_4)_2H^+$, equilibrium (black line), 0 K (blue dotted line), and 298 K (red dashed line) surfaces are shown calculated at the B3LYP-GD3BJ/6-311+G(d,p) level of theory. Hydrogen bonds are indicated by dashed lines.

between the two hydrazines, coupled with small rotations. Because the proton motion is high in frequency, the zero-point energy level of this double-well potential lies above the TS on the equilibrium surface such that the g_+ and g_ isomers should rapidly interconvert at all temperatures. The t and c isomers are coupled by TS t/c, which lies 4.6–10.5 kJ/mol higher in energy at 298 K, such that interchange between these isomers is possible at room temperature. In contrast, TS g_+/c and TS g_/t are sufficiently high in energy, >9 kJ/mol, that interchange between the t and c isomers and the g_ and g_+ isomers is unlikely at room temperature. Finally, we note that TS g_/t is similar to the saddle point found by Dyczmons for the neutral hydrazine dimer.[12]

4.4.2 Theoretical Structures: Trimer and Tetramer

For the larger protonated hydrazine clusters, our nomenclature again designates the donor (D)/acceptor (A) character of the two nitrogens of the protonated hydrazine followed by those for the other hydrazines, each in parentheses. Interactions between unprotonated hydrazines are indicated by a prime symbol (′). For $(N_2H_4)_3H^+$, the (DD,D)(A,A′)(A,AD′)g_c isomer (Figure 4.3) is the GS at 0 K at all levels of theory, Table 4.2, and the GS at 298 K for the B3LYP and PBE0 levels of theory. At the M06 and MP2(full) levels of theory, this isomer is 0.4–1.2 kJ/mol higher in energy at 298 K than the (DD,DD)(A,A)(A,A)C_2[VI] isomer (where C_2 indicates its symmetry), which B3LYP and PBE0 predicts is 0.6–1.2 kJ/mol above their GS at 298 K, respectively. This isomer appears to resemble the VI species located by Lifshitz and co-workers,[11] who also found (D,D)(AD′,A′)(AD′,A′)[IV] and (DD)(A,D′)(A,A′)[V], which we calculate are 5–11 and 2–12 kJ/mol, respectively, above the GS.[11] The mPW1PW91 level of theory

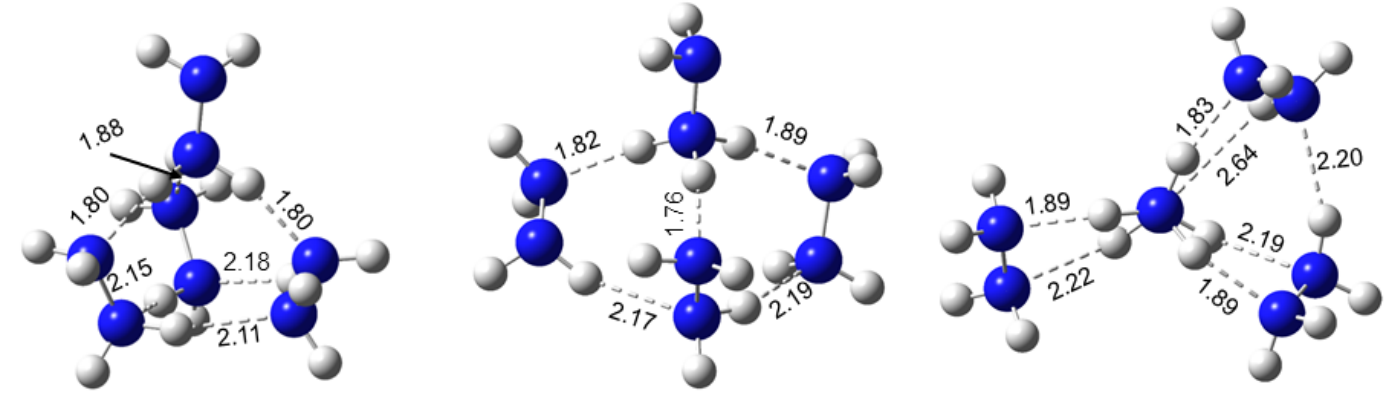

Figure 4.4. The low-lying isomers of $(N_2H_4)_4H^+$ calculated at the B3LYP-GD3BJ/6-311+G(d,p) level of theory. Hydrogen bonds are indicated by dashed lines with distances indicated in Å. In all cases, the protonated hydrazine is located at the top.

Table 4.2. Relative energies at 0 K and free energies at 298 K (kJ/mol) for low-lying conformers of the proton-bound hydrazine trimer and tetramer complexes[a]

Structures	B3LYP	M06	mPW1PW91	PBE0	MP2(full)
$(N_2H_4)_3H^+$					
(DD,D)(A,A′)(A,AD′)g_c	**0.0 (0.0)**	**0.0** (0.4)	**0.0** (2.2)	**0.0 (0.0)**	**0.0** (1.2)
(DD,D)(A,A′)(A,AD′)g_+c	1.4 (1.0)	2.3 (2.3)	1.6 (3.4)	1.6 (1.2)	1.7 (2.5)
(DD,DA)(A,DA′)(A,AD′)cc	1.7 (1.1)	3.1 (3.0)	2.3 (4.0)	2.0 (1.5)	2.1 (2.7)
(DD,DA)(A,DA′)(A,AD′)g_c	3.1 (3.6)	2.7 (3.6)	3.7 (6.4)	3.0 (3.5)	3.1 (4.8)
(DD,DD)(A,A)(A,A)C_2[VI]	4.7 (1.2)	3.1 **(0.0)**	1.9 (0.6)	4.6 (1.2)	2.3 **(0.0)**
(DD,D)(A,A′)(A,AD′)tc	5.1 (1.6)	6.6 (3.6)	4.8 (3.5)	5.4 (1.9)	5.7 (3.4)
(DD,DDA)(A,A)(A,AD)cg_	5.6 (1.2)	6.7 (2.7)	2.2 **(0.0)**	5.5 (1.2)	4.2 (1.0)
(DD,DD)(A,A)(A,A)cc	6.4 (1.7)	8.2 (4.0)	3.3 (0.9)	6.8 (2.1)	7.1 (3.6)
(D,D)(AD′,A′)(AD′,A′)[IV]	6.5 (6.9)	10.0 (10.8)	5.4 (8.0)	5.0 (5.4)	8.5 (10.1)
(DD)(A,D′)(A,A′)[V]	10.1 (4.2)	17.2 (11.7)	6.1 (2.3)	9.7 (3.8)	11.1 (6.4)
$(N_2H_4)_4H^+$					
(DDD)(A,D′A′)(A,D′A′)(A,D′A′)gtt	**0.0 (0.0)**	**0.0** (4.0)	**0.0** (0.5)	**0.0 (0.0)**	**0.0** (2.1)
(DD,D)(AD′,A′)(AD′,A′)(A,D′A′)	2.7 (5.2)	4.1 (10.6)	4.7 (7.7)	2.7 (5.2)	4.2 (8.8)
(DDD,DDA)(A,A)(A,AD′)(A,DA′)	5.8 (1.2)	0.5 **(0.0)**	4.1 (0.1)	6.5 (2.0)	2.5 **(0.0)**
(DDD)(A,D′)(A,D′A′)(A,A′)	8.2 (2.7)	10.1 (8.5)	5.1 **(0.0)**	7.9 (2.4)	6.5 (3.1)
(DDD)(A,D′A′)(AD′,D′A′)(A,A′)	9.1 (4.6)	9.3 (8.8)	6.5 (2.5)	8.9 (4.4)	7.6 (5.2)
(DDD)(A,D′A′)(A,D′A′)(A,D′A′)ttt	20.1 (10.5)	23.6 (18.0)	15.2 (6.1)	19.7 (10.0)	19.4 (11.8)

[a]Free energies in parentheses. Ground structure in bold. All values calculated at the level of theory indicated with empirical dispersion included for B3LYP, M06, and PBE0 levels of theory using the 6-311+G(2d,2p) basis set with structures, zero-point energies, and thermal energies calculated at B3LYP-GD3BJ/6-311+G(d,p) level of theory.

suggests the (DD,DDA)(A,A)(A,AD)cg_ isomer is the GS at 298 K, whereas the other levels of theory predict this isomer is 1.0–2.7 kJ/mol above their GS. All levels of theory predict an additional four isomers (shown in Figure 4.S1) lie within 6 kJ/mol of the GS at 298 K. As for the dimer, it is clear that multiple isomers are probably populated at 298 K. The (D,D)(AD′,A′)(AD′,A′)[IV] and (DD,DA)(A,DA′)(A,AD′)g_c isomers are sufficiently high in energy (> 3.5 kJ/mol) at all levels of theory that their populations are likely to be negligible at 298 K.

For the hydrazine tetramer, the (DDD)(A,D′A′)(A,D′A′)(A,D′A′)gtt isomer (Figure 4.4) is the GS at 0 K at all levels of theory, and the GS at 298 K for B3LYP and PBE0 levels of theory, Table 4.2. The M06 and MP2(full) levels predict this isomer is 2.1–4.0 kJ/mol higher in energy than the (DDD,DDA)(A,A)(A,AD′)(A,DA′) isomer at 298 K. The mPW1PW91 level of theory suggests (DDD)(A,D′)(A,D′A′)(A,A′) is the GS at 298 K, whereas other levels of theory predict this isomer is 2.4–8.5 kJ/mol higher in energy at 298 K. The next lowest energy isomer is (DDD)(A,D′A′)(AD′,D′A′)(A,A′), which lies 2.5–8.8 kJ/mol higher in energy than the GS at 298 K, meaning it could have a notable population at this temperature. All levels of theory find that two additional isomers, (DD,D)(AD′,A′)(AD′,A′)(A,D′A′) and DDD)(A,D′A′)(A,D′A′)(A,D′A′)ttt, are 5–11 and 6–18 kJ/mol, respectively, higher in energy at 298 K, suggesting their populations are likely to be negligible (<10%). Notably, we were unable find the two isomers suggested by Lifshitz and co-workers.[11] Attempts to find such geometries at both RHF/6-31G(d) and B3LYP/6-311+G(d,p) levels of theory were made.

On the basis of their theoretical exploration of the proton-bound hydrazine trimer and tetramer, Lifshitz and co-workers[11] suggested that these clusters formed open-chain

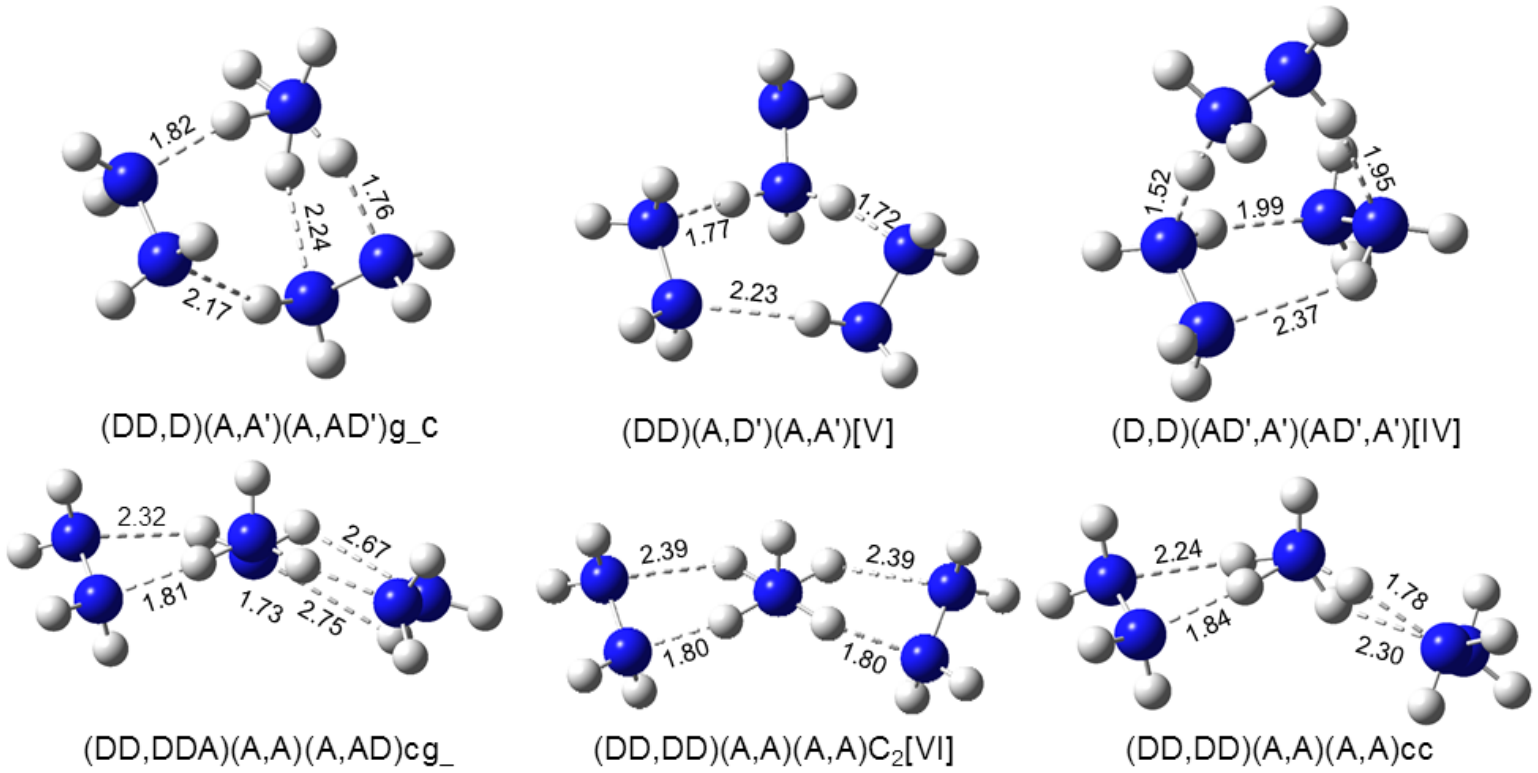

Figure 4.3. The low-lying isomers of $(N_2H_4)_3H^+$ calculated at the B3LYP-GD3BJ/6-311+G(d,p) level of theory. Hydrogen bonds are indicated by dashed lines with distances indicated in Å. In all cases, the protonated hydrazine is located at the top. Roman numeral in brackets indicate closest isomers to those found in reference [9].

isomers, although the criterion used to evaluate this was not explicitly stated. Our higher-level theoretical results clearly show that these clusters prefer cyclic structures. This conclusion considers that an open-chain isomer should have no H–bonding interactions between the unprotonated hydrazine molecules, such that only the (DD,DDA)(A,A)(A,AD)cg_, (DD,DD)(A,A)(A,A)C_2[VI], and (DD,DD)(A,A)(A,A)cc isomers correspond to open-chain motifs.

4.4.3 Theoretical Structures: UDMH Dimer

For $[(CH_3)_2N_2H_2]_2H^+$, isomers are named by using α for the protonated and methylated N and β for the protonated and unmethylated N. The four lowest-energy isomers found are shown in Figure 4.5, with an additional seven isomers shown in Figure 4.S3. All energies are listed in Table 4.3. All five levels of theory suggest that the (D_α,D)(A_α,A)g_+ isomer is the GS at 0 K, but only the M06 level of theory suggests this isomer is the GS at 298 K. The other levels of theory find the (D_α,DA)(A_α,DA)c isomer is the GS at 298 K and only 0.1–0.7 kJ/mol higher in energy than the GS at 0 K. Both isomers share the proton between the methylated nitrogens and have an additional hydrogen bonding interaction between the unmethylated nitrogens. The ($D\alpha$,A)($A\alpha$,D)g_- isomers low-lying, 1.5–2.6 and 2.1–2.6 kJ/mol above the GS at 0 and 298 K, respectively. The (D_α)(A_α)t isomer is 4.2–6.2 kJ/mol higher in energy at 0 K but only ~1 kJ/mol higher at 298 K because the lack of the additional hydrogen bonding raises the energy but allows a more flexible structure. Thus, these four isomers are likely to be populated at room temperature.

As for the proton-bound hydrazine dimer, the (D_α,D)(A_α,A)g_+ and

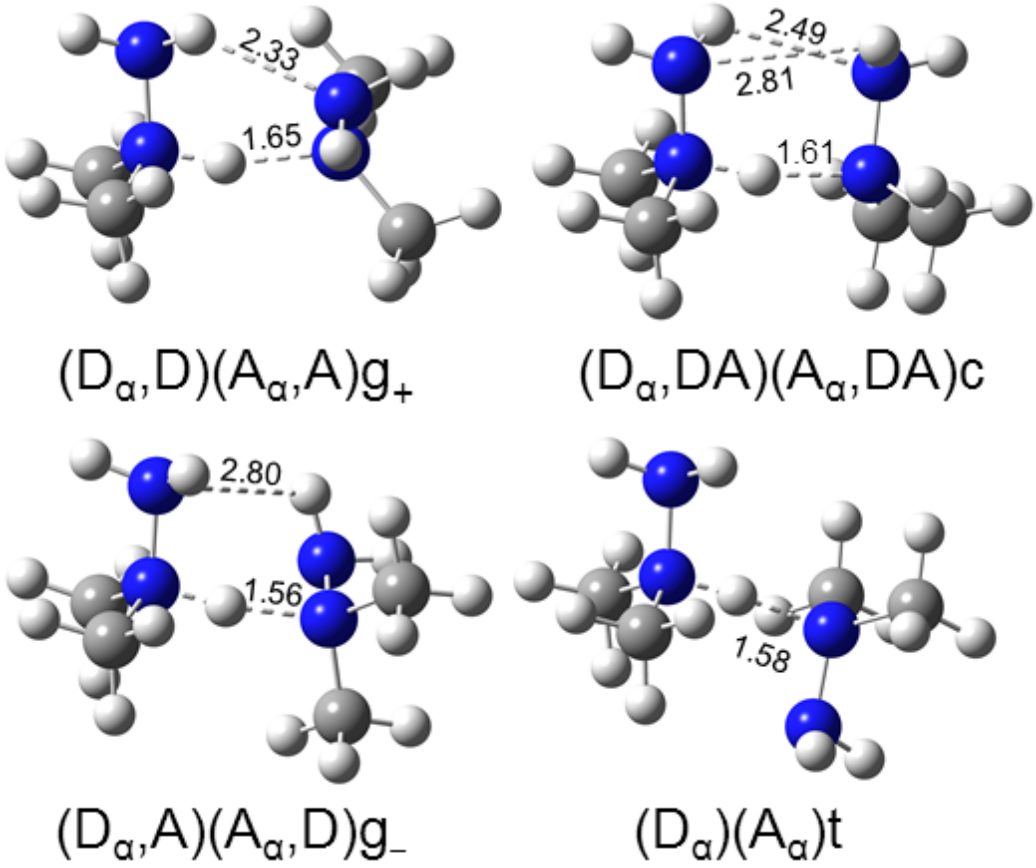

Figure 4.5. The low-lying isomers of $[(CH_3)_2N_2H_2]_2H^+$ calculated at the B3LYP-GD3BJ/6-311+G(d,p) level of theory. Hydrogen bonds are indicated by dashed lines with distances indicated in Å. In all cases, the protonated UDMH is located to the left.

Table 4.3. Relative energies at 0 K and free energies at 298 K (kJ/mol) for low-lying conformers of the proton-bound UDMH dimer[a]

Structures	B3LYP	M06	mPW1PW91	PBE0	MP2(full)
$(D_\alpha,D)(A_\alpha,A)g_+$	**0.0** (1.8)	**0.0 (0.0)**	**0.0** (2.0)	**0.0** (1.8)	**0.0** (1.4)
TS g_+/g_-	-3.3 (-1.3)	-2.6 (-2.3)	-3.8 (-1.5)	-5.3 (-3.3)	-3.4 (-1.8)
$(D_\alpha,A)(A_\alpha,D)g_-$	2.1 (2.6)	3.7 (2.5)	1.7 (2.4)	1.5 (2.1)	2.3 (2.5)
$(D_\alpha,DA)(A_\alpha,DA)c$	0.3 **(0.0)**	2.6 (0.5)	0.1 **(0.0)**	0.3 **(0.0)**	0.7 **(0.0)**
$(D_\alpha)(A_\alpha)t$	4.5 (1.0)	6.2 (0.9)	4.2 (1.0)	4.3 (0.9)	4.9 (1.0)
$(D_\alpha,D)(A_\alpha,A)c$	9.4 (13.8)	9.8 (12.3)	9.1 (13.7)	9.9 (14.3)	8.7 (12.7)
$(D_\alpha,D)(A_\beta,A)g$	6.0 (6.8)	4.1 (3.2)	4.7 (5.8)	6.3 (7.2)	8.4 (8.9)
$(D_\alpha,D)(A_\beta,A)c$	7.0 (6.9)	5.9 (3.5)	4.9 (5.1)	7.1 (7.1)	9.5 (9.1)
$(D_\alpha)(A_\beta)t$	10.7 (8.0)	10.1 (5.6)	7.2 (4.8)	10.2 (7.6)	14.5 (11.4)
$(D_\beta)(A_\beta)g$	29.5 (29.4)	25.9 (24.1)	21.8 (22.0)	25.9 (25.9)	40.1 (39.7)
$(D_\beta)(A_\beta)c$	28.3 (29.4)	25.3 (24.6)	21.7 (23.0)	24.7 (25.8)	38.3 (39.0)
$(D_\beta)(A_\beta)t$	32.3 (27.7)	29.6 (23.3)	22.6 (18.3)	28.9 (24.4)	41.3 (36.4)

[a]Free energies in parentheses. Ground structure in bold. All values calculated at the level of theory indicated with empirical dispersion included for B3LYP, M06, and PBE0 levels of theory using the 6-311+G(2d,2p) basis set with structures, zero-point energies, and thermal energies calculated at B3LYP-GD3BJ/6-311+G(d,p) level of theory.

(D_α,A)(A_α,D)g_- isomers interconvert via TS g_+/g_-, which becomes lower in energy than either g_+ or g_- after ZPE and thermal corrections are included (Table 4.3). For these four low-lying (D_α)(A_α) isomers, the average short NH bond to the bound proton is 1.11 Å, whereas the average long NH bond is 1.60 Å. Three of the isomers have additional H-bonding interactions at the unmethylated nitrogens with NH bond distances of 2.33–2.81 Å. Note that the hydrogen bonds are slightly longer (by ~0.02 Å) than in the unmethylated dimer, perhaps because of repulsive steric interactions. The proton can also be shared between one methylated and one unmethylated nitrogen (D_α)(A_β). Three isomers result and lie 3–11 kJ/mol higher in energy than the GS at 298 K. Sharing the proton between both unmethylated nitrogens (D_β)(A_β) increases the energy further, in part because there can be no hydrogen bonding between the methylated nitrogens. These three structures lie more than 18 kJ/mol above the GS. Neither of the last two types of structures should exhibit appreciable population at 298 K.

4.4.4 Experimental Results

Experimental cross sections for CID with Ar were measured for $(N_2H_4)_nH^+$ where n = 2–4 and the proton-bound UDMH dimer and are shown in Figure 4.6a–d after extrapolation to zero pressure. In all cases, the dominant fragment is loss of a hydrazine (or UDMH) molecule, with the n = 3 and 4 complexes showing sequential dissociation of a second hydrazine ligand as well. Analysis of all of these complexes using eq 4.2 and eq 4.2 × eq 4.4 yields optimized parameters listed in Table 4.4. In all cases, it can be seen that the model reproduces the cross sections of both the primary and secondary products with fidelity throughout the threshold regions and up to at least 2–4 eV. For the n = 2

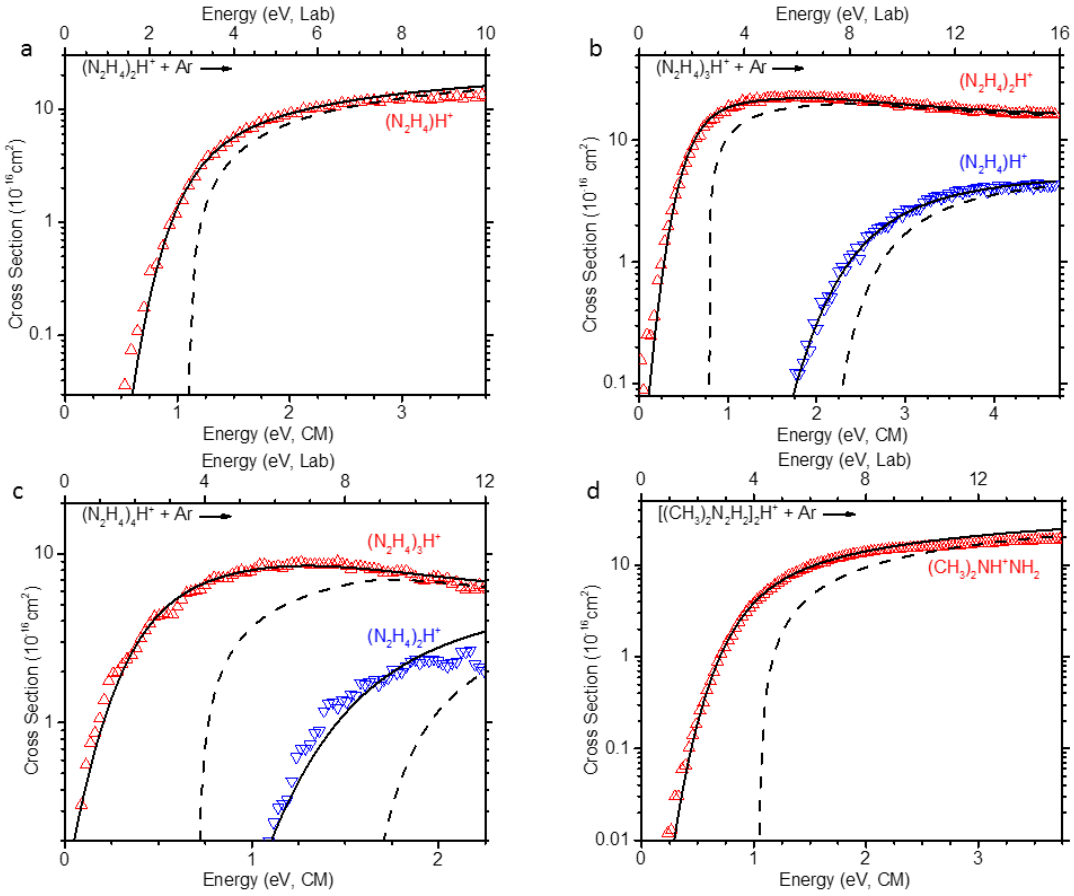

Figure 4.6. Zero pressure extrapolated cross sections for the CID with Ar of $(N_2H_4)_nH^+$ for n = 2–4 (parts a–c) and for $[(CH_3)_2N_2H_2]_2H^+$ (part d). Solid lines show the best fit to the primary (open red triangles) and secondary (open blue inverted triangles) product cross sections using eq 4.2 × eq 4.4 convoluted over the kinetic and internal energy distributions of the reactants. Dashed lines show the models in the absence of experimental kinetic energy broadening for reactants with an internal energy of 0 K. Optimized parameters for these models are found in Table 4.4.

Table 4.4. Optimized parameters of Equation 4.2 from Analysis of CID Cross Sections[a]

reactant	product	σ_0[b]	N[b]	E_0 (PSL, eV)[b]	$\Delta S^{\dagger}_{1000}$ (J/mol K)
$(N_2H_4)_2H^+$	$(N_2H_4)H^+$	19.6 (0.3)	1.0 (0.1)	1.17 (0.03)	55 (5)
$(N_2H_4)_3H^+$	$(N_2H_4)_2H^+$	36.2 (5.5)	0.8 (0.1)	0.76 (0.04)[c]	73 (5)
	$(N_2H_4)H^+$	21.5 (5.5)		2.05 (0.06)[c]	64 (3)
$(N_2H_4)_4H^+$	$(N_2H_4)_3H^+$	13.1 (1.9)	1.0 (0.1)	0.71 (0.05)[c]	73 (5)
	$(N_2H_4)_2H^+$	11.9 (2.0)		1.53 (0.06)[c]	68 (5)
$[(CH_3)_2N_2H_2]_2H^+$	$(CH_3)_2NH^+NH_2$	20.7 (0.5)	1.4 (0.1)	1.03 (0.03)	70 (5)

[a] Uncertainties in parentheses. [b] Parameters for modeling where lifetime effects are taken into account. [c] Sequential dissociation modeling using eq 4.2 × eq 4.4.

complex, the threshold for a loss of a single hydrazine molecule is 1.17 ± 0.03 eV. When the sequential model, eq 2 × eq 4, is used for n = 3, we measure a threshold of 0.76 ± 0.045 eV for the primary dissociation channel and require 2.05 ± 0.06 eV for the sequential loss of an additional hydrazine. The difference between the primary and secondary thresholds should equal the $(N_2H_4)H^+$–(N_2H_4) bond energy, and is 1.29 ± 0.06 eV, somewhat higher than the primary threshold for n = 2. For, the n = 4 complex, Figure 4.6c, a primary threshold of 0.71 ± 0.05 eV and a sequential threshold of 1.53 ± 0.06 eV yield a difference of 0.82 ± 0.06 eV, which agrees well with the primary dissociation threshold of 0.76 ± 0.04 eV from n = 3, Figure 4.6c. For the proton-bound UDMH dimer, the analysis of the cross section, Figure 4.6d, yields a threshold of 1.03 ± 0.03 eV for a loss of a UDMH molecule, similar to but slightly smaller than the unmethylated dimer.

In addition to the products above, the two dimer ions exhibited additional fragmentations corresponding to the dissociation of the protonated monomers at higher energies than shown in Figures 4.6a and 4.6d. In both cases, these products' ions have cross sections that are too small to be analyzed accurately and require >4 eV CM frame energy. These dissociations can be examined much more accurately from CID studies of the protonated monomers, work that is ongoing. We also note that the probability of $(N_2H_4)_4H^+$ dissociating into $(N_2H_4)_3H^+$ at room temperature exists even at a collision energy of 0 eV. This indicates that the BDE of the fourth hydrazine in $(N_2H_4)_4H^+$ is comparable to the average internal energy, 0.35 eV, for this complex. Lifshitz and co-workers have measured that the fifth hydrazine binds by only 0.38 eV,[11] which explains why we were unable to create $(N_2H_4)_5H^+$ or larger complexes at 298 K. Likewise, larger proton-bound UDMH clusters were not formed in our source. Clearly, methylation limits

the extent of strong hydrogen bonding, such that the higher order $(UDMH)_nH^+$ clusters will be weakly bound.

4.4.5 Comparison of Experimental and Theoretical Bond Energies: $(N_2H_4)_nH^+$ (n = 2–4) and $[(CH_3)_2N_2H_2]_2H^+$

There is reasonable agreement between the primary and secondary bond energies determined using the sequential model but in general, the primary thresholds provide the best experimental information as fewer assumptions associated with the modeling are needed. Therefore, these are our best experimental BDEs for the $(N_2H_4)_nH^+$ complexes where n = 2–4 and $(UDMH)_2H^+$, as listed in Table 4.5.

For comparison, the average theoretical BDEs weighted by their Maxwell–Boltzmann population associated with their relative energies at each level of theory are also included in Table 4.5 and shown in Figure 4.7. BSSE corrections were relatively small for B3LYP, M06, mPW1PW91, and PBE0 levels (<5 kJ/mol), whereas corrections for MP2(full) and CCSD(T) were larger, 7–15 kJ/mol. The BSSE corrections with and without ED functions are nearly identical. Overall, theory predicts BDEs in reasonable agreement with experiment with mean absolute deviations (MADs) ranging from ~3 to 12 kJ/mol. These differences are somewhat larger than the mean experimental uncertainty of ~3 kJ/mol, except for the PBE0 and M06 levels of theory without ED, which provide the best agreement with experiment. MAD values for PBE0 and M06 without ED are very similar, perhaps because they utilize similar HF exchange functions. The MAD for mPW1PW91 is only slightly worse, perhaps because it shares the same functional for noncovalent bonds as M06. MP2(full) and CCSD(T) yield similar MADs once BSSE

Table 4.5. Comparison of experimental 0 K bond energies (kJ/mol) to theoretical values[a]

	expt[b]	*lit.*[c]	B3LYP[d]		M06[d]		mPW1PW91[d]		PBE0[d]		MP2(full)[d]		CCSD(T)[e]	
$(N_2H_4)_{n-1}H^+$-(N_2H_4)														
$n = 2$	113.3 ± 2.7	135.1 ± 8.1	104.7	(107.1)	110.7	(113.4)	108.3	(111.1)	111.9	(114.7)	106.4	(115.3)	101.7	(111.8)
			116.3[f]	(118.6)[f]	112.7[f]	(115.4)[f]			118.6[f]	(121.3)[f]				
3	72.4 ± 3.5	75.3 ± 4.5	69.0	(70.9)	81.0	(83.5)	73.3	(75.3)	73.0	(75.3)	77.6	(86.6)	76.5	(83.2)
			82.8[f]	(85.0)[f]	84.1[f]	(86.7)[f]			86.5[f]	(89.2)[f]				
4	68.3 ± 4.6	59.8 ± 3.6	58.2	(60.4)	68.3	(70.6)	60.1	(62.9)	60.6	(63.3)	64.1	(72.6)	65.8	(73.7)
			72.4[f]	(74.8)[f]	70.8[f]	(73.1)[f]			73.1[f]	(75.9)[f]				
$[(CH_3)_2N_2H_2]_{n-1}H^+$-$(CH_3)_2N_2H_2)$														
2	99.4 ± 2.9		85.3	(88.0)	99.2	(102.8)	90.6	(93.7)	95.5	(98.5)	103.7	(117.5)	94.0	(108.6)
			109.3[f]	(111.9)[f]	105.2[f]	(108.8)[f]			110.3[f]	(113.3)[f]				
MAD[g]	3.4[h]	5.4[h]	9.1	(6.8)	2.9	(4.2)	5.7	(4.1)	3.4	(2.6)	5.2	(9.7)	5.9	(6.7)
			6.9[f]	(9.2)[f]	5.2[f]	(7.7)[f]			7.8[f]	(11.6)[f]				

[a] Theoretical values with (and without) BSSE corrections. [b] Primary threshold energies from Table 4.4. [c] Literature values from Reference 11. [d] Population weighted average BDEs for low-lying isomers calculated at the indicated level using a 6-311+G(2d,2p) basis set and B3LYP-GD3BJ/6-311+G(d,p) optimized geometries. [e] BDE for lowest-lying 0 K isomer calculated at the CCSD(T)/6-311+G(2d,2p)//B3LYP-GD3BJ/6-311+G(d,p) level of theory. [f] Empirical dispersion included. [g] Mean absolute deviations from experimental TCID BDEs. [h] Mean experimental uncertainty.

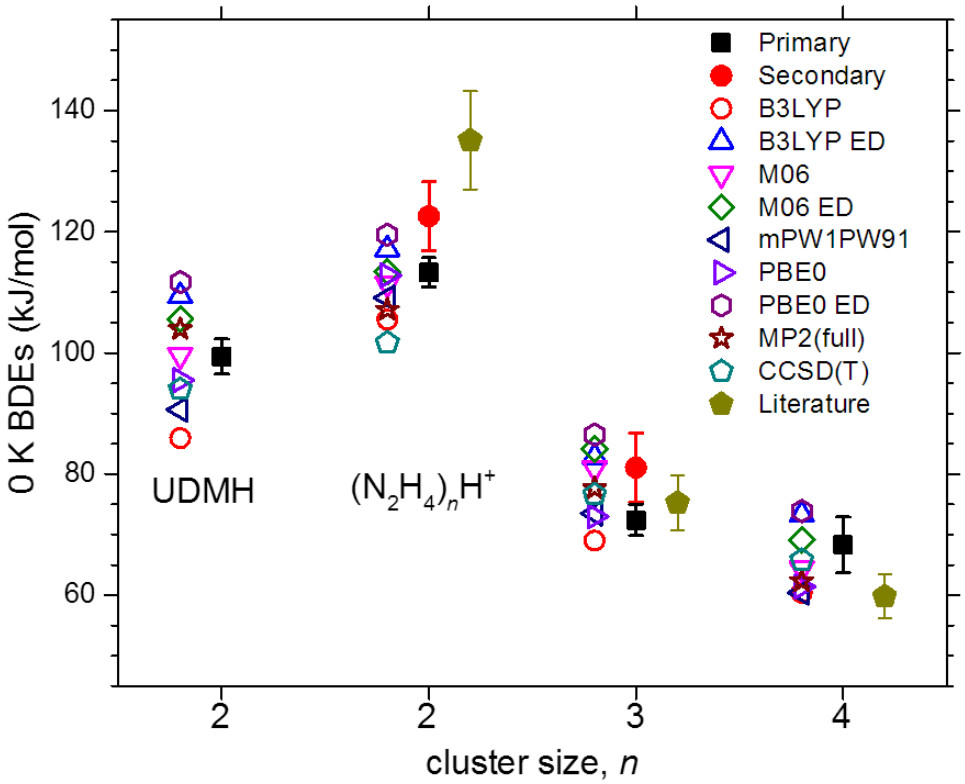

Figure 4.7. Comparison of 0 K bond energies for the proton-bound UDMH dimer and $(N_2H_4)_nH^+$ (n = 2–4) obtained from experiment (primary thresholds, solid black squares; secondary thresholds, solid red circles; literature, solid gold pentagon) and theory (open symbols). All results are from Table 4.5. Data points for theory and literature values have been offset for clarity.

corrections are included and similar to that for mPW1PW91. B3LYP performs poorly compared to the other levels of theory tried. Although addition of dispersion corrections improves the agreement of B3LYP with BSSE, it adversely affects the M06 and PBE0 calculations, which seems odd given that ED is designed to treat H-bonding more accurately. BSSE corrections are generally advantageous except for B3LYP and PBE0 calculations without ED and mPW1PW91. Overall, the M06 and PBE0 levels of theory appear to be more accurate and cost effective than other DFT approaches and the higher levels of theory for these systems.

4.4.6 Comparison to Literature Experimental and Theoretical Values

Figure 4.7 also compares the present experimental results to the KERD values, Table 4.5, obtained by Lifshitz and co-workers.[11] The KERD values for $n = 3$ and 4 agree fairly well with our TCID experimental values presented here, whereas for $n = 2$, their value is higher by 0.23 ± 0.08 eV (22 ± 8 kJ/mol). Lifshitz and co-workers also performed quantum mechanical calculations at the RHF/6-31G(d) level of theory and found the $n = 2$ theoretical value to be 1.23 eV (119 kJ/mol), well above the present experimental and theoretical values. For $n = 3$, their theoretical value of 0.82 eV (79 kJ/mol) agrees well with their KERD BDE of 0.78 eV (75.2 kJ/mol) as well as most values in Table 4.5. In contrast, their theoretical value for the $n = 4$ complex is 0.83 eV (80 kJ/mol), considerably above their experimental value and those in Table 4.5.

4.4.7 Comparison between the Proton-Bound Dimers

As noted above, the 0 K BDE of the proton-bound UDMH dimer is 14 ± 4 kJ/mol lower in energy than the unmethylated dimer. A reviewer notes that because the proton affinity (PA) of the methylated monomer is larger than the unmethylated analogue (by 73.9 kJ/mol),[68] a stronger bond for the UDMH dimer might have been anticipated. Such trends have been investigated previously and nicely explored by Meot-Ner.[69] Because the formation of the hydrogen bonds connecting proton-bound homodimers involves partial proton transfer from the donor to the acceptor, the bond strength is correlated with the efficiency of the proton transfer. Thus, the higher the PA of the monomer, the less efficient the proton transfer, such that an inverse trend is found between the PAs of the monomers and the BDEs of the proton-bound homodimers. In a comprehensive review, Meot-Ner documents these effects for stepwise methylation of NH_3.[69] These values are listed in Table 4.6 and shown in Figure 4.8 along with our experimental BDEs for comparison. It can be seen that the effect of dimethylation on NH_3 and N_2H_4 is very similar, with increases of 76 and 74 kJ/mol, respectively, in the PAs and decreases of 11 and 14 kJ/mol, respectively, in the BDEs (as also indicated by the similar slopes of the correlations in Figure 4.8). Notably, the addition of an NH_2 group to NH_3 and $(Me)_2NH$ has a small affect, 0.3 and 2.6 kJ/mol, respectively, on the PAs of the monomers. This shows that the NH_2 group has a smaller inductive effect than CH_3, as has been shown elsewhere.[70-72] In contrast, addition of the NH_2 group has a greater effect on the BDEs, increasing them by 7.9 and 5.3 kJ/mol, respectively. This increase is a result of additional NH•N hydrogen bonds, as shown in Figures 4.1 and 4.5. This conclusion is emphasized by noting that the increase in the BDEs between the proton-bound NH_3 and hydrazine

Table 4.6. Representative thermochemistry (kJ/mol) of select homodimers

Monomer (B)	Proton Affinity (B)[a]	BDEs (BH^+–B)[b]
NH_3	853.5	107.5[b,c]
$MeNH_2$	899.1	98.4[b,d]
$(Me)_2NH$	929.7	94.1[b,d]
$(Me)_3N$	948.9	93.3[b,f]
N_2H_4	853.2	113.3[f]
$(CH_3)_2N_2H_2$	927.1	99.4[f]

[a] Values from Ref. 68. [b] Values taken from Ref. 69.

[c] Average value from Refs. 73-76. [d] Average value from Refs. 77 and 78.

[e] Average value from Refs. 77-80.

[f] Experimental values from this work (Table 4.4).

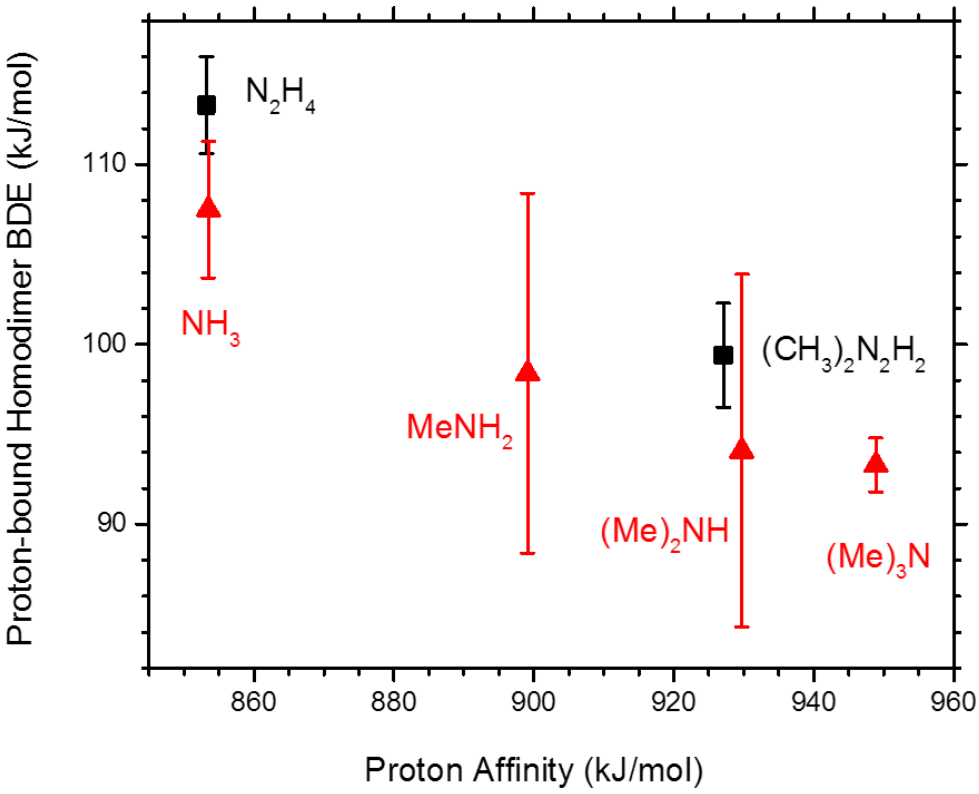

Figure 4.8. Inverse trend between the proton affinities of the neutral monomer (Ref. 69) and the bond dissociation energies of the proton-bound homodimers of substituted hydrazines (current experimental values, solid black squares) and of substituted ammonia (Ref. 70, solid red triangles).

homodimers is comparable to the computed relative energy difference of 2.2–7.8 kJ/mol (Table 4.1) between the g_+ (with H-bonds between NH_2 groups) and t (without these additional H-bonds) isomers of the $(N_2H_4)_2H^+$ dimer. Likewise, these isomers differ in energy by 4.2–6.2 kJ/mol (Table 4.3) for the g_+ and t isomers of $(UDMH)_2H^+$. (Notably the M06 level of theory predicts the experimentally observed differences better than other levels of theory.)

4.4.8 Conversion from 0 to 298 K Thermodynamics

A rigid rotor/harmonic oscillator approximation was applied to convert the 0 K bond energies into 298 K enthalpies. This was achieved using the theoretical vibrational frequencies scaled by 0.989 and rotational constants of the complexes. The uncertainties in these conversions were obtained by scaling the vibrational frequencies up and down by 10%. These conversion factors were used to determine ΔH_{298} and ΔG_{298} values listed in Table 4.7. Note that this approximation may not be suitable for all cases because of the inaccuracy of low-frequency torsional motions.

4.5 Conclusion

Energy-resolved threshold collision-induced dissociation with Ar is performed on $(N_2H_4)_nH^+$ where n = 2–4 and the proton-bound UDMH dimer. The primary dissociation pathway of the n = 2–4 reactants is a loss of a single hydrazine (or UDMH) molecule followed by the sequential loss of an additional hydrazine molecule, for n = 3 and 4, at higher collision energies. Statistical analysis of the TCID data is used to obtain 0 K bond energies for all dissociation pathways. These energies are converted to obtain

Table 4.7. Conversion of 0 K thresholds to 298 K enthalpies and free energies (kJ/mol)[a]

N	ΔH_0[b]	$\Delta H_{298} - \Delta H_0$[c]	ΔH_{298}	$T\Delta S_{298}$[c]	ΔG_{298}
		$(N_2H_4)_{n-1}H^+$-(N_2H_4)			
2	113.3 (2.7)	2.59 (0.44)	115.1 (2.8)	45.1 (1.2)	70.0 (3.1)
3	72.4 (3.5)	1.24 (0.37)	75.7 (3.0)	45.9 (1.2)	29.7 (3.5)
4	68.3 (4.6)	0.77 (0.33)	68.7 (4.9)	46.5 (1.3)	22.2 (5.6)
		$[(CH_3)_2N_2H_2]_{n-1}H^+$-$(CH_3)_2N_2H_2$			
2	99.4 (2.9)	-0.38 (0.3)	101.3 (4.0)	46.5 (1.3)	54.9 (3.6)

[a] Uncertainties in parentheses. [b] Experimental values from this work (Table 4.4). [c] Values are calculated from the vibrational frequencies and rotational constants at the B3LYP-GD3BJ/6-311+G(d,p) level of theory. Uncertainties are found by scaling the frequencies up and down by 10%.

thermodynamic values at 298 K using a rigid rotor/harmonic oscillator approximation. The TCID BDEs for the $(N_2H_4)_nH^+$ compare favorably to BDEs measured in KERD studies,[11] and decrease with increasing complex size, as expected for increased solvation of the charge center.[13-15] The BDE for the proton-bound dimer of UDMH is measured here for the first time and found to be weaker than the unmethylated dimer. This result is consistent with a previously noted trend that the BDEs of proton-bound homodimers decrease with increasing proton affinity of the monomer.[69] The BDEs calculated at the B3LYP, M06, mPW1PW91, PBE0, MP2(full), and CCSD(T) levels of theory with BSSE and/or ED also align nicely with the experimental values presented here, where the M06 and PBE0 levels of theory without ED reproduce the experimental BDEs the best.

4.6 Supporting Information

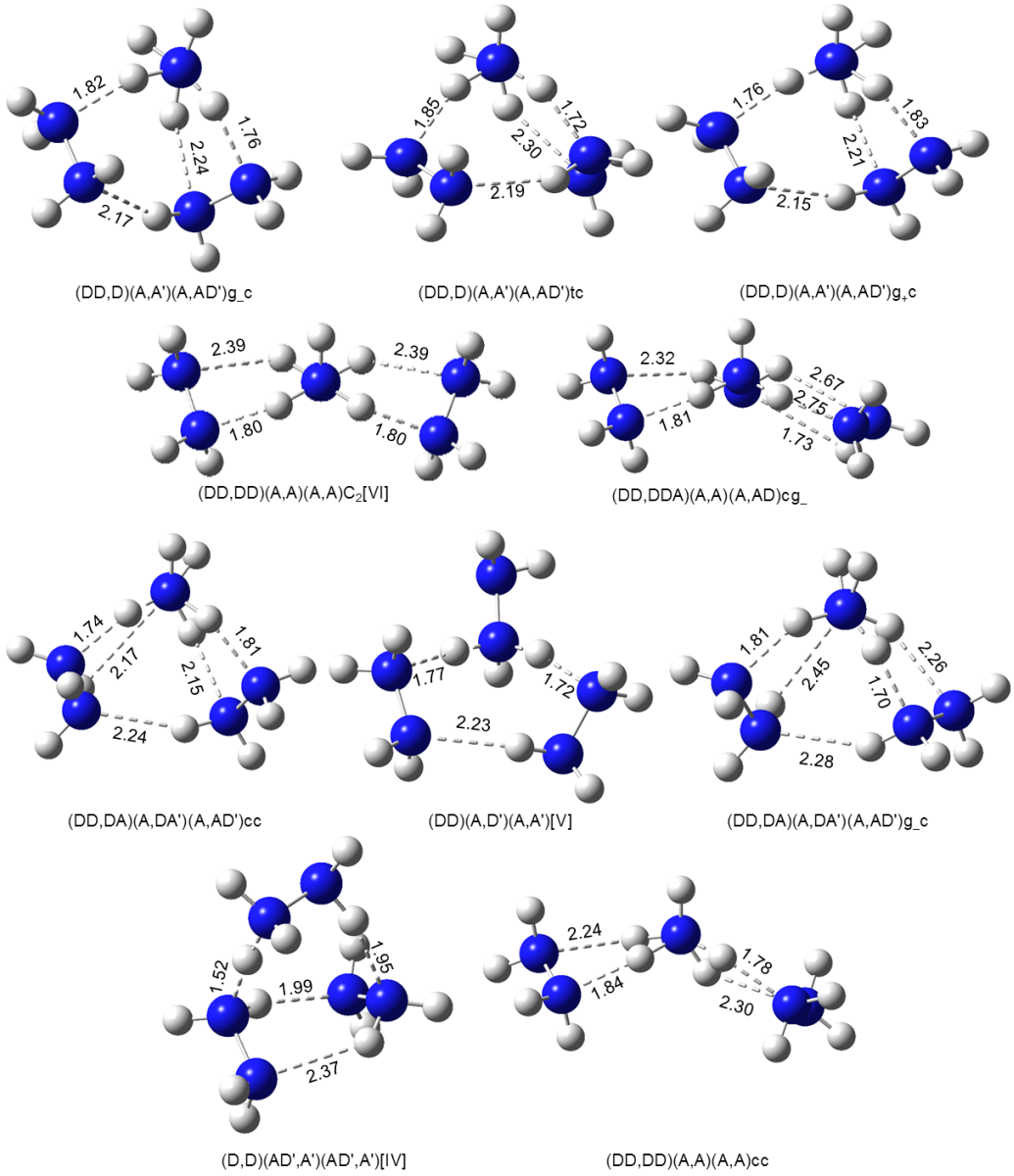

Figure 4.S1. The 10 low-lying isomers of $(N_2H_4)_3H^+$ calculated at the B3LYP-GD3BJ/6-311+G(d,p) level of theory. Hydrogen bonds are indicated by dashed lines with distances indicated in Å. In all cases, the protonated hydrazine is located at the top.

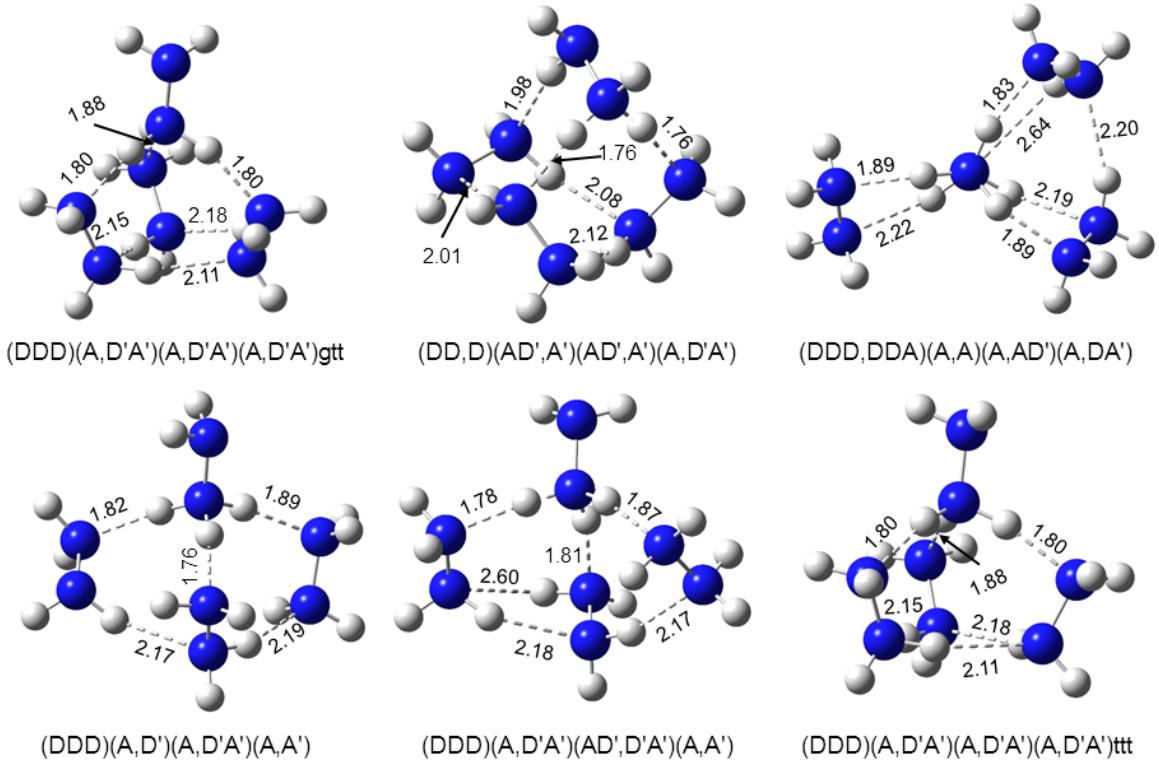

Figure 4.S2. The six low-lying isomers of $(N_2H_4)_4H^+$ calculated at the B3LYP-GD3BJ/6-311+G(d,p) level of theory. Hydrogen bonds are indicated by dashed lines with distances indicated in Å. In all cases, the protonated hydrazine is located at the top.

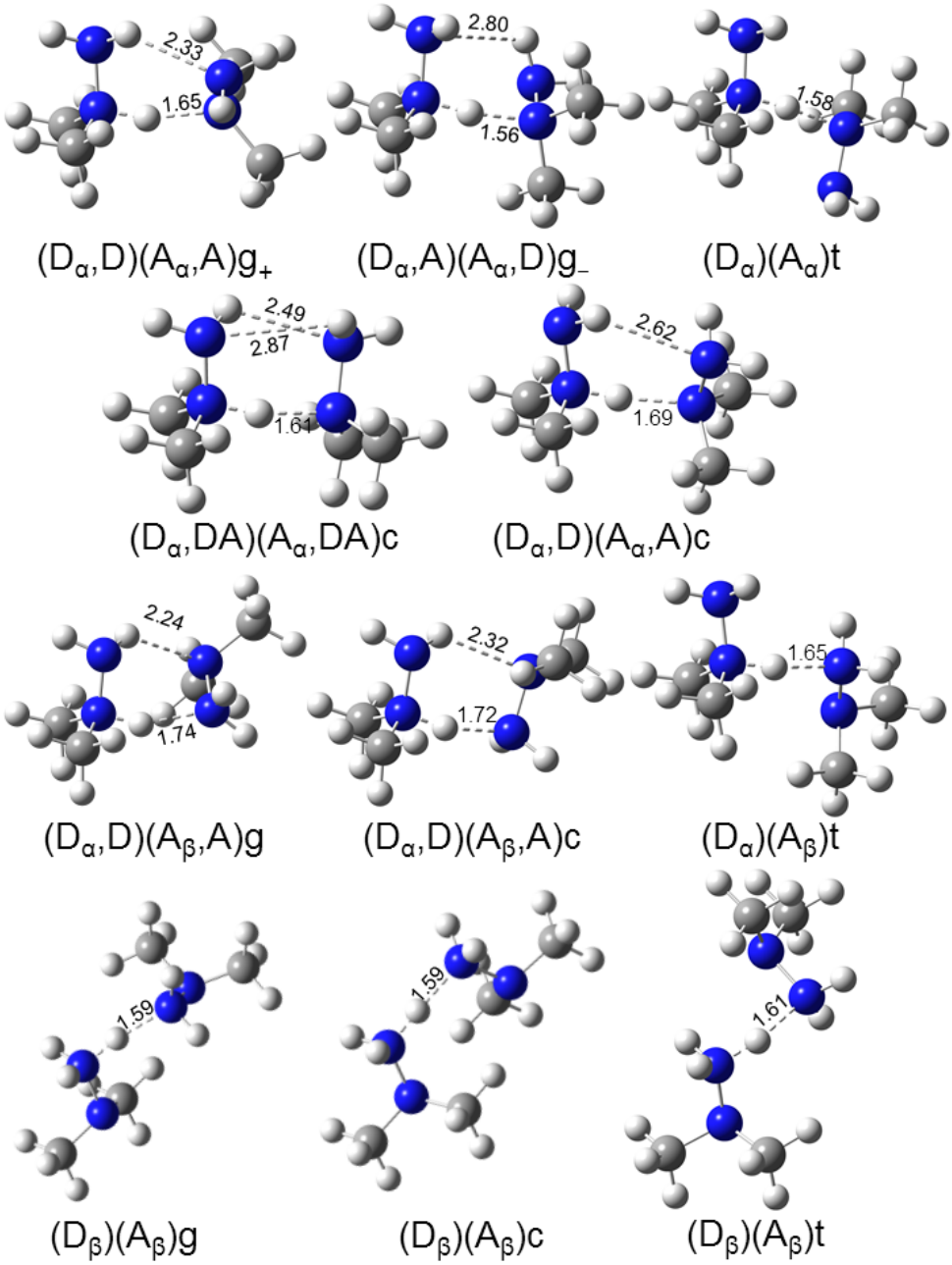

Figure 4.S3. The 11 isomers of $[(CH_3)_2N_2H_2]_2H^+$ calculated at the B3LYP-GD3BJ/6-311+G(d,p) level of theory. Hydrogen bonds are indicated by dashed lines with distances indicated in Å. In all cases, the protonated UDMH is located to the left.

4.7 References

1. Gardner, J. A.; Dressler, R. A.; Salter, R. H.; Murad, E., Reactions of Hydrazine with Atomic Oxygen(1^+) and other Ions at Suprathermal Energies. *J. Phys. Chem.* **1992,** (11), 4210-4217.

2. Matus, M. H.; Arduengo, A. J.; Dixon, D. A., The Heats of Formation of Diazene, Hydrazine, $N_2H_3^+$, $N_2H_5^+$, N_2H, and N_2H_3 and the Methyl Derivatives CH_3NNH, CH_3NNCH_3, and $CH_3HNNHCH_3$. *J. Phys. Chem. A* **2006,** (33), 10116-10121.

3. Lunn, G.; Sansone, E. B.; Keefer, L. K., Notes. Reductive Destruction of Hydrazines as an Approach to Hazard Control. *Environ. Sci. Technol.* **1983,** (4), 240-243.

4. Tuazon, E. C.; Carter, W. P. L.; Winer, A. M.; Pitts, J. N., Reactions of Hydrazines with Ozone under Simulated Atmospheric Conditions. *Environ. Sci. Technol.* **1981,** (7), 823-828.

5. Buck, U.; Gu, X. J.; Hobein, M.; Lauenstein, C., Infrared Photodissociation of Size-selected Hydrazine Clusters. *Chem. Phys. Lett.* **1989,** (4), 455-460.

6. Beu, T. A.; Buck, U.; Siebers, J. G.; Wheatley, R. J., A New Intermolecular Potential for Hydrazine Clusters: Structures and Spectra. *J. Chem. Phys.* **1997,** (17), 6795-6805.

7. Beu, T. A.; Buck, U.; Ettischer, I.; Hobein, M., et al., Vibrational Predissociation Spectra of Size Selected Hydrazine Clusters: Experiment and Calculations. *J. Chem. Phys.* **1997,** (17), 6806-6812.

8. Dyczmons, V., Structures and Vibrations of the Dimers and Trimers of Hydrazine/water. *J. Mol. Struct.* **2006,** (1), 9-13.

9. Dyczmons, V., The Trimer Structures of Hydrazine. *J. Phys. Chem. A* **2002,** (19), 5031-5040.

10. Cabaleiro-Lago, E. M.; Ríos, M. A., Ab Initio Study of Interactions in Hydrazine Clusters of One To Four Molecules: Cooperativity in the Interaction. *J. Phys. Chem. A* **1999,** (32), 6468-6474.

11. Feng, W. Y.; Aviyente, V.; Varnali, T.; Lifshitz, C., Structures, Energetics, and Reactions of Proton-Bound Hydrazine Clusters. *J. Phys. Chem.* **1995,** (6), 1776-1785.

12. Dyczmons, V., Six Structures of the Hydrazine Dimer. *J. Phys. Chem. A* **2000,** (35), 8263-8269.

13. Wei, S.; Tzeng, W. B.; Castleman, A. W., Dissociation Dynamics: Measurements of Decay Fractions of Metastable Ammonia Cluster Ions. *J. Chem. Phys.* **1990,** (4), 2506-2512.

14. A W Castleman, J., and; Wei, S., Cluster Reactions. *Annu. Rev. Phys. Chem.* **1994,** (1), 685-719.

15. A W Castleman, J., and; Keesee, R. G., Clusters: Properties and Formation. *Annu. Rev. Phys. Chem.* **1986,** (1), 525-550.

16. Kim, T.; Tolmachev, A. V.; Harkewicz, R.; Prior, D. C., et al., Design and Implementation of a New Electrodynamic Ion Funnel. *Anal. Chem.* **2000,** (10), 2247-2255.

17. Shaffer, S. A.; Tolmachev, A.; Prior, D. C.; Anderson, G. A., et al., Characterization of an Improved Electrodynamic Ion Funnel Interface for Electrospray Ionization Mass Spectrometry. *Anal. Chem.* **1999**, 2957-2964.

18. Shaffer, S. A.; Prior, D. C.; Anderson, G. A.; Udseth, H. R., et al., An Ion Funnel Interface for Improved Ion Focusing and Sensitivity Using Electrospray Ionization Mass Spectrometry. *Anal. Chem.* **1998**, 4111-4119.

19. Moision, R. M.; Armentrout, P. B., An Electrospray Ionization Source for Thermochemical Investigation with the Guided Ion Beam Mass Spectrometer. *J. Am. Soc. Mass Spectrom.* **2007,** (6), 1124-34.

20. Heaton, A. L.; Ye, S. J.; Armentrout, P. B., Experimental and Theoretical Studies of Sodium Cation Complexes of the Deamidation and Dehydration Products of Asparagine, Glutamine, Aspartic Acid, and Glutamic Acid. *J. Phys. Chem. A* **2008,** (15), 3328-3338.

21. Heaton, A. L.; Moision, R. M.; Armentrout, P. B., Experimental and Theoretical Studies of Sodium Cation Interactions with the Acidic Amino Acids and Their Amide Derivatives. *J. Phys. Chem. A* **2008,** (15), 3319-3327.

22. Cooper, T. E.; Armentrout, P. B., Threshold Collision-induced Dissociation of Hydrated Cadmium (II): Experimental and Theoretical Investigation of the Binding Energies for $Cd^{2+}(H_2O)_n$ Complexes (n = 4 – 11). *Chem. Phys. Lett.* **2010,** (1–3), 1-6.

23. Carl, D. R.; Moision, R. M.; Armentrout, P. B., In-source Fragmentation Technique for the Production of Thermalized Ions. *J. Am. Soc. Mass Spectrom.* **2009,** (12), 2312-2317.

24. Carl, D. R.; Moision, R. M.; Armentrout, P. B., Binding Energies for the Inner Hydration Shells of Ca^{2+}: An Experimental and Theoretical Investigation of $Ca^{2+}(H_2O)_x$ Complexes (x = 5 – 9). *Int. J. Mass Spectrom.* **2007,** (2–3), 308-325.

25. Carl, D. R.; Chatterjee, B. K.; Armentrout, P. B., Threshold Collision-Induced Dissociation of $Sr^{2+}(H_2O)_x$ Complexes (x = 1 – 6): An Experimental and Theoretical Investigation of the Complete Inner Shell Hydration Energies of Sr^{2+}. *J. Chem. Phys.* **2010**, 044303-1-12.

26. Ervin, K. M.; Armentrout, P. B., Translational Energy Dependence of $Ar^+ + XY \rightarrow ArX^+ + Y$ ($XY = H_2, D_2, HD$) from Thermal to 30 eV c.m. *J. Chem. Phys.* **1985,** (1), 166-189.

27. Teloy, E.; Gerlich, D., Integral Cross Sections for Ion—molecule Reactions. I. The Guided Beam Technique. *Chem. Phys.* **1974,** (3), 417-427.

28. Dalleska, N. F.; Honma, K.; Sunderlin, L. S.; Armentrout, P. B., Solvation of Transition Metal Ions by Water. Sequential Binding Energies of M+(H2O)x (x = 1-4) for M = Ti to Cu Determined by Collision-Induced Dissociation. *J. Am. Chem. Soc.* **1994,** (8), 3519-3528.

29. Aristov, N.; Armentrout, P. B., Collision-Induced Dissociation of Vanadium Monoxide Ion. *J. Phys. Chem.* **1986**, 5135-5140.

30. Daly, N. R., Scintillation Type Mass Spectrometer Ion Detector. *Rev. Sci. Instrum.* **1960**, 264-267.

31. Hales, D. A.; Lian, L.; Armentrout, P. B., Collision-Induced Dissociation of Nb_n^+ (n = 2 - 11): Bond Energies and Dissociation Pathways. *Int. J. Mass Spectrom. Ion Processes* **1990**, 269-301.

32. Muntean, F.; Armentrout, P. B., Guided Ion Beam Study of Collision-Induced Dissociation Dynamics: Integral and Differental Cross Sections. *J. Chem. Phys.* **2001**, 1213-1228.

33. Stein, S. E.; Rabinovitch, B. S., On the Use of Exact State Counting Methods in RRKM Rate Calculations. *Chem. Phys. Lett.* **1977,** (1), 183-188.

34. Stein, S. E.; Rabinovitch, B. S., Accurate Evaluation of Internal Energy Level Sums and Densities Including Anharmonic Oscillators and Hindered Rotors. *J. Chem. Phys.* **1973,** (6), 2438-2445.

35. Beyer, T.; Swinehart, D. F., Algorithm 448: Number of Multiply-restricted Partitions. *Comm. ACM* **1973,** (6), 379.

36. Truhlar, D. G.; Garrett, B. C.; Klippenstein, S. J., Current Status of Transition-State Theory. *J. Phys. Chem.* **1996**, 12771-12800.

37. Holbrook, K. A.; Pilling, M. J.; Robertson, S. H., *Unimolecular Reactions*. 2nd ed.; Wiley: New York, 1996.

38. Gilbert, R. G.; Smith, S. C., *Theory of Unimolecular and Recombination Reactions*. Blackwell Scientific: London, 1990.

39. Armentrout, P. B.; Simons, J., Understanding Heterolytic Bond Cleavage. *J. Am. Chem. Soc.* **1992,** (22), 8627-8633.

40. Rodgers, M. T.; Ervin, K. M.; Armentrout, P. B., Statistical Modeling of Collision-induced Dissociation Thresholds. *J. Chem. Phys.* **1997,** (11), 4499-4508.

41. Armentrout, P. B., Statistical Modeling of Sequential Collision-induced Dissociation Thresholds. *J. Chem. Phys.* **2007,** (23), 234302.

42. Pettersen, E. F.; Goddard, T. D.; Huang, C. C.; Couch, G. S., et al. *UCSF Chimera - A Visualization System for Exploratory Research and Analysis."*, 2004.

43. Case, D. A.; Babin, V.; Berryman, J. T.; Betz, R. M., et al. *AMBER 14*, University of California, San Francisco, 2014.

44. Valiev, M.; Bylaska, E. J.; Govind, N.; Kowalski, K., et al., NWChem: A Comprehensive and Scalable Open-source Solution for Large Scale Molecular Simulations. *Comput. Phys. Commun.* **2010,** (9), 1477-1489.

45. Frisch, M. J.; Trucks, G. W.; Schlegel, H. B.; Scuseria, G. E., et al. *Gaussian 09, Revision D.01* Gaussian, Inc.: Wallingford, CT, USA, 2009.

46. Becke, A. D., Density-functional Thermochemistry. III. The Role of Exact Exchange. *J. Chem. Phys.* **1993,** (7), 5648.

47. Ditchfield, R.; Hehre, W. J.; Pople, J. A., Self-Consistent Molecular-Orbital Methods. IX. An Extended Gaussian-Type Basis for Molecular-Orbital Studies of Organic Molecules. *J. Chem. Phys.* **1971,** (2), 724-728.

48. Grimme, S.; Ehrlich, S.; Goerigk, L., Effect of the Damping Function in Dispersion Corrected Density Functional Theory. *J. Comput. Chem.* **2011,** (7), 1456-1465.

49. Grimme, S.; Antony, J.; Ehrlich, S.; Krieg, H., A Consistent and Accurate *ab initio* Parametrization of Density Functional Dispersion Correction (DFT-D) for the 94 Elements H-Pu. *J. Chem. Phys.* **2010,** (15), 154104-1-19.

50. Zhao, Y.; Truhlar, D. G., The M06 Suite of Density Functionals for Main Group Thermochemistry, Thermochemical Kinetics, Noncovalent Interactions, Excited States, and Transition Elements: Two New Functionals and Systematic Testing of Four M06-Class Functionals and 12 Other Functionals. *Theor. Chem. Acc.* **2008**, 215-241.

51. Perdew, J. P.; Burke, K.; Ernzerhof, M., Generalized Gradient Approximation Made Simple *Phys. Rev. Lett.* **1997,** (7), 1396-1396.

52. Adamo, C.; Barone, V., Toward Reliable Density Functional Methods without Adjustable Parameters: The PBE0 Model. *J. Chem. Phys.* **1999,** (13), 6158-6170.

53. Adamo, C.; Barone, V., Toward Reliable Adiabatic Connection Models Free from Adjustable Parameters. *Chem. Phys. Lett.* **1997,** (1–3), 242-250.

54. Adamo, C.; Barone, V., Exchange Functionals with Improved Long-range Behavior and Adiabatic Connection Methods without Adjustable Parameters: The mPW and mPW1PW Models. *J. Chem. Phys.* **1998,** (2), 664-675.

55. Becke, A. D., Density-functional Thermochemistry. IV. A New Dynamical Correlation Functional and Implications for Exact-exchange Mixing. *J. Chem. Phys.* **1996,** (3), 1040-1046.

56. Møller, C.; Plesset, M. S., Note on an Approximation Treatment for Many-Electron Systems. *Physical Review* **1934,** (7), 618-622.

57. Frisch, M. J.; Head-Gordon, M.; Pople, J. A., A Direct MP2 Gradient Method. *Chem. Phys. Lett.* **1990,** (3), 275-280.

58. Frisch, M. J.; Head-Gordon, M.; Pople, J. A., Semi-direct Algorithms for the MP2 Energy and Gradient. *Chem. Phys. Lett.* **1990,** (3), 281-289.

59. Head-Gordon, M.; Head-Gordon, T., Analytic MP2 Frequencies without Fifth-order Storage. Theory and Application to Bifurcated Hydrogen Bonds in the Water Hexamer. *Chem. Phys. Lett.* **1994,** (1 – 2), 122-128.

60. Head-Gordon, M.; Pople, J. A.; Frisch, M. J., MP2 Energy Evaluation by Direct Methods. *Chem. Phys. Lett.* **1988,** (6), 503-506.

61. Cizek, J., *Advances in Chemical Physics*. Wiley Interscience: New York, 1969; Vol. 14, p 35.

62. Purvis III, G. D.; Bartlett, R. J., A Full Coupled-cluster Single and Doubles Model - The Inclusion of Disconnected Triples. *J. Chem. Phys.* **1982**, 1910-1918.

63. Scuseria, G. E.; Janssen, C. L.; Schaefer III, H. F., An Efficient Reformulation of the Colosed-shell Coupled Cluster Single and Double Excitation (CCSD) Equations. *J. Chem. Phys.* **1988**, 7382-7387.

64. Scuseria, G. E.; Schaefer III, H. F., Is Coupled Cluster Singles and Doubles (CCSD) More Computationally Intensive than Quadratic Configuration-interaction (QCISD)? *J. Chem. Phys.* **1989**, 3700-3703.

65. Pople, J. A.; Head-Gordon, M.; Raghavachari, K., Quadratic Configuration Interaction - A General Technique for Determining Electron Correlation Energies. *J. Chem. Phys.* **1987**, 5968-5975.

66. van Duijneveldt, F. B.; van Duijneveldt-van de Rijdt, J. G. C. M.; van Lenthe, J. H., State of the Art in Counterpoise Theory. *Chem. Rev.* **1994**, 1873-1885.

67. Boys, S. F.; Bernardi, R., The Calculation of Small Molecular Interactions by the Differences of Separate Total Energies. Some Procedures with Reduced Errors. *Mol. Phys.* **1970**, 553-566.

68. Hunter, E. P. L.; Lias, S. G., Evaluated Gas Phase Basicities and Proton Affinities of Molecules: An Update. *J. Phys. Chem. Ref. Data* **1998,** (3), 413-656.

69. Meot-Ner, M., Update 1 of: Strong Ionic Hydrogen Bonds. *Chem. Rev.* **2012,** (10), PR22-PR103.

70. Donald, K. J.; Tawfik, M.; Buncher, B., Weak Interactions as Diagnostic Tools for Inductive Effects. *J. Phys. Chem. A* **2015,** (16), 3780-3788.

71. Chattaraj, P. K.; González-Rivas, N.; Matus, M. H.; Galván, M., Substituent Effects. *J. Phys. Chem. A* **2005,** (25), 5602-5607.

72. Smith, A. P.; McKercher, A. E.; Mawhinney, R. C., Inductive Effect: A Quantum Theory of Atoms in Molecules Perspective. *J. Phys. Chem. A* **2011,** (45), 12544-12554.

73. Tang, I. N.; Castleman, A. W., Gas-phase Solvation of the Ammonium Ion in Ammonia. *J. Chem. Phys.* **1975,** (11), 4576-4578.

74. Payzant, J. D.; Cunningham, A. J.; Kebarle, P., Gas Phase Solvation of the Ammonium Ion by NH_3 and H_2O and Stabilities of Mixed Clusters $NH_4^+(NH_3)_n(H_2O)_w$. *Can. J. Chem.* **1973,** (19), 3242-3249.

75. Deakyne, C. A.; Knuth, D. M.; Speller, C. V.; Meot-Ner (Mautner), M., et al., Filling of Solvent Shells about Ions. Part 3. Isomeric Clusters of $(HCN)_n(NH_3)_mH^+$. *J. Mol. Struct.* **1994**, 217.

76. Meot-Ner, M.; Sieck, L. W., Proton Affinity Ladders from Variable-temperature Equilibrium Measurements. 1. A Reevaluation of the Upper Proton Affinity Range. *J. Am. Chem. Soc.* **1991,** (12), 4448-4460.

77. El-Shall, M. S.; Daly, G. M.; Gao, J.; Meot-Ner, M., et al., How Sensitive are Cluster Compositions to Energetics? A Joint Beam Expansion/thermochemical Study of Water-methanol-trimethylamine Clusters. *J. Phys. Chem.* **1992,** (2), 507-510.

78. Yamdagni, R.; Kebarle, P., Gas-phase Basicities of Amines. Hydrogen Bonding in Proton-bound Amine Dimers and Proton-induced Cyclization Of .Alpha., .Omega.-diamines. *J. Am. Chem. Soc.* **1973,** (11), 3504-3510.

79. Meot-Ner, M., Intermolecular Forces in Organic Clusters. *J. Am. Chem. Soc.* **1992,** (9), 3312-3322.

80. Wei, S.; Tzeng, W. B.; Castleman, A. W., Structure of Protonated Solvation Complexes: Ammonia-trimethylamine Cluster Ions and Their Metastable Decompositions. *J. Phys. Chem.* **1991,** (2), 585-591.

CHAPTER 5

THRESHOLD COLLISION-INDUCED DISSOCIATION OF PROTONATED HYDRAZINE AND DIMETHYLHYDRAZINE CLUSTERED WITH WATER

5.1 Abstract

Threshold collision-induced dissociation using a guided ion beam tandem mass spectrometer is performed on $(N_2H_4)H^+(H_2O)_n$, where n = 1 and 2, and on the protonated unsymmetrical 1, 1-dimethylhydrazine one-water complex. The primary dissociation pathway for all clusters is a loss of a single water molecule, which for n = 2 is followed by the sequential loss of an additional water molecule at higher collision energies. The data are analyzed using a statistical model after accounting for internal and kinetic energy distributions, multiple collisions, and kinetic shifts to obtain 0 K bond dissociation energies (BDEs). These are also converted using a rigid rotor/harmonic oscillator approximation to yield thermodynamic values at room temperature. Experimental BDEs compare favorably to theoretical BDEs determined at the B3LYP, M06, mPW1PW91, PBE0, MP2(full), and CCSD(T) levels of theory with a 6-311+G(2d,2p) basis set both with and without empirical dispersion. These calculations also allow visualization of the structures of these complexes, which are simple hydrogen-bonded donor-acceptors.

Reprinted from C. P. McNary, and P. B. Armentrout, J. Chem. Phys. 145, 214311 (2016).
With permission from AIP Publishing.

5.2. Introduction

Hydrazine and unsymmetrical 1,1-dimethylhydrazine (commonly known as UDMH) are used as fuels for some types of rocket engines,[1] have been suggested as possible chemical hydrogen storage systems,[2] and their hydrates are extensively investigated in synthetic organic chemistry.[3] During successful and unsuccessful rocket burns, these fuels are released into the atmosphere, where they react with atmospheric gases leading to devastating effects on the environment.[4,5] In addition, protonated hydrazine, $(N_2H_4)H^+$, is known to be formed in ion/molecule reactions that occur in the ionosphere or during launch and reentry[1] and upon ionization of neutral clusters of hydrazine in water.[6] Therefore, it is of interest to explore the fundamental properties of the ionic water clusters of hydrazine and UDMH in order to understand what impact these systems might have on the environment.

Hydrazine has six hydrogen-bonding sites, four NH donors and two nitrogen lone pair acceptors, and its neutral water clusters tend to form cyclic configurations,[3] whereas protonated hydrazine water clusters have yet to be explored. Likewise, the structures, energetics, and dynamics of protonated UDMH water complexes are unexplored to the best of our knowledge.

Dyczmons[3] theoretically investigated the structures of neutral hydrazine water clusters, (N2H4)(H2O)*n*, where *n* = 1 and 2, locating one and five isomers, respectively. For *n* = 2, the lowest-lying isomer prefers a cyclic configuration, which was proposed to be a result of cooperative interactions that enhance the local dipole moments leading to a more effective hydrogen bonding.

Lifshitz and co-workers[7] used mass-analyzed ion kinetic energy spectrometry and

collision-induced dissociation (CID) to examine the metastable fragmentations of $(N_2H_4)_nH^+$, where n = 2–7. During that experiment, Lifshitz and co-workers also observed proton-bound hydrazine water clusters, $(N_2H_4)H^+(H_2O)_n$, where n = 1–4, which formed readily in their source. Upon CID, the $(N_2H_4)H^+(H_2O)_n$ clusters would lose a single water molecule initially and then sequential losses of additional water molecules with increasing translational energy. No detailed characterization of the structures, energetics, or dynamics of these proton-bound hydrazine water clusters was obtained.

In the current study, we use threshold collision-induced dissociation (TCID) in a guided ion beam tandem mass spectrometer (GIBMS) to quantitatively investigate the thermochemistry of the $(N_2H_4)H^+(H_2O)_n$ systems for n = 1 and 2 and the protonated UDMH water complex. Analysis of kinetic energy dependent TCID cross sections yields 0 K bond dissociation energies (BDEs) for these complexes. These BDEs are then compared to theoretical values from six different levels of theory, which are also used to thoroughly explore the possible structures of these clusters. The present work complements a similar study on the thermodynamic and structural properties of clusters of protonated hydrazine and protonated UDMH.[8]

5.3 Experimental and Theoretical Methods

5.3.1 Instrumentation

Complexes of the protonated hydrazine and UDMH with water are created from a 0.1M solution of hydrazine or UDMH in high-performance liquid chromatography (HPLC) grade water using electrospray ionization (ESI) techniques. The solution is advanced at a rate of 100–300 µl/h through a 35 gauge 304 stainless steel needle that has

an applied voltage of 2.5 kV. Once in the gas phase, ions enter the vacuum system through a stainless steel inlet cap with an inlet diameter of 0.010" followed by a 6.125" long by 0.040" diameter electro-formed nickel capillary that is heated to a temperature of 120 ºC in order to desolvate large droplets. An 88 plate radio frequency (rf) ion funnel (IF) with superimposed DC gradient field, copied from a design described in detail elsewhere,[9] collects and focuses the ions to increase signal intensity.[10,11] The voltage bias between the first and last plate of the ion funnel is kept below 20 V to minimize heating of the ions. At the end of the funnel, the ions enter an rf-only hexapole with rf amplitudes typically set at 250 V peak to peak centered around ground. Here, the ions undergo cooling by $>10^5$ thermalizing collisions with ambient gas (largely air and water).[12] This ensures that ions beyond the hexapole are well-defined by a Maxwell–Boltzmann distribution of rovibrational states at room temperature, as demonstrated elsewhere.[12-17]

Ions generated in the ESI/IF/hexapole source then enter the guided ion beam tandem mass spectrometer,[18,19] where they are focused into a magnetic momentum analyzer for initial mass selection. These reactant ions are decelerated to a well-defined kinetic energy and injected into a rf octopole ion guide[20] where they pass through a collision cell containing Ar at low pressures. Although xenon is commonly used in our laboratory, for reasons described elsewhere,[21,22] argon is used in the present experiment because preliminary results with xenon showed a significant amount of back scattered reactant ions at low collision energy. As will be seen below, for these weakly bound systems, the use of Ar still permits good collision energy transfer such that accurate threshold energies can be obtained. Product and remaining reactant ions are extracted from the octopole, mass selected using a quadrupole mass filter, and detected using a

Daly detector.[23]

5.3.2 Data Analysis

Acquiring accurate thermodynamic information from the TCID data requires diligent consideration of many experimental factors that convolute the raw data. These factors include the internal and kinetic energy distributions of the ionic and neutral reactants, lifetime effects that arise from a finite experimental time window, and the probability of multiple collisions. The measured intensities of the reactant and product ions are first corrected for dissociation outside the collision cell as well as background noise by measuring their intensities with and without gas in the collision cell. They are then converted to absolute reaction cross sections using a Beer–Lambert analogue, as described elsewhere.[18] The energy of the reactants is converted from the lab frame voltage of the ion, V_{lab}, to the center-of-mass energy, E_{CM}, using $E_{CM} = V_{lab}m/(m + M)$, where m is the mass of the reactant neutral and M is the mass of the reactant ion. The kinetic energy distribution of the ions is determined using a retarding potential analysis,[18] which also allows the absolute zero of the energy to be obtained. Experiments are performed at three different pressures of the Ar neutral gas, typically ~0.1, 0.2, and 0.4 mTorr. The cross sections at each pressure are used to linearly extrapolate to a zero pressure cross section which rigorously represents a single collision event.[24]

The kinetic energy dependent CID cross sections are modeled using the empirical model shown as follows:

$$\sigma(E) = \sigma_0 \sum_i g_i(E + E_i - E_0)^N/E, \quad (5.1)$$

where σ_0 is an energy independent scaling factor, E is the relative collision energy, E_0 is

the reaction threshold at 0 K, *N* describes the energy deposition function,[19] and the summation is over the rovibrational states of the reactant ion (before collision) having energies E_i and populations g_i, where $\Sigma g_i = 1$. Rovibrational states taken from quantum chemical calculations of the ground state structures are directly counted using the Beyer–Swinehart–Stein–Rabinovitch algorithm[25-27] and are assigned populations on the basis of a Maxwell–Boltzmann distribution at 300 K. As the size of the reactants increases, the number of accessible rovibrational states increases such that dissociative lifetimes near the threshold energy can be longer than the experimental time-of-flight, $\tau \sim 5 \times 10^{-4}$ s.[19] For this reason, the apparent dissociation thresholds for larger reaction complexes shift to higher energies. This kinetic shift is accounted for using Rice-Ramsperger-Kassel-Marcus (RRKM) statistical theory[28-30] for unimolecular dissociation and is incorporated into the cross section model as follows:

$$\sigma(E) = \left(\frac{N\sigma_0}{E}\right) \sum_i g_i \int_{E_0 - E_i}^{E} (E - \varepsilon)^{N-1} P_{D1} d\varepsilon, \tag{5.2}$$

where ε is the energy that is deposited into internal modes of the reactant ion complex during collision, such that the energy available to the energized molecule is $E^* = E_i + \varepsilon$, and $P_{D1} = 1 - \exp(-k(E^*)\tau)$ is the dissociation probability. If the dissociative lifetime of the energized molecule is shorter than the average experimental time frame, the integration in Eq. (5.2) recovers Eq. (5.1). The rate coefficient, $k(E^*)$, is defined by RRKM theory as follows:

$$k(E^*) = \frac{dN^\dagger(E^* - E_0)}{h\rho(E^*)}, \tag{5.3}$$

where the reaction degeneracy, *d*, is calculated from the ratio of the rotational symmetry numbers of reactants and products, $N^\dagger(E^* - E_0)$ is the sum of rovibrational states of the transition state (TS), and $\rho(E^*)$ is the density of states of the energized molecule at E^*. In

the present work, the dissociation channels observed are heterolytic bond cleavages that can be characterized as proceeding over loose TSs equivalent to the product asymptotes.[31] Thus, the TSs are treated at the phase space limit (PSL) in which the transitional modes are rotors.[32] All molecular parameters for the TS and energized molecule are taken from quantum chemical calculations described below.

Cross sections for the loss of an additional water ligand are modeled by multiplying Eq. (5.2), which reproduces the cross section of the primary dissociation product, by the probability for further dissociation[33] given as follows:

$$P_{D2} = 1 - e^{-k_2(E_2^*)\tau}, \tag{5.4}$$

where $E_2^* = E^* - E_0 - T_1 - E_L$ is the internal energy of the product ion undergoing further dissociation and k_2 is defined analogously to Eq. (5.3) where the TS corresponds to the second dissociation starting at $E_{0,2}$. Statistical assumptions are used to assign the distributions for T_1 and E_L, which represent the translational energy of the primary products and the internal energy of the neutral product, respectively.

For both primary and secondary processes, the model cross sections of Eq. (5.2) and Eqs. (5.2) × (5.4) are convoluted over the kinetic energy distributions of the neutral and ion reactants before comparison to experimental data.[18] The fitting parameters in these equations ($\sigma_0, N, E_0,$ and $E_{0,2}$) are then optimized using a nonlinear least-squares criterion to reproduce the experimental data throughout the threshold region. The threshold energies obtained are equivalent to the 0 K binding energy of water to the protonated hydrazine or UDMH. The uncertainties in these binding energies are determined from the range of parameters obtained from modeling multiple data sets, scaling the vibrational frequencies of reactants and products by ±10%, varying the best fit

N value by ±0.1, changing the experimental time-of-flight up and down by a factor of 2, and including the uncertainty in the energy scale, ±0.05 eV (lab).

5.3.3 Computational Details

To obtain stable geometries, vibrational frequencies, and energies for the protonated hydrazine water clusters and the protonated UDMH one-water complex, theoretical calculations were performed using UCSF Chimera,[34] AMBER,[35] NWChem,[36] and Gaussian 09 Rev. D[37] suites of programs. Possible low-energy conformations of these complexes were explored via a 5000 cycle simulated annealing procedure employing the Amber14SB force field with the in vacuum option. Briefly, a three-phase molecular dynamic distance-restrained simulated annealing process was used with each cycle beginning and ending at 100 K. Each cycle lasted for 1.25 ps and achieved a maximum simulation temperature of 1600 K. Heating and cooling times for each cycle were 0.85 ps each, allowing 0.4 ps for the ions to sample conformational space at the simulation temperature. The conformations accessed at the end of each annealing cycle were subjected to a geometry optimization, by using molecular mechanics minimization every 0.001 ps followed by a quantum mechanic optimization at the HF/6-31G level of theory. Conformations above a relative energy of ~120 kJ/mol were not included in further calculations. Further optimizations of the low-energy conformations were then performed at the B3LYP/6-31G(d) level of theory[38,39] utilizing the opt = loose criterion (maximum step size of 0.01 au and an RMS force of 0.0017 au).[37] Final geometry optimizations and vibrational calculations were performed at the B3LYP/6-311+G(d,p) level of theory with and without empirical dispersion. Frequencies were scaled by 0.989

to obtain zero-point energy (ZPE) and thermal corrections to 298 K. The empirical dispersion functions were set to the D3 version of Grimme dispersion[40] (GD3) with Becke–Johnson (BJ) damping for B3LYP and PBE1PBE (PBE0), and GD3[41] for the M06 levels of theory. Using empirical dispersion optimized structures at the B3LYP/6-311+G(d,p) level of theory, single-point energy calculations were performed with a 6-311+G(2d,2p) basis set at the B3LYP, M06,[42] PBE0,[43,44] mPW1PW91,[45-47] MP2(full) (where full indicates correlation of all electrons),[48-52] and CCSD(T) levels. Results with and without empirical dispersion and with and without basis set superposition error (BSSE) corrections determined at the full counterpoise level[53,54] were also obtained.

These various levels of theory were chosen for the following reasons. B3LYP and MP2(full) levels of theory were used for consistency with previous studies of noncovalent interactions.[13-17,55] The M06[42] and mPW1WP91[46] functionals were included because they are designed to accurately model noncovalent interactions, such as hydrogen bonds, and PBE0 has a similar HF exchange, 25%,[44] to that of the M06 (27%), allowing an assessment of whether this property leads to consistent results. The CCSD(T) level of theory was included to provide a theoretical benchmark for accuracy. Finally, dispersion corrections were utilized when available as these also are designed to improve the description of longer range interactions such as hydrogen bonding.

5.4 Results and Discussion

5.4.1 Theoretical Structures: $(N_2H_4)H^+(H_2O)$

Two low-lying isomers for the protonated hydrazine one-water complex were found and are shown in Figure 5.1, with energies in Table 5.1. In both cases, the

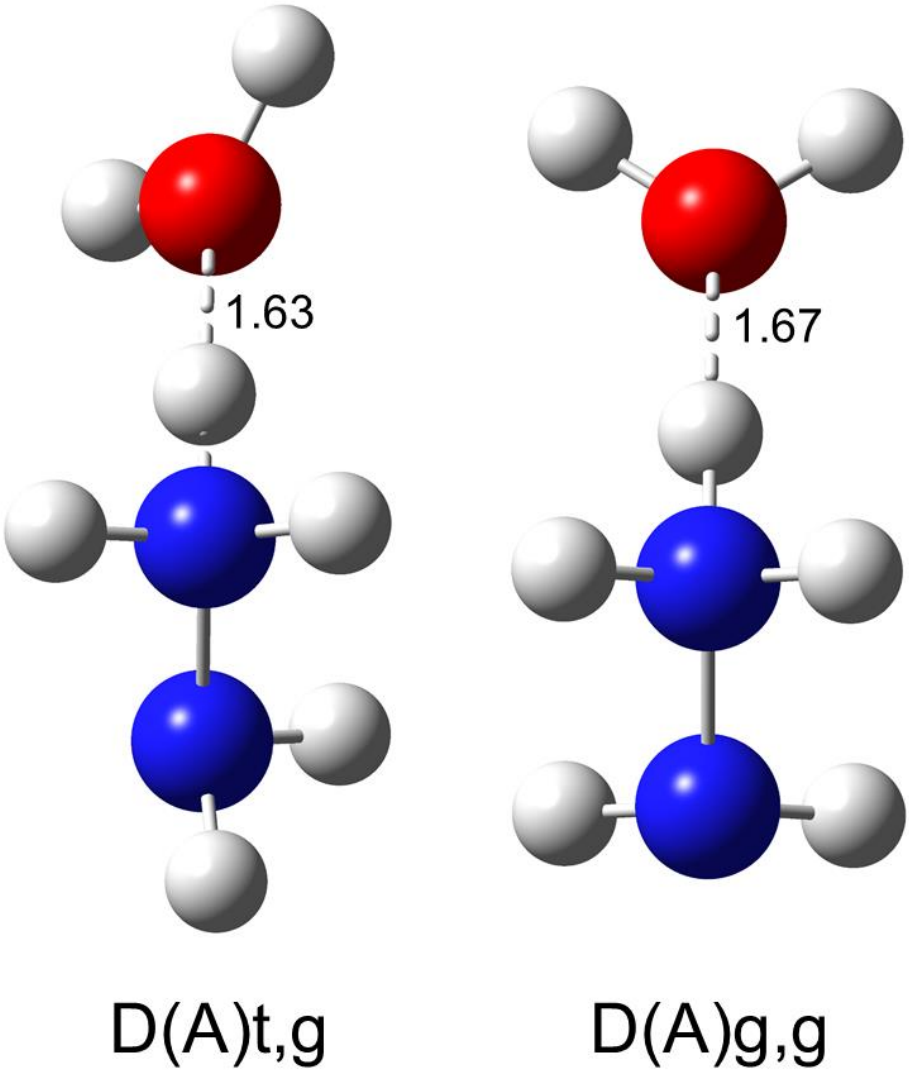

Figure 5.1. The two isomers of $(N_2H_4)H^+(H_2O)$ calculated at the B3LYP-GD3BJ/6-311+G(d,p) level of theory. Hydrogen bonds are indicated by dashed lines with distances indicated in Å.

Table 5.1. Relative energies at 0 K and free energies at 298 K (kJ/mol) of low-lying isomers for protonated hydrazine and UDMH complexed with water[a]

Structure	B3LYP	M06	mPW1PW91	PBE0	MP2(Full)
$(N_2H_4)H^+(H_2O)$					
D(A)t,g	**0.0 (0.0)**	**0.0 (0.0)**	**0.0 (0.0)**	**0.0 (0.0)**	**0.0 (0.0)**
D(A)g,g	3.7 (0.6)	4.2 (1.0)	3.9 (0.6)	4.0 (0.9)	3.6 (0.5)
TS (tg),g	5.9 (6.4)	5.1 (5.6)	6.4 (6.9)	6.3 (9.7)	6.7 (7.2)
$(N_2H_4)H^+(H_2O)_2$					
DD(A)(A)g,g	**0.0 (0.0)**	**0.0 (0.0)**	**0.0 (0.0)**	**0.0 (0.0)**	**0.0 (0.0)**
DD(A)(A)t,g	2.1 (0.7)	1.7 (0.4)	2.1 (0.8)	2.2 (0.8)	2.1 (0.8)
TS (gt),g	7.3 (9.3)	6.2 (8.1)	8.0 (10.0)	7.7 (9.7)	8.1 (10.0)
D(AD')(A')t,g_-	10.7 (11.8)	14.1 (14.2)	10.4 (10.5)	10.9 (10.9)	14.2 (14.2)
D(AD')(A')t,g_+	11.5 (12.0)	14.1 (14.5)	10.0 (10.5)	10.6 (11.1)	13.9 (14.4)
D,D(AD')(AA')t,c	11.3 (17.4)	10.7 (16.8)	13.9 (20.0)	11.3 (17.4)	12.9 (19.0)
D(AD')(A')g,g	15.5 (12.8)	17.9 (15.2)	15.0 (12.2)	15.2 (12.4)	17.2 (14.5)
D,D(AD')(AA')g,c	15.2 (20.2)	14.2 (19.3)	18.1 (23.1)	15.6 (20.6)	16.3 (21.3)
$(CH_3)_2NH^+NH_2(H_2O)$					
D_α(A)g,g	1.7 **(0.0)**	1.4 **(0.0)**	1.5 **(0.0)**	1.7 **(0.0)**	0.2 **(0.0)**
D_α(A)t,g	**0.0** (0.7)	**0.0** (0.6)	**0.0** (0.5)	**0.0** (0.2)	**0.0** (1.7)
TS (gt),g	7.2 (8.3)	6.4 (7.7)	7.5 (8.8)	7.6 (8.6)	7.9 (10.4)
D_β(A)t,g	24.7 (25.6)	19.1 (20.2)	21.7 (22.7)	22.0 (22.8)	30.3 (32.6)
D_β(A)g,g	29.9 (27.6)	23.4 (21.4)	27.4 (25.3)	27.5 (25.2)	35.3 (34.6)
$(CH_3)_2NH^+NH_2$					
D_αg,g	**0.0 (0.0)**	**0.0 (0.0)**	**0.0 (0.0)**	**0.0 (0.0)**	**0.0 (0.0)**
D_αt,g	1.3 (1.2)	2.1 (1.9)	1.5 (1.4)	1.5 (1.4)	2.9 (2.7)
D_β	28.9 (28.7)	26.3 (26.1)	26.8 (26.6)	26.6 (26.4)	35.1 (34.9)

[a] Free energies in parenthesis. Ground structure in bold. All values calculated at the level of theory indicated with empirical dispersion included for B3LYP, M06, and PBE0 levels of theory the 6-311+G(2d,2p) basis set with structures, zero-point energies, and thermal energies calculated at B3LYP-GD3BJ/6-311+G(d,p) level of theory.

protonated nitrogen donates a hydrogen bond to the water acceptor, such that we use a D(A) nomenclature to identify these species. The two isomers only differ from one another in the dihedral angles of the water with respect to the hydrogen atoms on the unprotonated nitrogen. These dihedral angles are designated as either gauche (g, near 60º) or *trans* (t, near 180º). All five levels of theory suggest that the D(A)t,g isomer is the ground structure (GS), whereas the D(A)g,g isomer is 3.6–4.2 and 0.5–1.0 kJ/mol higher in energy at 0 and 298 K, respectively. Because the relative energies of these two isomers at 298 K are small, a Maxwell-Boltzmann population at 298 K for the D(A)t,g and D(A)g,g isomers are 55%–60% and 40%–45%, respectively. Thus, it seems likely that both isomers are populated at room temperature. We also explored the transition state between these isomers, finding that it lies 5.6–9.7 kJ/mol higher than the GS. Thus, there is a small probability of isomerization occurring at 298 K, although this would not perturb the equilibrium populations. We also looked for structures in which the water is bound to the unprotonated nitrogen but these always collapsed to the structures of Figure 5.1. Neither of the two isomers located here resembles the neutral hydrazine one-water complex found by Dyczmons,[3] which has a D,A(AD) structure such that the water donates one its hydrogens to the lone pair of electrons on one nitrogen and accepts a hydrogen from the other NH_2 of hydrazine. This difference is simplistically accounted for by the fact that the protonated nitrogen can only donate a hydrogen, whereas prior to protonation, this nitrogen can either donate or accept a hydrogen bond.

5.4.2 Theoretical Structures: $(N_2H_4)H^+(H_2O)_2$

For the n = 2 protonated hydrazine water complex, we again use a donor (D)/acceptor (A) nomenclature coupled with the dihedral angles associated with the water binding site and the hydrogens on the unprotonated nitrogen. Here, the dihedral angles are *cis* (c, for angles between 0–45°), *trans*, or gauche with + or – when needed to distinguish similar isomers. In addition, interactions between water molecules are indicated by a prime symbol (′). The two low-lying, DD(A)(A)g,g and DD(A)(A)t,g, and five higher energy isomers were located and are shown in Figure 5.2, with energies in Table 5.1.

All five levels of theory suggest the DD(A)(A)g,g isomer is the GS, whereas the DD(A)(A)t,g isomer is predicted to be 1.7–2.2 and 0.4–0.8 kJ/mol higher in energy than the GS at 0 and 298 K, respectively. Again these isomers differ only in the orientation of the unprotonated NH_2 group. Similar to the $(N_2H_4)H^+(H_2O)$ complex, the relative energies of these two low-lying isomers at 298 K are small, such that Maxwell-Boltzmann populations are 54%–58% and 42%–46%, respectively. The TS that connects these two isomers is 6.2–10.0 kJ/mol higher in energy than the GS at all levels of theory, suggesting isomerization could occur at 298 K.

The higher energy isomers are sufficiently high in energy > 10.0 kJ/mol at all levels of theory, that their populations are likely to be negligible at 298 K. In all D(AD′)(A′) cases, these species involve a water molecule in a second solvent shell, which clearly weakens the interaction. Interestingly, even though the D,D(AD′)(AA′) isomers, which are similar to the lowest-lying isomer found by Dyczmons for the neutral analogue,[3] share additional hydrogen–bonding at the unprotonated nitrogen, they are

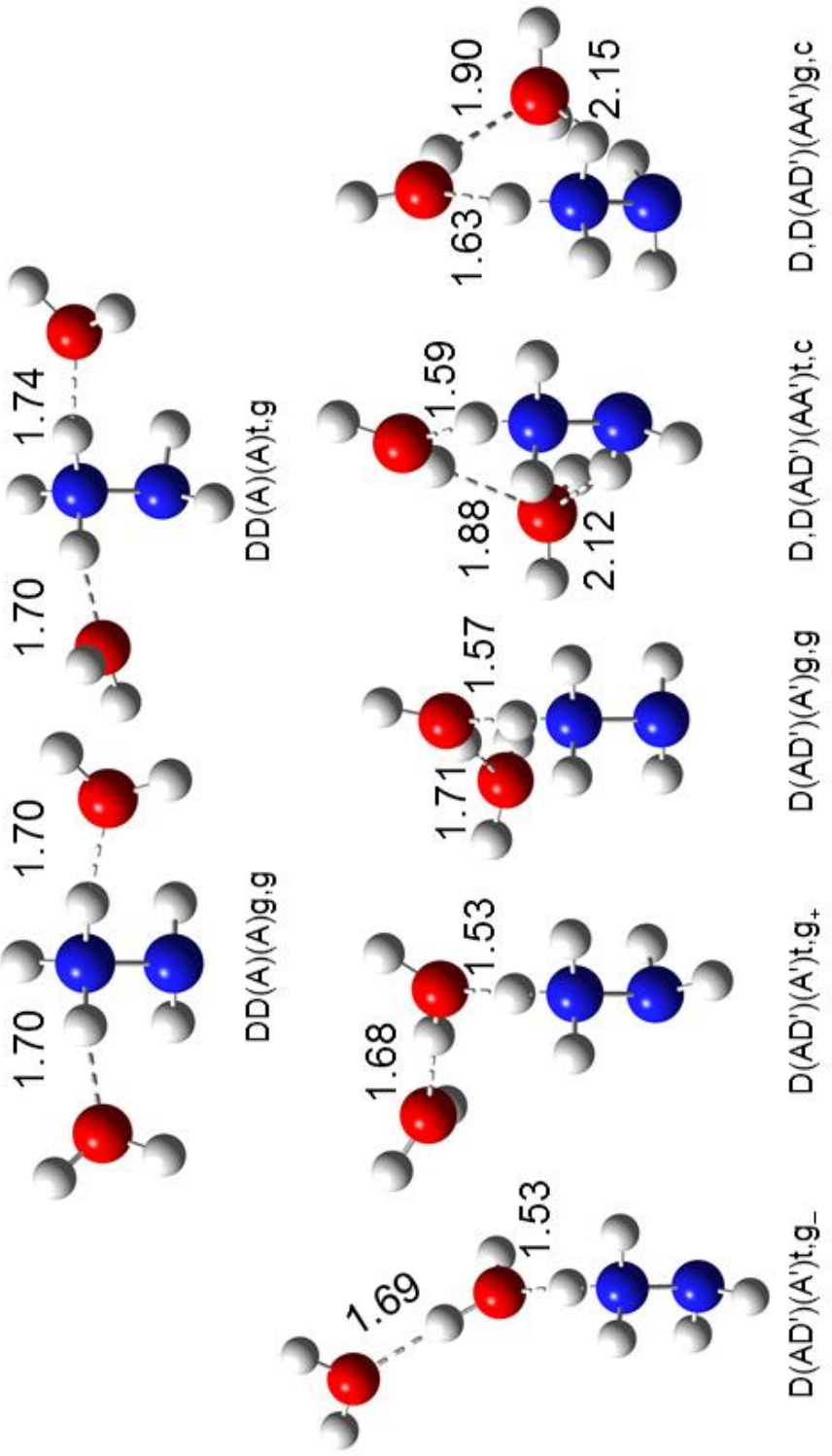

Figure 5.2. Isomers of $(N_2H_4)H^+(H_2O)_2$ calculated at the B3LYP-GD3BJ/6-311+G(d,p) level of theory. Hydrogen bonds are indicated by dashed lines with distances indicated in Å.

predicted to be > 10.7 kJ/mol higher in energy than the GS at all levels of theory. Therefore, unlike the neutral analogue, this suggests that cooperative interactions do not have a great effect on these protonated systems, where the charge is more highly localized, limiting the enhancement of local dipoles.

5.4.3 Theoretical Structures: $(UDMH)H^+(H_2O)$

For $(CH_3)_2NH^+NH_2(H_2O)$, isomers are named with the donor/acceptor nomenclature with α designating the protonated and methylated nitrogen and β indicating the protonated and unmethylated nitrogen. Additionally, the dihedral angles, g or t, between the water binding site and the hydrogens or methyl groups on the uncoordinated nitrogen are indicated. The isomers located are shown in Figure 5.3, with all energies listed in Table 5.1. All five levels of theory suggest that the D_α(A)t,g isomer is the GS at 0 K and the D_α(A)g,g isomer is the GS at 298 K. Both isomers have the water binding to the proton on the methylated nitrogen and differ only in the orientation of the NH_2 group. The relative energies of these two low-lying isomers at 298 K are small (0.2–1.7 kJ/mol), such that Maxwell-Boltzmann populations at 298 K are 52%–67% and 33%–48% for g,g and t,g, respectively. The TS that connects these two isomers is 7.7–10.4 kJ/mol higher in energy than the GS, suggesting these isomers will not readily interconvert at 298 K. When water binds to a proton on the unmethylated nitrogen, the relative energies for these isomers are 20–35 kJ/mol at all levels of theory. This is sufficiently high in energy that neither of these isomers should exhibit appreciable populations at 298 K. This difference is largely a consequence of the less stable protonation site as the unhydrated D_α isomers are lower in energy than D_β isomers by 26–35 kJ/mol, listed in Table 5.1.

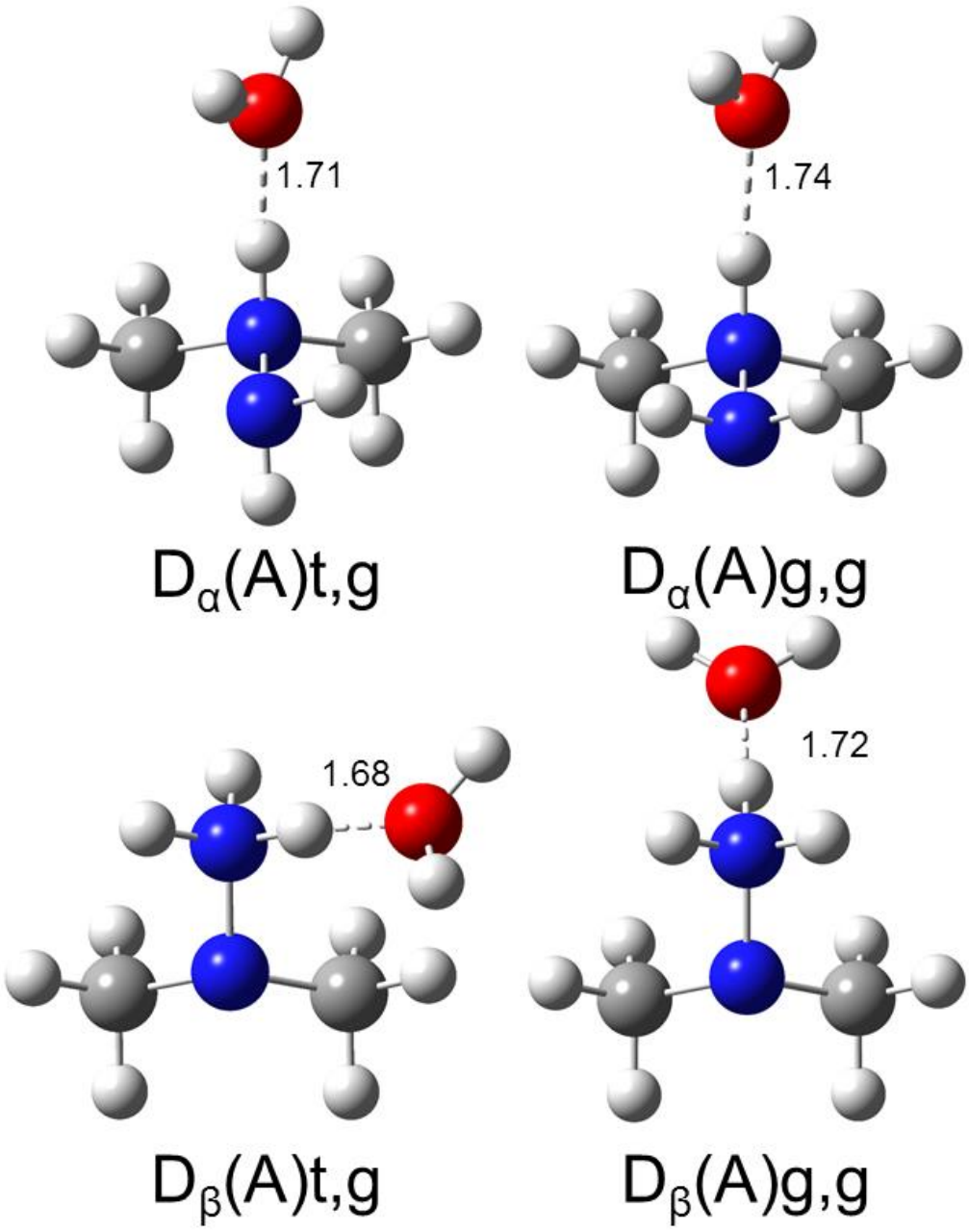

Figure 5.3. Isomers of $(UDMH)H^+(H_2O)$ calculated at the B3LYP-GD3BJ/6-311+G(d,p) level of theory. Hydrogen bonds are indicated by dashed lines with distances indicated in Å.

Note that hydration reduces this difference slightly, and thus the water stabilizes protonation of the less favorable unmethylated nitrogen.

5.4.4 Experimental Results

Experimental cross sections for collision-induced dissociation with Ar for $(N_2H_4)H^+(H_2O)_n$ where n = 1 and 2 and $(UDMH)H^+(H_2O)$ are shown in Figures 5.4(a)–5.4(c) after extrapolation to zero pressure. In all cases, the dominant fragment is a loss of a water molecule, with the n =2 complex showing sequential dissociation of a second water ligand as well. Analysis of all of these complexes using Eqs. (5.2) and (5.4) yields optimized parameters listed in Table 5.2. In all cases, it can be seen that the model reproduces the cross sections of both the primary and secondary products with fidelity throughout the threshold regions and up to at least 1–3 eV. For the n = 1 complex, the threshold for a loss of a single water molecule is 0.71 ± 0.02 eV. When the sequential model, Eqs. (5.2) and (5.4), is used for n = 2, we measure thresholds of 0.63 ± 0.03 eV for the primary dissociation channel and 1.57 ± 0.06 eV for loss of two water molecules. The difference between the primary and secondary thresholds should equal the $(N_2H_4)H^+(H_2O)$–(H_2O) bond energy, and is 0.94 ± 0.06 eV, somewhat higher than the primary threshold for n = 1. As in previous work, this latter secondary bond energy can be larger than the primary bond energy because a) the statistical assumptions used in Eq. (5.4) are not accurate and b) the energy deposition not as well controlled experimentally. Therefore, we take the primary threshold as our best determination of this bond energy. For the $(UDMH)H^+(H_2O)$, the analysis of the cross section, Figure 5.4(c), yields a threshold of 0.57 ± 0.03 eV for a loss of a water molecule, slightly smaller than that for

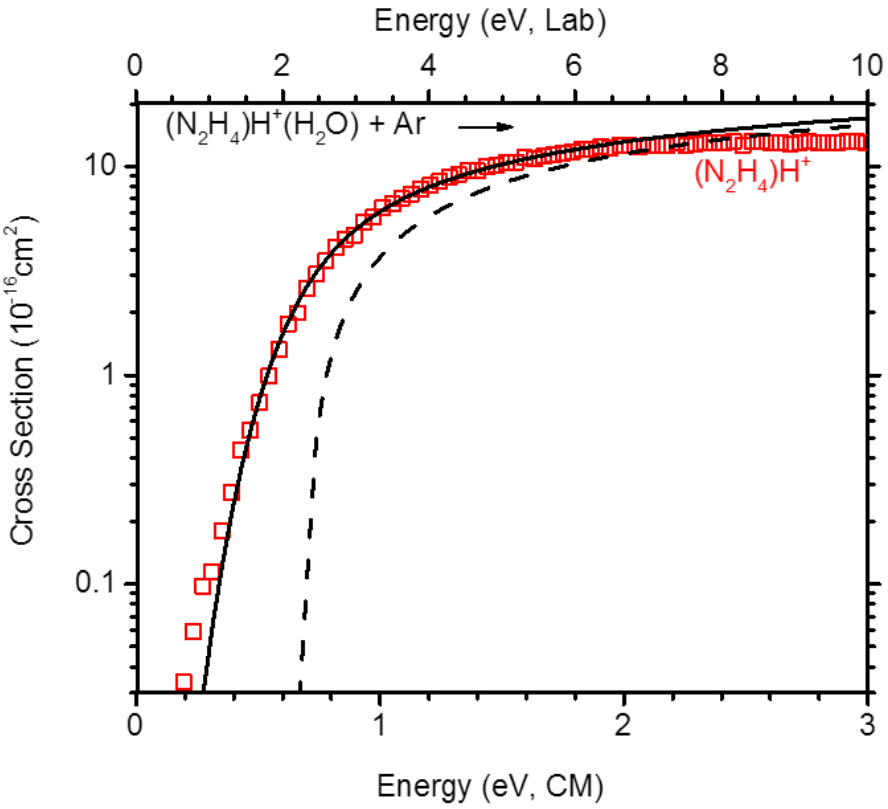

Figure 5.4. Zero pressure extrapolated cross sections for the CID with Ar of $(N_2H_4)H^+(H_2O)_n$ for n = 1 and 2 (parts a and b) and for $(UDMH)H^+(H_2O)$ (part c). Solid lines show the best fit to the primary (open red squares) and secondary (open blue triangles) product cross sections using Eq. (5.2) and Eqs (5.2) × (5.4) convoluted over the kinetic and internal energy distributions of the reactants. Dashed lines show the models in the absence of experimental kinetic energy broadening for reactants with an internal energy of 0 K. Optimized parameters for these models are found in Table 5.2.

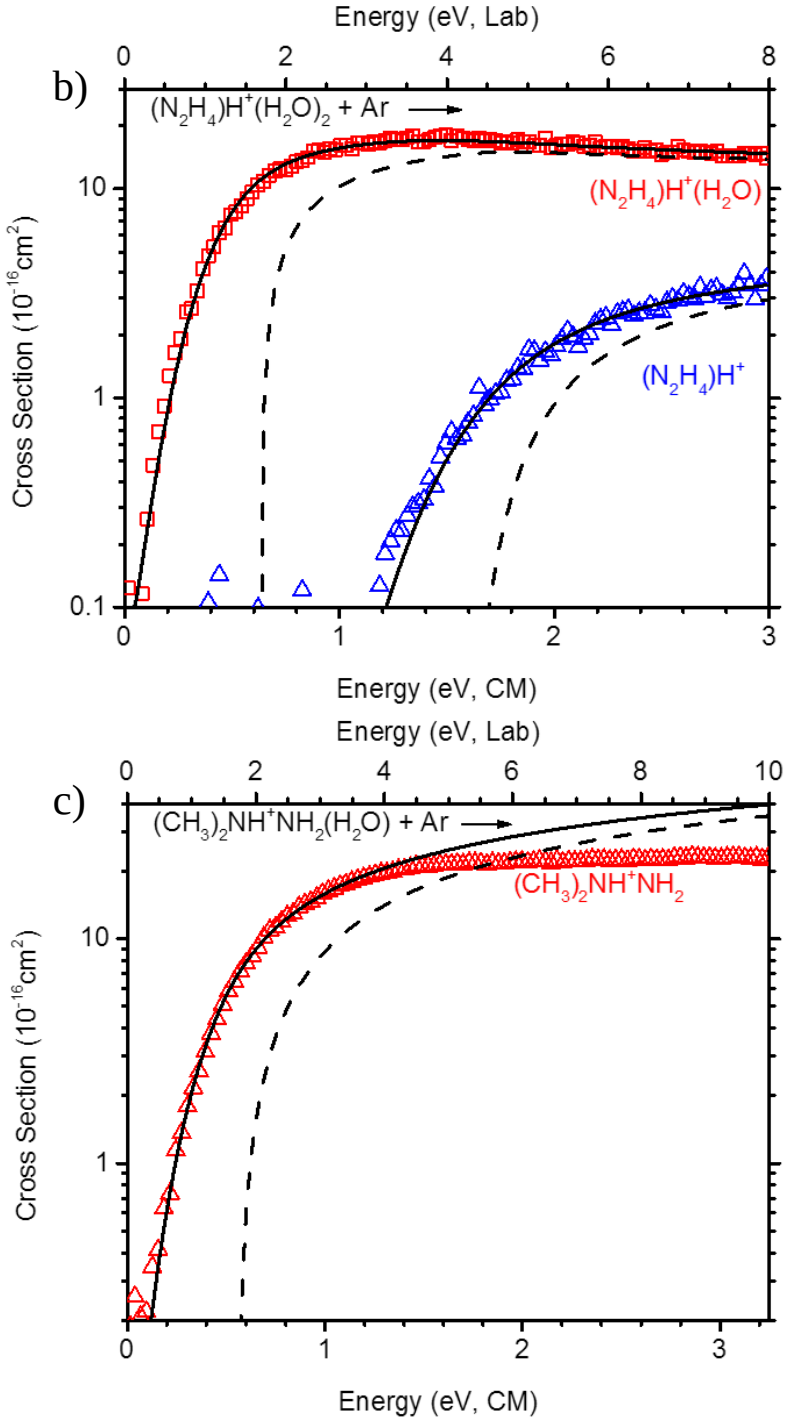

Figure 5.4. (Continued)

Table 5.2. Optimized parameters of equation (5.2) from analysis of CID cross sections[a]

reactant	product	σ_0 (Å^{2}eV^{1-N})[b]	N[b]	E_0 (eV)[b]	$\Delta S^{\dagger}_{1000}$ (J/mol K)
$(N_2H_4)H^+(H_2O)$	$(N_2H_4)H^+$	16.8 (1.1)	1.2 (0.1)	0.71 (0.02)	24 (2)
$(N_2H_4)H^+(H_2O)_2$	$(N_2H_4)H^+(H_2O)$	24.0 (3.8)	0.9 (0.1)	0.63 (0.03)[c]	11 (5)
	$(N_2H_4)H^+$	13.6 (1.1)		1.57 (0.06)[c]	9 (6)
$(CH_3)_2NH^+NH_2(H_2O)$	$(CH_3)_2NH^+NH_2$	27.7 (0.3)	1.3 (0.1)	0.57 (0.03)	18 (5)

[a] Uncertainties in parentheses. [b] Parameters for modeling where lifetime effects are taken into account. [c] Sequential dissociation modeling using Eq. (5.2) and Eqs. (5.2) × (5.4).

the unmethylated water complex. For all three of the complexes, lifetime effects are small, within the cited uncertainties.

In addition to the water-loss products, the one-water complex ions exhibited additional fragmentations corresponding to the dissociation of the protonated monomers at higher energies than shown in Figures 5.4(a) and 5.4(c). In both cases, these product ions have cross sections that are too small to be analyzed accurately and require > 4 eV. These dissociations can be examined much more accurately using CID studies of the protonated monomers, which is ongoing work. Larger protonated hydrazine and UDMH water clusters were not formed in our source. The B3LYP level of theory suggests the BDE for a loss of a water molecule from the three water cluster, $(N_2H_4)H^+(H_2O)_2$–(H_2O), is 0.54 eV at 0 K, only slightly above the average internal energy for this complex of 0.34 eV at 298 K. The fact that these values are comparable could explain why we were unable to create $(N_2H_4)H^+(H_2O)_3$ or larger complexes at 298 K. Clearly, methylation limits the extent of strong hydrogen bonding, such that the higher order $(UDMH)H^+(H_2O)_n$ clusters will also be weakly bound.

5.4.5 Comparison of Experimental and Theoretical Bond Energies: $(N_2H_4)H^+(H_2O)_n$ (n = 1 and 2) and $(CH_3)_2NH^+NH_2(H_2O)$

The primary thresholds represent our best experimental BDEs at 0 K for the $(N_2H_4)H^+(H_2O)_n$ complexes where n = 1 and 2, and $(UDMH)H^+(H_2O)$, and are listed in Table 5.3. Because these parent ions probably correspond to a distribution of the low-lying isomers of each complex, the experimental BDEs are compared to the 0 K theoretical BDEs weighted by their calculated Maxwell-Boltzmann populations at 298 K

Table 5.3. Comparison of experimental 0 K bond energies (kJ/mol) to theoretical values[a]

bond	expt[b]	B3LYP[c]	M06[c]	mPW1PW91[c]	PBE0[c]	MP2(Full)[c]	CCSD(T)[c]
$(N_2H_4)H^+(H_2O)_{n-1}$–(H_2O)							
n = 1	68.5 ± 1.9	73.1 (74.9) 78.0[d] (79.8)[d]	75.8 (77.8) 77.0[d] (79.0)[d]	74.0 (76.0)	76.2 (78.2) 79.2[d] (81.1)[d]	71.4 (77.5)	69.6 (75.5)
2	60.8 ± 2.9	59.3 (61.0) 64.0[d] (65.7)[d]	62.4 (64.3) 63.8[d] (65.7)[d]	59.6 (61.5)	61.7 (63.5) 64.5[d] (66.4)[d]	59.4 (65.2)	58.4 (64.0)
$(CH_3)_2NH^+NH_2$–(H_2O)							
	55.0 ± 2.9	57.0 (59.1) 63.6[d] (65.6)[d]	60.5 (62.8) 62.7[d] (65.0)[d]	58.1 (60.4)	60.6 (62.8) 64.8[d] (66.9)[d]	60.0 (67.0)	55.5 (62.3)
MAD[e]	2.6[f]	2.7 (5.1) 7.1[d] (8.9)[d]	4.8 (6.9) 6.4[d] (8.5)[d]	3.3 (4.5)	4.7 (6.7) 8.1[d] (10.0)[d]	3.1 (8.5)	1.3 (5.8)

[a] Theoretical values with (and without) BSSE corrections. [b] Primary threshold energies from Table 5.2. [c] Population weighted average BDE of low-lying isomers calculated at the indicated level using a 6-311+G(2d,2p) basis set and B3LYP-GD3BJ/6-311+G(d,p) optimized geometries. [d] Empirical dispersion included. [e] Mean absolute deviations from experimental TCID BDEs. [f] Mean experimental uncertainty.

at each level of theory. These are also included in Table 5.3 and shown in Figure 5.5. BSSE corrections were relatively small for B3LYP, M06, mPW1PW91, and PBE0 levels (<3 kJ/mol), whereas corrections for CCSD(T) and MP2(full) were slightly larger, 5–7 kJ/mol. The BSSE corrections with and without empirical dispersion functions are nearly identical. Overall, theory predicts BDEs in reasonable agreement with experiment with mean absolute deviations (MADs) ranging from 1 to 8 kJ/mol once BSSE corrections are included. Agreement with experiment is worse if BSSE corrections are not made. These differences are somewhat larger than the mean experimental uncertainty of 2.6 kJ/mol. MAD values for PBE0 and M06 without empirical dispersion are very similar, perhaps because they utilize similar HF exchange functions, whereas the MAD for mPW1PW91 is only slightly better, perhaps because it shares the same functional for noncovalent bonds as M06. Interestingly, the theoretical BDEs with empirical dispersion included adversely affect the MADs, which seems odd given that empirical dispersion is designed to treat hydrogen bonding more accurately. Overall, the CCSD(T) level of theory with BSSE provides the best agreement with experiment, although B3LYP (without empirical dispersion), MP2(full), and mPW1PW91 with BSSE results are only slightly farther off.

5.4.6 Comparison to Similar Proton-Bound Hydrated Complexes

As noted above, the 0 K BDE of the proton-bound UMDH one-water complex is 7.7 ± 3.5 kJ/mol lower in energy than the unmethylated complex. The origins of this difference can be explored by comparing similar systems, which have been evaluated thoroughly in a comprehensive review by Meot-Ner.[56] He notes that the formation of the hydrogen bonds connecting the proton-bound hydrated complexes involve partial proton

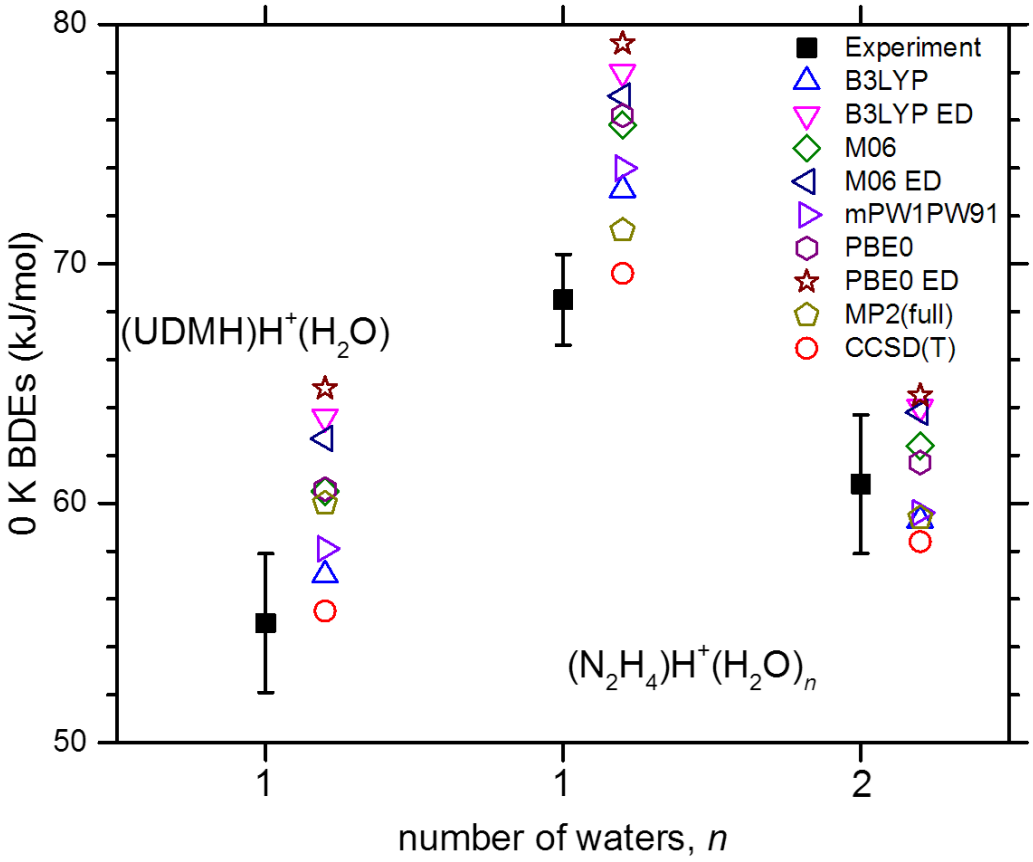

Figure 5.5. Comparison of 0 K bond energies for $(UDMH)H^+(H_2O)$ and $(N_2H_4)H^+(H_2O)_n$ (n = 1 and 2) obtained from experiment (primary thresholds, solid black squares) and theory (open symbols). All results are from Table 5.3. Data points for theoretical values are offset for clarity.

transfer from the donor to the acceptor, such that the bond strength is correlated with the efficiency of the proton transfer. Thus, the higher the difference in proton affinities (PAs) between the monomer and water, the less efficient the proton transfer, such that an inverse trend is found between the PAs of the monomers and the BDEs of the proton-bound hydrated complexes. This trend is shown by hydration energies of NH_3 that is stepwise methylated. These values are listed in Table 5.4 and shown in Figure 5.6 along with our experimental BDEs for comparison. The effect of dimethylation on NH_3 and N_2H_4 is similar, with increases of 76 and 74 kJ/mol, respectively, in the PAs and decreases of 17.8 and 13.5 kJ/mol, respectively, in the BDEs (indicated by the similar slopes of the correlations in Figure 5.6). The addition of an NH_2 group to NH_3 and $(Me)_2NH$ has a small effect, 0.3 and 2.6 kJ/mol, respectively, on the PAs of the monomers and a slightly greater effect on the BDEs, decreasing them by 12.1 and 7.8 kJ/mol, respectively. Likewise, the BDE for a second water ligand decreases by 3.1 kJ/mol going from NH_4^+ to $N_2H_5^+$. We believe this change in the BDEs is a consequence of differing hydrogen bonding associated with the NH_2 group. Examination of the low-lying isomers of the one-water complexes of protonated hydrazine and UDMH (Figures 5.1 and 5.3), show additional H-bonding interactions between the water molecule and the NH_2 group. These interactions apparently disrupt the binding to the protonated nitrogen, by changing the N-H-O angle by 3º–10^o in the direction of the NH_2 group when compared to the non-NH_2 substituted complexes, thus perturbing the alignment of the water dipole and the hydrogen bond. Interestingly, addition of the NH_2 group had an opposite effect on the BDEs for the proton-bound homodimers of ammonia versus hydrazine and UDMH.[8] In these cases, the additional NH_2 groups on *both* partners in the

Table 5.4. Representative thermochemistry (kJ/mol) of select proton-bound hydrated complexes

Monomer (B)	Proton Affinity (B)[a]	BDE, $BH^+ – H_2O$[b]	BDE, $(H_2O)BH^+ – H_2O$[b]
H_2O	690.4	136.0[b,c]	
NH_3	853.5	80.6[b,d]	63.9[b,d]
$MeNH_2$	899.1	74.5[b,e]	
$(Me)_2NH$	929.7	62.8[b,f]	
$(Me)_3N$	948.9	60.7[b,g]	
N_2H_4	853.2	68.5[h]	60.8[h]
$(CH_3)_2N_2H_2$	927.1	55.0[h]	

[a] Values from Ref. 57. [b] Values taken from Ref. 56.

[c] Average value from Refs. 58-62. [d] Average value from Refs. 61, 63, and 64.

[e] Average value from Refs. 63 and 65.

[f] Value from Ref. 63. [g] Average value from Ref. 63, 66, and 67.

[h] Experimental values from this work (Table 5.3)

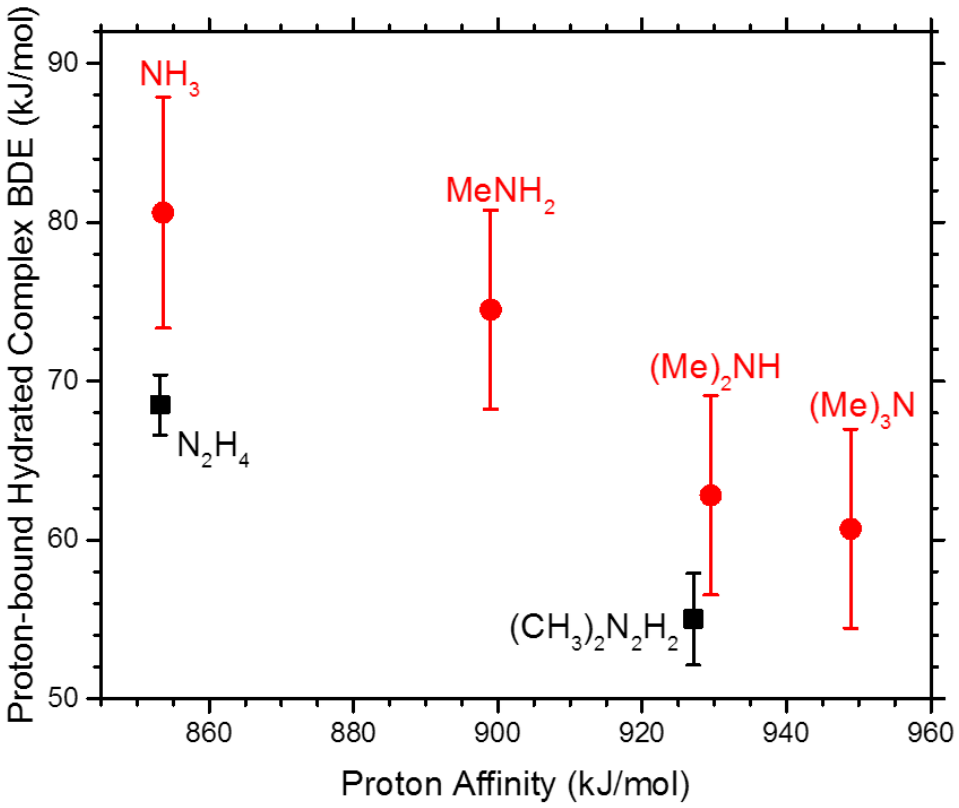

Figure 5.6. Inverse trend between the proton affinities of the neutral monomer (Ref. 60) and the bond dissociation energies of the proton-bound hydrated complex (current experimental values, solid black squares) and of substituted ammonia (Ref. 59, solid red circles).

homodimers allow additional hydrogen bonding interactions that strengthen the homodimer bond.

5.4.7 Conversion from 0 to 298 K Thermodynamics

A rigid rotor/harmonic oscillator approximation was applied to convert the 0 K bond energies into 298 K enthalpies and free energies. This was achieved using the theoretical vibrational frequencies scaled by 0.989 and rotational constants for a Maxwell-Boltzmann distribution of the low-lying isomers. The uncertainties in these conversions were obtained by scaling the vibrational frequencies up and down by 10%. These conversion factors were used to determine ΔH_{298} and ΔG_{298} values listed in Table 5.5. Note that this approximation may not be suitable for all cases because of the inaccuracy of low-frequency torsional motions and (as pointed out by a referee) that the entropy could include the entropy of mixing different conformers.

5.5 Conclusion

Energy-resolved threshold collision-induced dissociation with Ar is performed on $(N_2H_4)H^+(H_2O)_n$ where n = 1 and 2 and $(UDMH)H^+(H_2O)$. The primary dissociation pathway of all complexes is a loss of a single water molecule followed by the sequential loss of an additional water molecule for n = 2 at higher collision energies. Statistical analysis of the TCID data is used to obtain 0 K bond energies for all dissociation pathways. These energies are converted to obtain thermodynamic values at 298 K using a rigid rotor/harmonic oscillator approximation. The BDEs for the proton-bound hydrazine water clusters and proton-bound UMDH one-water complex are measured here for the

Table 5.5. Conversion of 0 K thresholds to 298 K enthalpies and free energies (kJ/mol)[a]

n	ΔH_0[b]	$\Delta H_{298} - \Delta H_0$[c]	ΔH_{298}	$T\Delta S_{298}$[c]	ΔG_{298}
		$(N_2H_4)H^+(H_2O)_{n-1}–(H_2O)$			
1	68.5 (1.9)	2.16 (0.48)	69.9 (0.5)	4.29 (0.12)	34.2 (2.9)
2	60.8 (2.9)	0.80 (0.37)	61.1 (3.7)	3.81 (0.16)	29.4 (4.2)
		$(CH_3)_2NH^+NH_2–(H_2O)$			
	55.0 (2.9)	0.74 (0.40)	56.2 (3.1)	3.96 (0.15)	23.3 (3.7)

[a] Uncertainties in parentheses. [b] Experimental values from this work, Table 5.3. [c] Values are calculated from the vibrational frequencies and rotational constants at the B3LYP-GD3BJ/6-311+G(d,p) level of theory. Uncertainties are found by scaling the frequencies up and down by 10%.

first time. For $n = 2$, the low-lying isomers prefer an open-chain structural motif over cyclic configurations, in contrast to previous work on neutral analogues, suggesting that cooperative interactions are not influential in the protonated system. The BDE for the protonated UDMH one-water complex is found to be weaker than the unmethylated one-water complex. This result is consistent with a previously noted trend that the BDEs of proton-bound hydrated complexes decrease with increasing proton affinity of the monomer.[56] The BDEs calculated at the B3LYP, M06, mPW1PW91, PBE0, MP2(full), and CCSD(T) levels of theory with and without BSSE and/or empirical dispersion also align nicely with the experimental values presented here. The CCSD(T) results reproduce the experimental BDEs the best. However, B3LYP, MP2(full), and mPW1PW91 levels of theory with BSSE and without empirical dispersion (B3LYP) provide reasonable reproduction of the experimental values.

5.6 References

[1]J. A. Gardner, R. A. Dressler, R. H. Salter *et al.*, J. Phys. Chem. **96**, 4210 (1992).

[2]M. H. Matus, A. J. Arduengo, and D. A. Dixon, J. Phys. Chem. A **110**, 10116 (2006).

[3]V. Dyczmons, J. Mol. Struct. **766**, 9 (2006).

[4]L. Carlsen, O. A. Kenesova, and S. E. Batyrbekova, Chemosphere **67**, 1108 (2007).

[5]J. Street, C. Johnston, L. Ou *et al.*, edited by A. F. E. a. S. Center (1988).

[6]U. Buck, X. J. Gu, M. Hobein *et al.*, Chem. Phys. Lett. **163**, 455 (1989).

[7]W. Y. Feng, V. Aviyente, T. Varnali *et al.*, J. Phys. Chem. **99**, 1776 (1995).

[8]C. P. McNary, and P. B. Armentrout, J. Phys. Chem. A **120**, 9690 (2016).

[9]T. Kim, A. V. Tolmachev, R. Harkewicz *et al.*, Anal. Chem. **72**, 2247 (2000).

[10]S. A. Shaffer, A. Tolmachev, D. C. Prior *et al.*, Anal. Chem. **71** (1999).

[11]S. A. Shaffer, D. C. Prior, G. A. Anderson *et al.*, Anal. Chem. **70** (1998).

[12]R. M. Moision, and P. B. Armentrout, J. Am. Soc. Mass Spectrom. **18**, 1124 (2007).

[13]A. L. Heaton, S. J. Ye, and P. B. Armentrout, J. Phys. Chem. A **112**, 3328 (2008).

[14]A. L. Heaton, R. M. Moision, and P. B. Armentrout, J. Phys. Chem. A **112**, 3319 (2008).

[15]T. E. Cooper, and P. B. Armentrout, Chem. Phys. Lett. **486**, 1 (2010).

[16]D. R. Carl, B. K. Chatterjee, and P. B. Armentrout, J. Chem. Phys. **132**, 044303 (2010).

[17]D. R. Carl, R. M. Moision, and P. B. Armentrout, J. Am. Soc. Mass Spectrom. **20**, 2312 (2009).

[18]K. M. Ervin, and P. B. Armentrout, J. Chem. Phys. **83**, 166 (1985).

[19]F. Muntean, and P. B. Armentrout, J. Chem. Phys. **115**, 1213 (2001).

[20]E. Teloy, and D. Gerlich, Chem. Phys. **4**, 417 (1974).

[21]N. F. Dalleska, K. Honma, L. S. Sunderlin *et al.*, J. Am. Chem. Soc. **116**, 3519 (1994).

[22]N. Aristov, and P. B. Armentrout, J. Phys. Chem. **90**, 5135 (1986).

[23]N. R. Daly, Rev. Sci. Instrum. **31** (1960).

[24]D. A. Hales, L. Lian, and P. B. Armentrout, Int. J. Mass Spectrom. Ion Processes **102**, 269 (1990).

[25]S. E. Stein, and B. S. Rabinovitch, Chem. Phys. Lett. **49**, 183 (1977).

[26]S. E. Stein, and B. S. Rabinovitch, J. Chem. Phys. **58**, 2438 (1973).

[27]T. Beyer, and D. F. Swinehart, Comm. ACM **16**, 379 (1973).

[28]D. G. Truhlar, B. C. Garrett, and S. J. Klippenstein, J. Phys. Chem. **100** (1996).

[29]K. A. Holbrook, M. J. Pilling, and S. H. Robertson, *Unimolecular Reactions* (Wiley, New York, 1996), 2nd edn.

[30]R. G. Gilbert, and S. C. Smith, *Theory of Unimolecular and Recombination Reactions* (Blackwell Scientific, London, 1990).

[31]P. B. Armentrout, and J. Simons, J. Am. Chem. Soc. **114**, 8627 (1992).

[32]M. T. Rodgers, K. M. Ervin, and P. B. Armentrout, J. Chem. Phys. **106**, 4499 (1997).

[33]P. B. Armentrout, J. Chem. Phys. **126**, 234302 (2007).

[34]E. F. Pettersen, T. D. Goddard, C. C. Huang *et al.*, in *J. Comput. Chem.*2004), pp. 1605.

[35]D. A. Case, V. Babin, J. T. Berryman *et al.*, University of California, San Francisco, 2014).

[36]M. Valiev, E. J. Bylaska, N. Govind *et al.*, Comput. Phys. Commun. **181**, 1477 (2010).

[37]M. J. Frisch, G. W. Trucks, H. B. Schlegel *et al.*, (Gaussian, Inc., Wallingford, CT, USA, 2009).

[38]A. D. Becke, J. Chem. Phys. **98**, 5648 (1993).

[39]R. Ditchfield, W. J. Hehre, and J. A. Pople, J. Chem. Phys. **54**, 724 (1971).

[40]S. Grimme, S. Ehrlich, and L. Goerigk, J. Comput. Chem. **32**, 1456 (2011).

[41]S. Grimme, J. Antony, S. Ehrlich *et al.*, J. Chem. Phys. **132**, 154104 (2010).

[42]Y. Zhao, and D. G. Truhlar, Theor. Chem. Acc. **120**, 215 (2008).

[43]J. P. Perdew, K. Burke, and M. Ernzerhof, Phys. Rev. Lett. **78**, 1396 (1997).

[44]C. Adamo, and V. Barone, J. Chem. Phys. **110**, 6158 (1999).

[45]C. Adamo, and V. Barone, Chem. Phys. Lett. **274**, 242 (1997).

[46]C. Adamo, and V. Barone, J. Chem. Phys. **108**, 664 (1998).

[47]A. D. Becke, J. Chem. Phys. **104**, 1040 (1996).

[48]C. Møller, and M. S. Plesset, Physical Review **46**, 618 (1934).

[49]M. J. Frisch, M. Head-Gordon, and J. A. Pople, Chem. Phys. Lett. **166**, 275 (1990).

[50]M. J. Frisch, M. Head-Gordon, and J. A. Pople, Chem. Phys. Lett. **166**, 281 (1990).

[51]M. Head-Gordon, and T. Head-Gordon, Chem. Phys. Lett. **220**, 122 (1994).

[52]M. Head-Gordon, J. A. Pople, and M. J. Frisch, Chem. Phys. Lett. **153**, 503 (1988).

[53]F. B. van Duijneveldt, J. G. C. M. van Duijneveldt-van de Rijdt, and J. H. van Lenthe, Chem. Rev. **94**, 1873 (1994).

[54]S. F. Boys, and R. Bernardi, Mol. Phys. **19**, 553 (1970).

[55]D. R. Carl, R. M. Moision, and P. B. Armentrout, Int. J. Mass Spectrom. **265**, 308 (2007).

[56]M. Meot-Ner, Chem. Rev. **112**, PR22 (2012).

[57]E. P. L. Hunter, and S. G. Lias, J. Phys. Chem. Ref. Data **27**, 413 (1998).

[58]M. DePaz, J. J. Leventhal, and L. Friedman, J. Chem. Phys. **51**, 3748 (1969).

[59]M. Meot-Ner, and F. H. Field, J. Am. Chem. Soc. **99**, 998 (1977).

[60]A. J. Cunningham, J. D. Payzant, and P. Kebarle, J. Am. Chem. Soc. **94**, 7627 (1972).

[61]M. Meot-Ner, and C. V. Speller, J. Phys. Chem. **90**, 6616 (1986).

[62]N. F. Dalleska, K. Honma, and P. B. Armentrout, J. Am. Chem. Soc. **115**, 12125 (1993).

[63]M. Mautner, J. Am. Chem. Soc. **106**, 1265 (1984).

[64]J. D. Payzant, A. J. Cunningham, and P. Kebarle, Can. J. Chem. **51**, 3242 (1973).

[65]Y. K. Lau, and P. Kebarle, Can. J. Chem. **59**, 151 (1981).

[66]M. S. El-Shall, G. M. Daly, J. Gao *et al.*, J. Phys. Chem. **96**, 507 (1992).

[67]M. Meot-Ner, and L. W. Sieck, J. Am. Chem. Soc. **105**, 2956 (1983).

CHAPTER 6

IRON CLUSTER – CO BOND ENERGIES FROM THE KINETIC ENERGY DEPENDENCE OF THE FE_N^+ (N = 4–17) + CO ASSOCIATION REACTIONS

6.1 Abstract

The energy dependences of size-selected Fe_n^+ cluster ions (n = 1–17) reacting with CO at low energies are studied using a guided ion beam tandem mass spectrometer equipped with a laser vaporization source. Below about 1 eV, all clusters with $n \geq 4$ form the Fe_nCO^+ association complex. The probability of this reaction increases with cluster size until the absolute cross sections equal the collision limit for $n > 10$, with those for n = 12 and 14 exceeding the collision limit. As the cluster size increases, a second pathway becomes prominent at higher energies. The kinetic energy dependence and absolute magnitudes of these cross sections are analyzed to extract cluster-CO binding energies, which are found to progressively decrease with increasing cluster size, consistent with a simple Coulomb model. For the largest clusters, these binding energies approach that of an extended surface at shallow hollow sites, whereas the higher energy feature correlates with binding energies for dissociatively chemisorbed C and O on an iron surface.

Reprinted from C. P. McNary, and P. B. Armentrout, Phys. Chem. Chem. Phys. 16, 26567 (2014), with permission from Physical Chemistry Chemical Physics.

6.2 Introduction

The interaction of carbon monoxide with iron is technologically important for diverse reasons, including synthetic fuel production using Fischer-Tropsch (F-T) chemistry[1] and for the catalytic growth of multi- and single-walled carbon nanotubes (SWNT).[2] In F-T synthesis, syngas (CO and H_2) reacts on the metal catalyst with alkanes being the most desirable products, although alkenes and alcohols are often formed as well. For SWNT synthesis, Smalley and co-workers[2] used a gas-phase reactor utilizing $Fe(CO)_5$ in the presence of a flow of carbon monoxide. At the catalytic conditions for nanotube growth, $Fe(CO)_5$ decomposes and forms iron clusters that serve as the catalytic centers for disproportionation of the CO feedstock in the Boudouard reaction, $Fe_n + 2\ CO \rightarrow Fe_nC + CO_2$.[3] In all of this chemistry, dissociative chemisorption of CO on the catalyst is required. Thus, physisorption of CO onto the catalyst surface should weaken the triple bond of CO, while the interaction of the metal with carbon, oxygen, and hydrogen must be sufficiently weak to allow subsequent reactions to occur. Weakening of the CO bond is classically described within the Blyholder model,[4] where the 5σ orbital of CO interacts with unoccupied orbitals of a metal center (σ donation), while filled metal *d* orbitals interact with the empty CO $2\pi^*$ orbitals (π back bonding).

Guided ion beam mass spectrometry is a powerful means to study the chemistry and thermodynamics of isolated metal cluster ions in the gas phase because it provides the kinetic energy dependence of reactions under single collision conditions. Analysis of these data provides size-specific cluster thermochemistry for a wide range of atomic and molecular adsorbates.[5-11] In addition, by examining the variation in this chemistry as the size of the metal clusters is systematically changed, insight into the thermochemistry of

surfaces can be obtained from the asymptotic behavior of larger clusters.[11,12-14] This gas-phase approach is an intriguing alternative to single crystal surfaces and powders for model studies of elementary reactions, particularly where the reactivity of defect sites (steps and kinks) on surfaces is of interest.

In this paper, we investigate the association reactions of iron metal cluster cations (Fe_n^+ with n = 1–17) with CO as a function of kinetic energy using guided ion beam tandem mass spectrometry. At energies below 1 eV, the n = 4–17 systems react exclusively to form Fe_nCO^+ complexes, even under single collision conditions. The observation of this reaction is interesting because the Fe_nCO^+ association complex always has sufficient energy to decompose back to reactants. Thus, the Fe_nCO^+ complexes have lifetimes that exceed their flight time through the instrument. Unlike collision-induced dissociation (CID) of a preformed Fe_nCO^+ complex, where collision with a nonreactive partner deposits a broad distribution of internal energies leading to dissociation, the association process forms Fe_nCO^+ complexes with well-defined distributions of internal energy and angular momenta, and a cross section for formation determined by the ion-molecule collision probability. Thus, the dissociation lifetime of the association complex is governed primarily by only one adjustable parameter, the 0 K binding energy, $D_0(Fe_n^+–CO)$, Fig. 6.1. By varying the collision energy forming the complexes, the lifetime of the Fe_nCO^+ complex can be systematically altered. This kinetic energy dependence can be modeled using statistical unimolecular decay theory,[15] thereby allowing measurement of these binding energies.

There are several previous studies of the gas-phase association reactions of carbon monoxide with metal clusters. Cox *et al*. first studied the association reactions of CO with

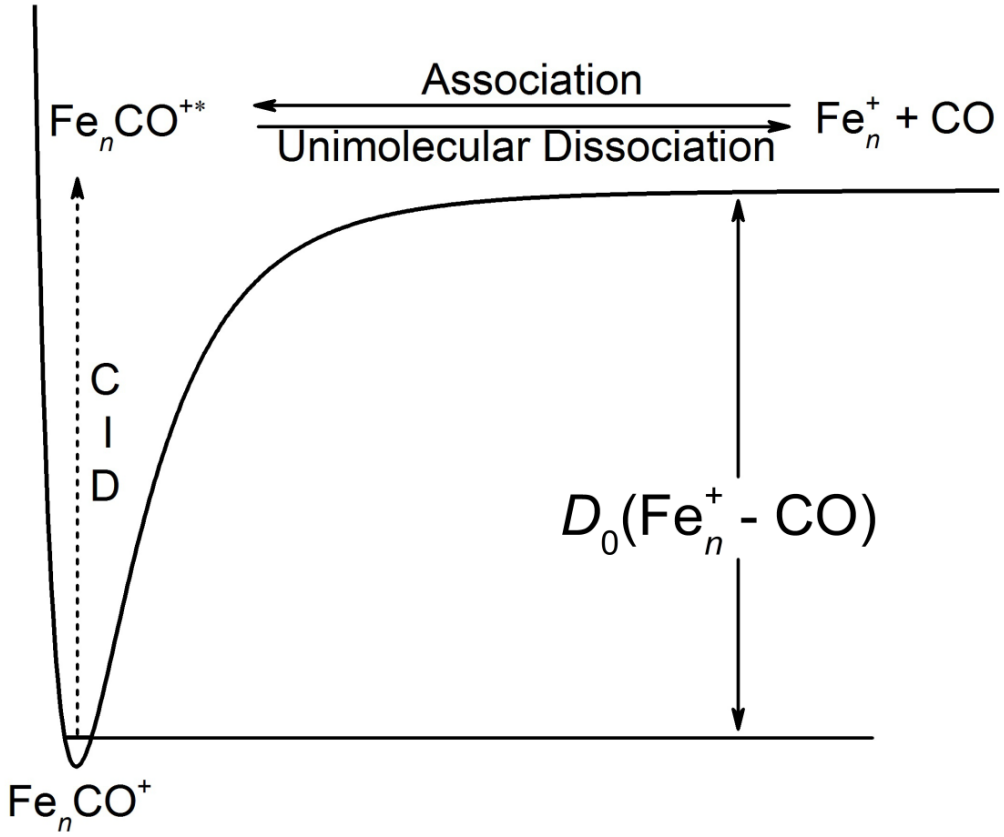

Fig. 6.1. Potential energy surface for association and collision-induced dissociation (CID) reactions. In a CID process, Fe_nCO^{+*} complexes are prepared by collisional excitation of complexes formed at room temperature, such that they have a broad internal energy distribution and unknown angular momentum distribution. In the association reactions, internally excited Fe_nCO^{+*} complexes are formed with well-characterized internal and angular momentum distributions by reacting the bare iron cluster with the CO neutral gas at room temperature. In both cases, Fe_nCO^{+*} complexes having internal energies in excess of $D_0(Fe_n^+–CO)$ undergo unimolecular dissociation to yield $Fe_n^+ + CO$.

many different neutral transition metal clusters using a flow tube under multiple collision conditions.[16] They found a range of reactivities, with iron showing formation of cluster carbonyls for n = 4–14. Qualitatively, they concluded that iron is among the metals that are least reactive with CO, suggesting relatively weak binding. Castleman and coworkers[17,18] examined the association reactions of CO with copper (n = 1–14) and cobalt (n = 2–9) cluster cations using a flow tube reactor under multiple collision conditions. They found that the adsorption rates were greatly affected by the pressure of CO and determined the saturation coverage of CO on cobalt clusters. Riley and coworkers[19,20] used a flow tube reactor under multiple collisions to study the saturation coverage of CO on nickel cluster cations (n = 2–20). They found that the saturation coverage depends on the size of the metal cluster, the temperature of the cluster carbonyl, and the pressure of CO. Beyer and coworkers have examined the effect of charge on CO-adsorption to group 5 (V, Nb, and Ta) and 9 (Co, Rh, and Ir) transition metal cluster cations and anions in the size range n = 1–30 using a Fourier transform ion cyclotron resonance (FT-ICR) mass spectrometer.[21,22] Their absolute reaction rates for the metal carbonyl species are both cluster size and charge dependent. In all of these studies, no quantitative thermodynamic information is obtained experimentally, information that might provide more predictive capability for understanding the CO adsorption process. This is one of the primary goals of the present work.

6.3 Experimental Methods

6.3.1 Guided Ion Beam Tandem Mass Spectrometer

The reactions of iron cluster cations with carbon monoxide are examined using a guided ion beam tandem mass spectrometer with a laser vaporization supersonic expansion source, which is described in detail elsewhere.[23] Briefly, a copper vapor laser (Oxford LM-100, 510 and 578 nm, 6 kHz repetition rate, 3–5 mJ/pulse) is tightly focused onto a rotating and translating iron rod (99.96%, Alfa Aesar). The plasma thus created is entrained in a continuous flow of helium at flow rates between 3000–8000 sccm. Prior to the helium entraining the plasma, the helium passes through a dual stage molecular sieve trap that is liquid nitrogen cooled to remove impurities. The clustering of the iron atoms and ions occurs in a 3 mm diameter, 6.4 cm long channel that immediately follows the ablation site. The average ion undergoes approximately ~10^5 collisions with He in this channel, which should be sufficient to equilibrate the ions to the temperature of the He carrier gas. The gas mixture expands from the clustering channel into the source chamber in a mild supersonic expansion that further cools the internal modes of the clusters. Iron clusters created are therefore believed to be fully thermalized and may be cooler.[24,25] The region between the ablation block and the skimmer is kept field free, and the focusing lenses in the two differential regions that follow are also kept at low potentials so that collisional reheating of the cluster ion is minimized.

The iron clusters ions are extracted from the source, focused into a magnetic sector for mass analysis, decelerated to a desired kinetic energy, and focused into a radio frequency (rf) octopole ion beam guide.[26] Reactions take place within the octopole, which passes through a collision cell where CO is introduced at low pressures. The octopole

beam guide utilizes rf electric fields to create a potential well to trap ions in the transverse direction without affecting their axial energy. Product and unreacted cluster ions drift out of the collision chamber to the end of the octopole, where they are extracted and focused into a quadrupole mass filter (QMF) for mass analysis (Extrel 3/4" Tri-Filter, 880 kHz). The pole bias of the QMF is varied to achieve maximum collection efficiency for the product and parent ions. The QMF has a mass limit of 1000 Da such that products up to $Fe_{17}CO^+$ can be studied. Finally, ions are detected by a 27 kV conversion dynode, secondary electron scintillation ion detector,[27] and the signal is processed using standard pulse counting techniques. Reactant and product ion intensities are converted to absolute cross sections as described previously.[23] Absolute cross sections measured in the laboratory have an uncertainty estimated as ±30% and relative uncertainties of ±5%.

Cross sections are broadened by thermal motion of the CO gas and the distribution of ion energies. The distribution and absolute zero of the ion kinetic energies are measured using the octopole as a retarding potential analyzer.[23] The uncertainty in the absolute energy scale is ± 0.05 (lab). The ion beam kinetic energy distributions have a full width at half-maximum (fwhm) of about 0.6–1.5 eV (lab), increasing with increasing cluster mass. Kinetic energies in the laboratory frame (lab) are converted to energies in the center-of-mass frame (CM) by using $E(\mathrm{CM}) = E(\mathrm{lab}) \times M / (M+m)$, where m is the cluster ion mass and M is the mass of carbon monoxide (28.01 amu). At very low energies, the conversion includes a correction for the truncation of the ion beam kinetic energy distribution.[23] Unless stated otherwise, all energies quoted in this paper correspond to the CM frame.

6.3.2 Model for Association Reactions

The association reaction cross sections were analyzed using a model devised by Koizumi and Armentrout[15] that explicitly conserves orbital angular momentum. This model assumes that the association and reverse dissociation processes occur on an ion-induced dipole + locked dipole potential surface, which provides an upper limit to the collision cross section as the relative collision energies of these studies are generally above those that might allow true dipole locking. (The addition of the locked dipole to the ion-induced dipole potential is a small effect because of the small dipole moment of CO.) Thus, formation of the complex with a specific internal energy and angular momentum distribution is assumed to be controlled by the collision cross section for the locked dipole (LD) model. The unimolecular decay rate coefficient is calculated for a transition state in the phase space limit (PSL).[28,29] Collisions with non-zero impact parameters produce rotating complexes because of angular momentum conservation. For the association reaction, conservation of angular momentum requires that the rotational angular momentum of the complex equals the orbital angular momentum of the reactants, as given by L = $\mu v b$, where μ is the reduced mass of the reactants, v is the relative velocity, and b is the impact parameter for the reaction. This relationship ignores the rotational angular momentum of the reactants, which should be a reasonable approximation, as discussed elsewhere.[15,30]

The energy dependences of the association cross sections are modeled with explicit conservation of orbital angular momentum according to eqn (6.1).

$$\sigma_{ass}(E) = \frac{\sigma_o \pi \hbar^2}{2E\mu} \sum_i g_i \int_0^{J_{max}} (2J+1) \exp\left[-k_{tot}\left(E^*, J\right)\tau\right] dJ \qquad (6.1)$$

Here E^* is the total available energy for the reaction defined as $E^* = E + E_i + E_0$, E is the

center-of-mass kinetic energy, $E_0 = D_0(Fe_n^+–CO)$, σ_o is an energy independent scaling parameter that is generally held to unity, and τ is the experimental flight time, ~100 μs. The summation is over the rovibrational states i of the reactants having energies E_i and populations g_i, where $\Sigma g_i = 1$. The Beyer-Swinehart-Stein-Rabinovitch algorithm[31,32] is used to evaluate the density of the rovibrational states of the Fe_n^+ reactants and the relative populations g_i are calculated by the appropriate Maxwell-Boltzmann distribution at 300 K. Vibrational frequencies for the bare cluster ions are obtained as outlined by Tan *et al*.[10] using an elastic model proposed by Shvartsburg *et al*.[33] J_{max} is the maximum orbital angular momentum defined by eqn (6.2),

$$J_{\max}(J_{\max}+1) = \left[\left(2\mu^2\alpha q^2 E/\pi\varepsilon_0\right)^{1/2} + \mu_D\mu^2 q/2\pi\varepsilon_o\right]/\hbar^2 \qquad (6.2)$$

which is derived from the expression for the locked dipole (LD) collision cross section, eqn (6.3).

$$\sigma_{LD}(E) = \pi\left(2\alpha q^2/4\pi\varepsilon_0 E\right)^{\frac{1}{2}} + (q\mu_D/4\varepsilon_o E), \qquad (6.3)$$

Here α is the polarizability volume of CO (1.957 Å^3),[34] q is the electron charge, ε_o is the permittivity of vacuum, and μ_D is the dipole moment of CO (0.1098 Debye).[35] When the exponential term in eqn (6.1) is unity, i.e., when the lifetime of the association complex greatly exceeds the flight time of the instrument, the integration of eqn (6.1) converges to $\sigma_{LD} \times \sigma_0$. Thus, the only adjustable parameters are E_0 and σ_0, where the latter is ideally held to unity.

The rate coefficients for unimolecular dissociation of the Fe_nCO^+ association complexes, $k_{tot}(E^*,J)$ in eqn (6.1), are calculated using Rice-Ramsperger-Kassel-Marcus (RRKM) theory.[36-38] The implementation of RRKM theory in the present work requires

the reaction degeneracy along with rotational constants and vibrational frequencies of the iron cluster cations and their association complexes. The vibrational frequencies for the association complexes are estimated as follows. Gutsev *et al.* performed DFT calculations to obtain electronic and geometric structures for the ground states of Fe_n^+ and Fe_nCO^+(n = 1–6).[39,40] Comparison of the vibrational frequencies of the bare and carbonylated iron cluster cations for n = 4–6 (which overlaps the range of the complexes studied here) shows that CO addition adds five frequencies between 38 and 443 cm^{-1} along with a CO stretch at 1687–1907 (1785 average) cm^{-1}. The latter values are comparable to the values near 1865 cm^{-1} found by Lyon *et al.*[41] in their infrared multiple photon dissociation (IRMPD) study of Fe_nCO (n = 18–28) complexes under thermal conditions. In the present case, the frequencies appropriate for Fe_nCO^+ complexes can be estimated by using those for the Fe_{n+2}^+ cluster, calculated as described above, and replacing a mode near 180 cm^{-1} with a CO stretch of 1800 cm^{-1}. This is because the additional five frequencies (Fe–CO bends, wags, and stretches) have a comparable dispersion to the Fe-Fe modes. The rotational constants of the bare and association complex cluster cations are calculated as detailed in our previous work.[5] Briefly, we assume a spherical cluster geometry for the bare and association complex cluster, where the radius of the sphere is calculated using a body-centered cubic crystal packing pattern similar to the model used by Shvartsburg *et al.*[33]

Before comparing the model with the experimental data, the thermal motion of the neutral gas and the kinetic energy distribution of the parent ions are both convoluted into eqn (6.1) as described previously.[15,23] The overall uncertainty associated with E_0 is determined by analyzing multiple zero-pressure extrapolated data sets, varying the

vibrational frequencies by ±30% (which includes any uncertainties associated with the added CO modes), varying the time-scale of the experiment by factors of approximately 2 (where the lower time limit was estimated by the mass dependent average flight times of 25–40 μs), and including the uncertainty in the absolute energy scale (0.05 eV_{Lab}).

6.4 Results

6.4.1 Experimental Cross Sections and Their Pressure Dependence

Reactions of CO with Fe_n^+, n = 1–17, were examined in the energy range below 1 eV. No products were observed for n = 1–3, whereas n = 4–17 all exhibited formation of the association complex, reaction (6.4).

$$Fe_n^+ + CO \rightarrow Fe_nCO^+ \qquad (6.4)$$

Other possible products, $Fe_{n-1}CO^+$, Fe_nC^+, Fe_nO^+, and Fe_n^+ were looked for and not observed at these energies, which indicates that the Fe_nCO^+ products must dissociate exclusively back to reactants, $Fe_n^+ + CO$, a dark channel that cannot be explicitly monitored. The failure to observe the Fe_nCO^+ complexes for the smallest cluster reactants, n = 1–3, is because these complexes, which are probably formed transiently, decompose back to reactants on a time scale faster than the experimental flight time. No attempt to form such complexes at higher CO pressures was made because no thermodynamic information can be gleaned from such observations. Our observation of Fe_nCO^+ complexes is comparable to that of Cox *et al.*,[16] who observed CO association to Fe_n for n = 4–14, but not to n = 1–3, at thermal energies even under multicollision conditions. Their instrumental time window of 160 μs is comparable to that in the present

experiments, 100 μs. Importantly, the failure to observe products such as $Fe_{n-1}CO^+$, Fe_nC^+, and Fe_nO^+ over this energy range may suggest that dissociative chemisorption is not occurring. At higher energies, such products are observed, consistent with activation of the CO bond, e.g., see Fig. 6.S1 of the Electronic Supplemental Material.

Experimental cross sections for cluster sizes Fe_n^+, n = 4–17, were taken at several different pressures, approximately 0.2, 0.1, 0.05 mTorr for clusters n = 4–7 and approximately 0.05, 0.025, and 0.0125 mTorr for clusters n = 8–17. In all cases, the experimental cross sections show a clear pressure dependence on CO, which indicates collisional stabilization of Fe_nCO^+ by secondary collisions. Indeed, $Fe_n(CO)_2^+$ products could be observed for $n > 10$ and clearly must result from secondary collisions. Our cross sections show a linear dependence on CO pressure for all cluster sizes at all energies. For small clusters, $n < 7$, the cross sections increase with increasing CO pressure, indicating that secondary collisions are stabilizing association complexes that otherwise would dissociate. For larger clusters, $n \geq 7$, the linear pressure dependence is inverse, such that higher pressures in the collision cell yield lower reaction cross sections. For the largest clusters, this is partially attributable to the secondary attachment of CO, coupled with scattering of the product complexes such that they are no longer transmitted to the detector. The effects of secondary collisions can be removed by adding the experimental cross sections for $Fe_n(CO)_2^+$ to those for Fe_nCO^+ and then linearly extrapolating the cross section data to zero CO pressure.[42] Such zero pressure extrapolated cross sections for representative cluster sizes are shown in Fig. 6.2, with Fig. 6.S2 of the Electronic Supplementary Information showing results for all cluster sizes.

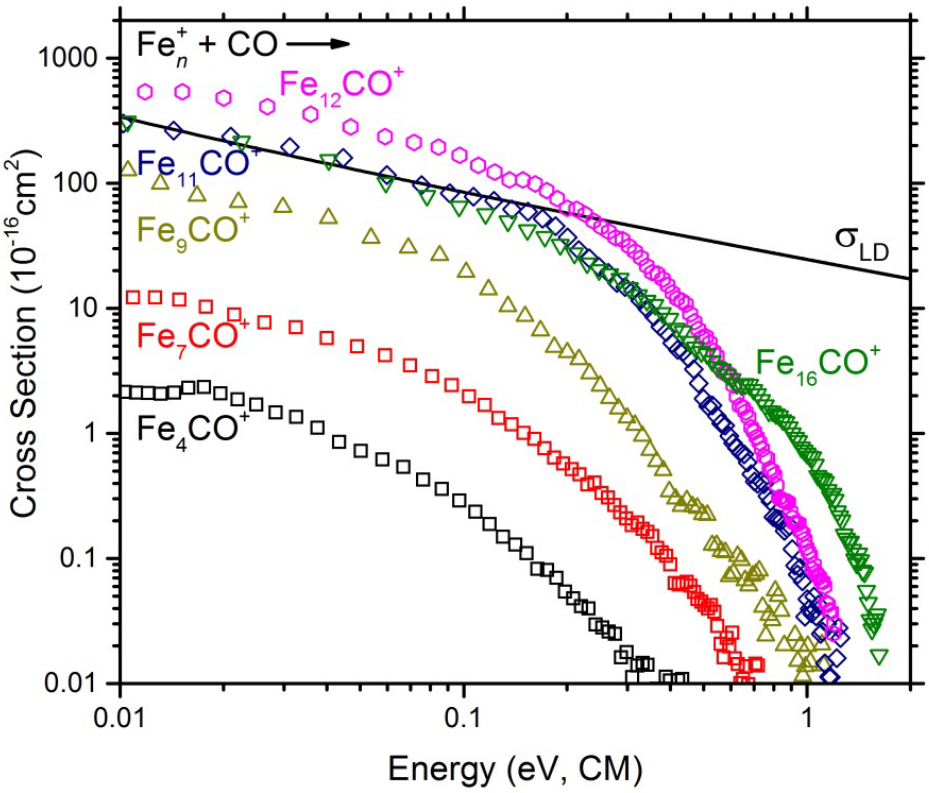

Fig. 6.2. Zero-pressure extrapolated experimental cross sections for reactions of Fe_4^+, Fe_7^+, Fe_9^+, Fe_{11}^+, Fe_{12}^+, and Fe_{16}^+ with CO as a function of kinetic energy in the center-of-mass frame. The locked dipole (LD) collision cross section, eqn (6.3), is shown by the solid line.

6.4.2 Experimental Cross Sections and Their Energy Dependence

It can be seen that the cross sections for reaction (6.4) generally increase with cluster size, increasing from about 2 $Å^2$ for $n = 4$ to about 600 $Å^2$ for $n = 12$ at the lowest energies examined. This trend is consistent with the idea that the lifetimes of the complexes increase as the number of degrees of freedom in the complex increases. In all systems, the association complexes exhibit cross sections that decline with increasing energy, consistent with exothermic barrierless processes, as must be the case for this association reaction, Fig. 6.1. For all cluster sizes, the cross sections decline more rapidly at higher energies, indicating faster dissociation. However, the largest clusters, in particular $n = 15–17$, clearly show a second feature in the cross sections, e.g., compare the shape of the cross section for $Fe_{16}CO^+$ with that for $Fe_{11}CO^+$. The extent of this second feature becomes more evident when the cross sections are modeled, as detailed below.

At low kinetic energies, the efficiency of these processes can be assessed by comparison to models for the collision cross section. For most exothermic ion-molecule reactions, the Langevin-Gioumousis-Stevenson (LGS) collisional capture cross section model[43] describes the collision probability for a polarizable molecule and is given by the first part of eqn (6.3). An upper limit to the collision cross section for a molecule having a permanent dipole is provided by the locked dipole (LD) model of eqn (6.3).[44] This collision cross section model is shown in Fig. 6.2. For smaller clusters, $n < 11$, the cross sections lie below the collision limit, whereas once $n \geq 11$, the Fe_nCO^+ cross sections at low energies lie at or above σ_{LD}, indicating 100% reaction efficiency.

For $n = 11, 13, 15–17$, the experimental cross sections match the σ_{LD} collision

cross section within the 30% experimental uncertainty (average deviation of 5 ± 17 %). Interestingly, the cross sections for n = 12 and 14 exceed the collision limit by factors of 2.1 ± 0.6 and 1.7 ± 0.5, respectively. As a consequence, these results were checked and reproduced carefully. Similar observations have been made previously for metal cluster ion-CO interactions by Beyer and coworkers using FT-ICR mass spectrometry at thermal energies.[21,22] They observed abnormally large experimental rates (as much as a factor of 3) compared to the average dipole orientation (ADO) rate[44-46] for the association reactions of group 5 and group 9 transition metal cluster cations and anions. Kummerlöwe and Beyer proposed a simple model to qualitatively explain such large collision cross sections.[22] Their surface charge capture (SCC) model treats the metal cluster as an ideally conducting sphere with the point charge free to move within its geometric boundaries. As the neutral molecule approaches, the charge is drawn to the closest point on the surface of the cluster, thereby enhancing the electrostatic long-range interaction by the geometric radius of the cluster. The latter is represented by the hard sphere (HS) model where the radius of the cluster is determined by assuming a spherical cluster with the same density ρ as the bulk, which for Fe is 7.874 g/cm^3.[47] The radius of the cluster can be estimated by by $r_{cluster} = n^{1/3} r_{Fe} = (3nm_{Fe}/4\pi\rho)^{1/3}$where r_{Fe} and m_{Fe} denote the atomic radius and mass of iron. The radius of CO is derived from the viscosity of CO, η = 1.78 μPa,[47] at 300 K, $r_{CO} = (25 m_{CO} k_B T/\pi\eta^2)^{1/4}/8$ = 1.86 Å. Fig. 6.3 shows our cross sections at thermal energies converted to rate constants using procedures outlined earlier,[23] along with rates calculated using the HS, LD, and SCC models. As for the cross sections, the smaller cluster sizes fall well below the collision limits, with those for n = 11, 13, 15–17 agreeing nicely with the LD prediction. Our results for n = 12 and

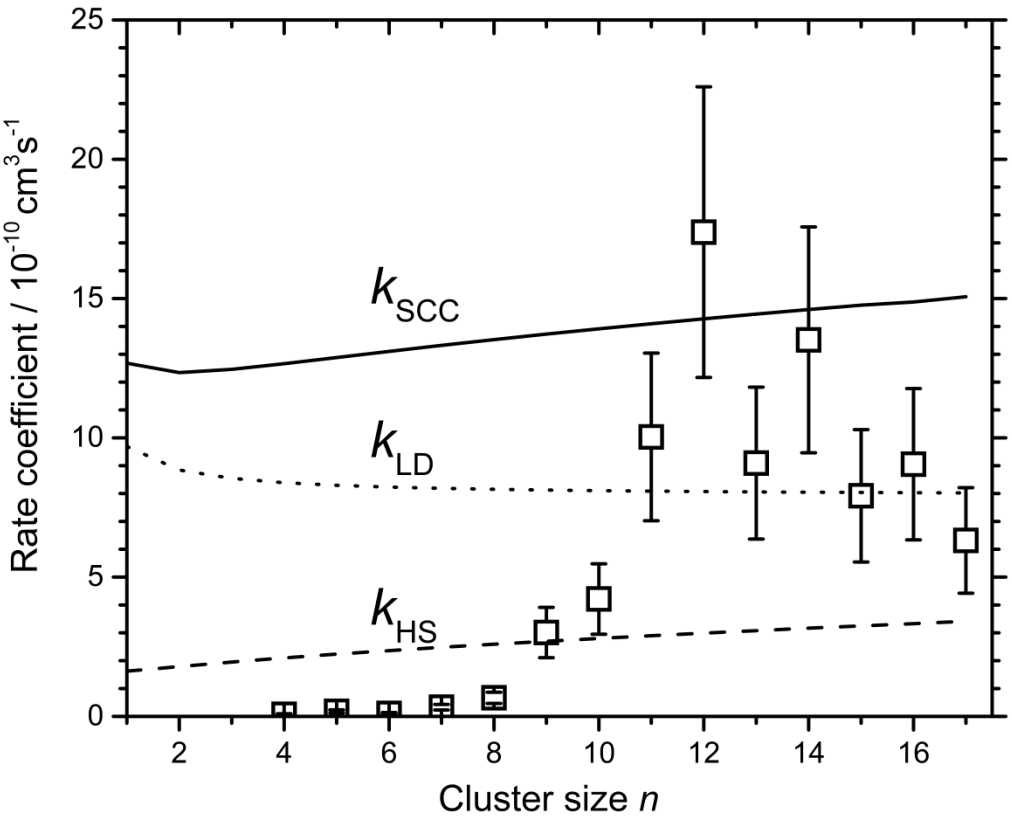

Fig. 6.3. Experimental (symbols) and theoretical (lines) reaction rate coefficients for Fe_4^+ + CO. The hard sphere k_{HS} (dashed line), locked dipole k_{LD} (dotted line), and surface charge capture k_{SCC} (solid line) models are shown.

14 agree with the SCC model within experimental uncertainty. These results deviate from the observations of Kummerlöwe and Beyer in that they observed a gradual increase in the reaction rates with cluster size, whereas we see strong fluctuations. There is no obvious explanation for why n = 12 and 14 are unique in their enhanced rates, as the thermochemistry derived below indicates that these clusters do not bind CO more strongly than adjacent cluster sizes. It is possible that this is related to the geometric and thermodynamic stability of the cluster cations. In particular, Fe_{13}^+ and Fe_{15}^+ are relatively thermodynamically stable,[48] suggesting that Fe_{12}^+ and Fe_{14}^+ may have either vacancies or adatoms that enhance their reactivity in a manner consistent with the SCC model (perhaps by extending the effective cluster radius). X-ray magnetic circular dichroism spectroscopy results on small cationic clusters provide some support for this hypothesis.[49,50] Here, Fe_{13}^+ is observed to have an exceptionally low magnetic moment compared with its neighbors, consistent with antiferromagnetic coupling of the central atom to the atoms of a distorted icosahedral shell.[49,50] Thus, removing or adding one atom to such a symmetric cluster could plausibly lead to the behavior observed here.

6.4.3 Thermochemical Analysis of the Association Reactions

The association model of eqn (6.1) is compared with the experimental results for several representative cluster sizes in Fig. 6.4. Results for all clusters are presented in the Electronic Supplementary Information, Fig. 6.S2. The parameters of eqn (6.1) used in these models are collected in Table 6.1. It can be seen that the model meets with varying success. For the Fe_{11}^+ association reaction with CO, Fig. 6.4c, the cross section at low energies lies 1.35 ± 0.13 higher than σ_{LD}, within the ±30% uncertainty in the absolute

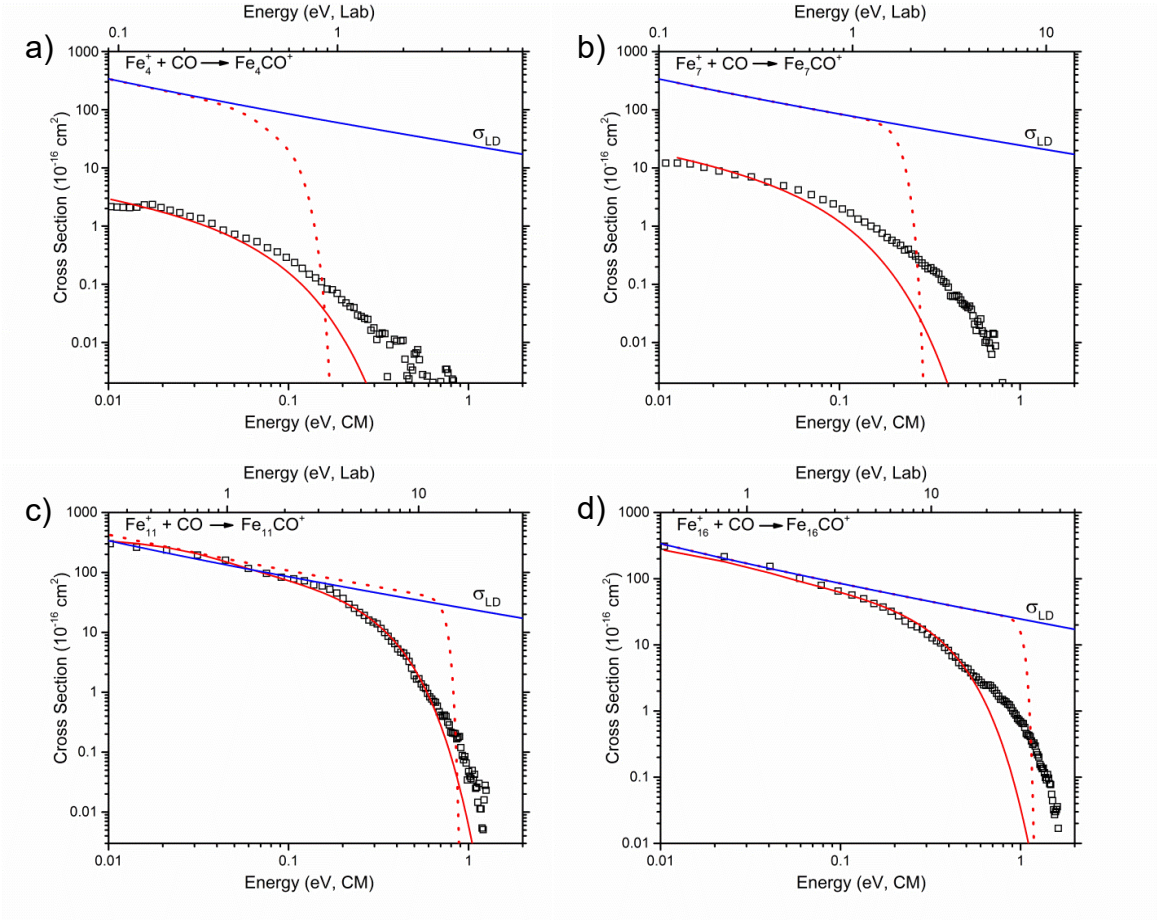

Fig. 6.4. Zero-pressure extrapolated experimental cross sections (symbols) for the association reactions of Fe_4^+, Fe_7^+, Fe_{11}^+, and Fe_{16}^+ (parts a–d) with CO as a function of kinetic energy in the center-of-mass (lower x-axis) and laboratory (upper x-axis) frames. The solid red line is the model of eqn (6.1) using the single model parameters in Table 6.1. The dashed line shows the model in the absence of experimental internal and kinetic energy distributions. The locked dipole cross section, σ_{LD}, eqn (6.3), is also indicated.

Table 6.1. Summary of bond energies (in eV) for $D_0(Fe_n^+\text{-CO})$ and scaling factors of eqn (6.1)[a]

	Single model Primary Feature		Dual model, Primary Feature		Dual model, Secondary Feature	
n	σ_0	$D_0(Fe_n^+$-CO)	σ_0	$D_0(Fe_n^+$-CO)	σ_0	$D_0(Fe_n^+$-CO)
4	1.00	2.84 (0.42)	1.00	2.80 (0.47)	0.005 (0.002)	6.0 (0.5)
5	1.00	2.26 (0.38)	1.00	1.98 (0.26)	0.003 (0.002)	4.0 (0.5)
6	1.00	1.87 (0.40)	1.00	1.68 (0.19)	0.003 (0.002)	3.8 (0.4)
7	1.00	1.64 (0.18)	1.00	1.74 (0.21)	0.005 (0.001)	3.51 (0.42)
8	1.00	1.63 (0.21)	1.00	1.60 (0.11)	0.007 (0.001)	3.56 (0.31)
9	1.11 (0.20)	1.79 (0.13)	1.00	1.77 (0.12)	0.018 (0.001)	2.71 (0.22)
10	1.00	1.79 (0.09)	1.42 (0.32)	1.72 (0.10)	0.015 (0.005)	2.90 (0.13)
11	1.35 (0.13)	1.88 (0.08)	1.00	1.92 (0.09)	0.087 (0.006)	2.42 (0.16)
12	2.73 (0.29)	1.78 (0.09)	3.57 (0.52)	1.70 (0.08)	0.057 (0.005)	2.51 (0.12)
13	1.00	1.86 (0.09)	1.00	1.80 (0.07)	0.044 (0.011)	2.51 (0.17)
14	1.91 (0.18)	1.72 (0.08)	2.26 (0.28)	1.65 (0.08)	0.052 (0.008)	2.34 (0.16)
15	1.05 (0.15)	1.58 (0.07)	1.25 (0.21)	1.48 (0.07)	0.099 (0.002)	2.19 (0.12)
16	1.13 (0.15)	1.55 (0.07)	1.00	1.52 (0.06)	0.098 (0.003)	2.16 (0.14)
17	0.91 (0.26)	1.50 (0.07)	1.00	1.44 (0.05)	0.047 (0.001)	2.31 (0.14)

[a] Uncertainties in parentheses.

cross sections. To best reproduce these data, this factor is used as the scaling factor σ_0 in eqn (6.1) while $E_0 = D_0(Fe_{11}^+–CO)$ is allowed to vary. The model shown uses $E_0 = 1.88 \pm 0.08$ eV and can be seen to reproduce the cross section over two orders of magnitude in energy and three orders of magnitude in cross section. This agreement validates the overall approach used here. The dashed line shows the model in the absence of the distributions of translational and internal energies of the reactants and properly reflects the lifetime of the complex as a function of energy truncated at the flight time through the instrument. Below a cross section of about 0.5 Å^2 at the highest energies, the model no longer reproduces the data, as discussed further below.

Comparably good model cross sections are obtained for $n = 12–14$ (again allowing σ_0 to vary slightly to best recreate the experimental cross section magnitude, Table 6.1), whereas both smaller and larger clusters show more obvious deviations at higher energies. Figs. 6.4a, 6.4b, and 6.4d show the examples of $n = 4$, 7, and 16, which are representative of the behavior of smaller and larger clusters. In all cases, the parameters of the model are chosen to best fit the experimental cross sections at low energies, with the optimized parameters listed in Table 6.1. Note that σ_0 is held to unity for the smaller clusters, i.e., the variation in the magnitude of the cross section model relies entirely on the value of $E_0 = D_0(Fe_n^+–CO)$. It can be seen that the model reproduces the data for $Fe_{16}CO^+$ with fidelity over extended ranges of energy and magnitude, but the deviation at higher energies is much larger than for $Fe_{11}CO^+$. The same is true for $n = 15$ and 17. For the smaller clusters, the deviations between the data and the model extend over larger energy ranges, but are of comparable size to the larger clusters in terms of the absolute cross section magnitude, i.e., the deviations are generally

less than 1 Å^2. Therefore, the deviations remain about the same absolute size but extend over larger energy ranges because the overall cross sections of the smaller clusters have smaller magnitudes.

As noted above, the comparison of the cross sections for Fe_{11}^+ and Fe_{16}^+ in Fig. 6.2 strongly suggests that the difference in behavior at higher energies is a distinct feature in the cross section. This observation implies that a new reaction pathway may become available. One possibility would be dissociative chemisorption, i.e., formation of the physisorbed Fe_nCO^+ species at low energy and chemisorbed CFe_nO^+ at higher energies. As noted above, if this were the case, one might expect to observe products like Fe_nC^+ or Fe_nO^+, although these would require considerable energy to induce loss of C or O atoms. More likely, if CFe_nO^+ were formed, then a potential competitive dissociation pathway would be loss of atomic Fe to form $Fe_{n-1}CO^+$, which also is not observed until much higher energies (Fig. 6.S1 in the Electronic Supplementary Information). This could suggest that dissociative chemisorption cannot explain the higher energy feature, but this presumes that the CO recombinative desorption energy is larger or comparable to the metal-metal bonds. We discuss this comparison further below.

Another possible explanation is that a different binding site with a different adsorption energy becomes available, perhaps because the higher collision energies anneal the clusters. To explore both possible explanations further, we model the high energy behavior again using eqn (6.1). This clearly requires a higher value of E_0 so that the lifetime of the Fe_nCO^+ complex extends to higher energies, but a lower value of σ_0 in order to match the smaller magnitude of the high energy features. The results of such dual model fits of the data are shown in Fig. 6.5 for n = 4, 7, 11, and 16, with the fitting

parameters in Table 6.1. Fig. 6.S2 in the Electronic Supplementary Information shows these models for n = 4–17. Now, the model reproduces the data for all cluster sizes over more than four orders of magnitude in cross section and the entire energy range. In most cases, the optimum E_0 value for the low energy feature differs by less than 0.1 eV from that found without considering the high energy feature, with larger differences (0.28 and 0.19 eV) for n = 5 and 6, respectively. For n = 11–17, the magnitude of the high energy feature is relatively constant at 4%–10% and the E_0 values are 0.66 ± 0.09 eV higher than those for the low energy feature. For the n = 4–10 clusters, the magnitudes are smaller, 0.3%–2 % and the E_0 value differences become larger. If the high energy feature really does correspond to a distinct site on the clusters, then the σ_0 value should be a relative measure of this site's probability coupled with the sticking probability at this site. Hence, it is reasonable to expect that the probability of having such a site is larger for the larger clusters, as we observe. In most cases, the E_0 value seems of a reasonable magnitude but that for n = 4 seems excessively large for this noncovalent (donor–acceptor) interaction. In this regard, the E_0 values for the higher energy feature must be viewed somewhat skeptically because they are no longer constrained by the σ_0 value being fixed.

6.5 Discussion

6.5.1 Trends in the Fe_n^+–CO Bond Energies as a Function of Cluster Size

The $D_0(Fe_n^+–CO)$ values derived from analysis of the association reactions are shown in Fig. 6.6. Excluding the two very large values for n = 4 and 5, the primary 0 K Fe_n^+–CO binding energies for n = 6–17 clusters have an average of 1.71 ± 0.13 eV with the highest values (n = 6, 9–13) averaging 1.82 ± 0.04 eV. For the secondary bond

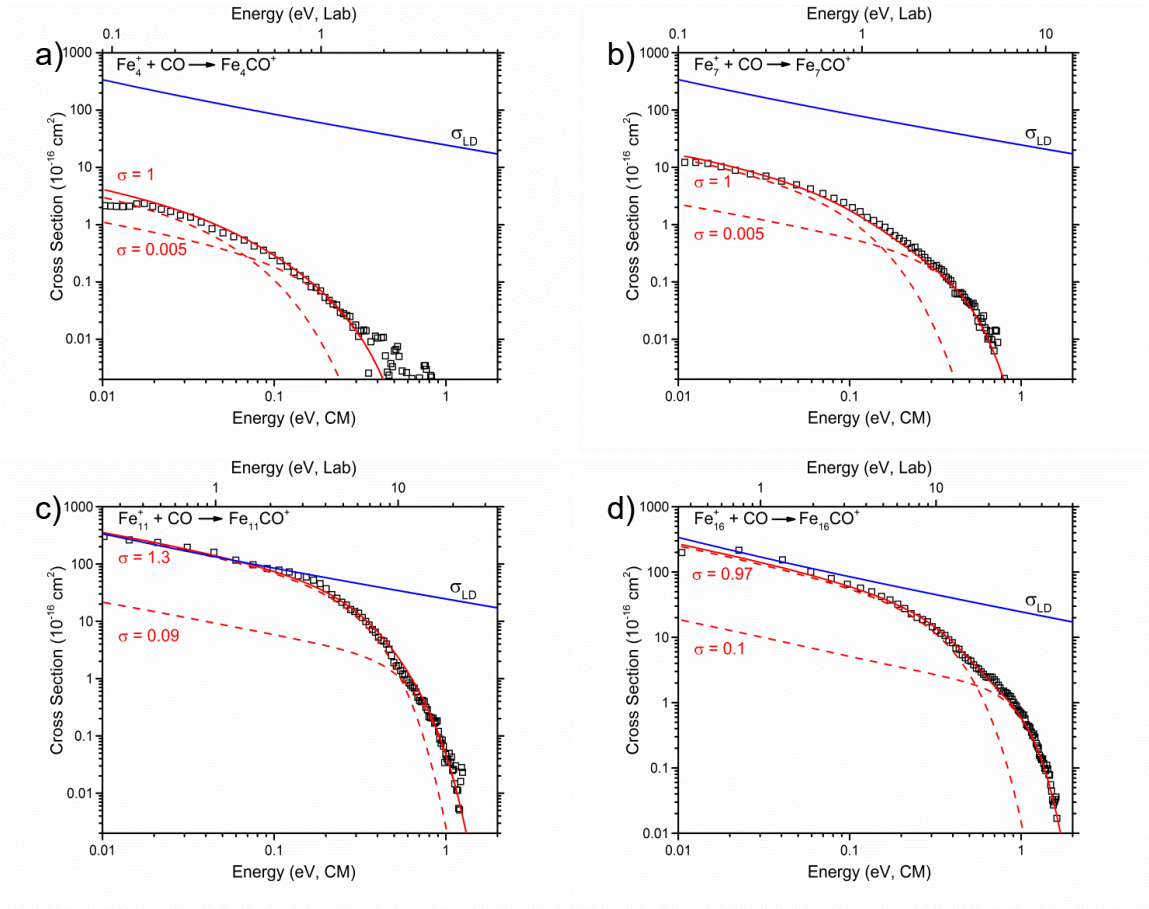

Fig. 6.5. Zero-pressure extrapolated experimental cross sections (symbols) for the association reactions of Fe_4^+, Fe_7^+, Fe_{11}^+, and Fe_{16}^+ (parts a–d) with CO as a function of kinetic energy in the center-of-mass (lower x-axis) and laboratory (upper x-axis) frames. Dashed lines represent the dual model of eqn (6.1) for the primary and secondary features and the red line shows their sum including experimental internal and kinetic energy distributions. The locked dipole cross section, σ_{LD}, eqn (6.3), is also indicated.

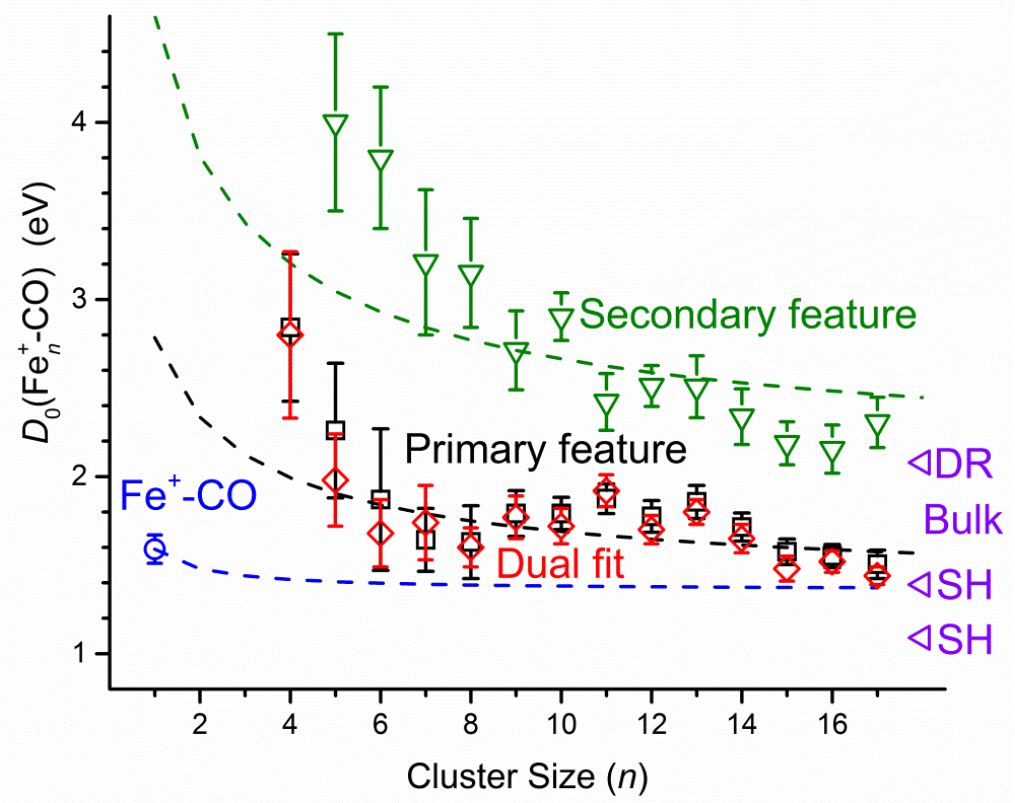

Fig. 6.6. Cluster–CO binding energies for the primary (black squares), primary dual fit (dark red diamonds), and secondary (green triangles) features taken from Table 6.1 and the Fe^+–CO bond strength (blue circle) from Ref. 51. Experimental bulk-phase binding energies, 1.39 (shallow hollow, SH),[53] 1.08 (SH),[54] and 2.08 (dissociative recombination, DR) eV,[53] are indicated by purple triangles to the right. The dashed lines indicate the model of eqn (6.5) normalized to $n_0 = 1$ (blue), $n_0 = 6$ (black), and $n_0 = 9$ (green), see text.

energies, the average value for the n = 11–17 clusters is 2.35 ± 0.14 eV.

Both the primary and secondary values generally decline with increasing n. This can be understood on the basis of a model proposed by Castleman and coworkers.[17] In their studies of the association reactions of CO with cobalt and copper cluster cations, analysis of the observed rates of reaction required the cluster–CO bond strength, E_n, which they estimated using eqn (6.5).

$$E_n = E_{bulk} + \Delta E_{n0}[(r_M n_0^{1/3} + r_{CO})/(r_M n^{1/3} + r_{CO})]^4 \qquad (6.5)$$

This assumes that there is a nearly constant covalent contribution taken to equal E_{bulk}, the bulk-phase bond energy of CO attached to the metal surface, enhanced by a Coulombic term that should vary with the size of the cluster. Eqn (6.5) estimates the latter by using ΔE_{n0}, the difference between the atomic (n_0 = 1) and bulk metal–CO bond strengths, and r_{M} and r_{CO}, the radii of the metal and CO (determined as detailed above). Clearly, the same expression can be normalized to values other than that for the atom by changing n_0 and ΔE_{n0}. This expression leads to calculated cluster–CO bond strengths that always exceed E_{bulk} and should increase as the clusters get smaller, in agreement with the trends in Fig. 6.6.

Fig. 6.6 shows these predicted cluster-CO bond energies starting with E_{bulk} = 1.39 eV and normalized to both n_0 = 1, where $D_0(\text{Fe}_n^+\text{–CO})$ = 1.59 ± 0.08 eV,[51] and the present bond energy for n_0 = 6. Clearly, the atomic–CO bond energy is not representative of those for larger clusters. This is because Fe^+ has a $^6D(4s^13d^6)$ ground state, such that donation of the lone-pair of electrons to iron is inhibited by occupation of the outermost 4s orbital. In contrast, the correlation associated with n_0 = 6 (arbitrarily chosen) represents the overall trend in the cluster-CO bond energies well, with the exception of

the $n = 4$ cluster. Fig. 6.6 also includes the prediction for $E_{bulk} = 2.08$ eV normalized to the high energy feature bond energy for $n_0 = 9$. Again the correlation with the data is reasonable except for the smallest clusters and captures the experimental trend with cluster size. Variations about this general trend are probably related to differences in the detailed structures of the clusters.

6.5.2 Comparison to Bulk Phase Thermochemistry

The trends shown in Fig. 6.6 and quantified by eqn (6.5) require appropriate bond energies for the bulk phase asymptote. Several papers have focused on the binding of CO to the Fe(111) surface. In thinking about these results, it is important to remember that iron forms a bcc lattice such that the (111) surface is fairly open with atoms in the second and third layers being exposed, as shown in Fig. 6.7. Bartosch, Whitman, and Ho (BWH),[52] Whitman *et al.*,[53] and Seip *et al.*[54] used temperature programmed desorption (TPD) and electron energy loss spectroscopy (EELS) to determine how CO adsorbs on a Fe(111) surface as a function of coverage and temperature. BWH found that CO binds to Fe(111) at atop and two different multifold sites, shallow hollow and deep hollow, which are outlined by the red and blue triangles in Fig. 6.7, respectively. The shallow hollow (SH) site was measured to have a binding energy of 1.39 eV, respectively, around 300–400 K.[53] Seip *et al.* found similar binding energies for the atop and shallow hollow sites: 0.91 and 1.08 eV, respectively. For results on the Fe(100) surface, a site like the shallow hollow remains but there can be no deep hollow site. Moon, Dwyer, and Bernasek (MDB)[55] observed CO absorbing molecularly to three sites on an Fe(100) surface, with desorption energies of 0.55, 0.78, and 1.14 eV. Whitman *et al*.[53] suggest that the latter

two studies obtain lower desorption energies because they used Redhead's formula[56] and assumed first-order desorption kinetics with a "normal" frequency factor of 10^{13} s^{-1}. A crucial factor for using Redhead's method is the availability of reliable preexponential factors,[54] which are commonly assumed to be on the order of 10^{13}–10^{15} s^{-1} on the basis of simple transition state theory.[57] Whitman *et al.* conclude that such normal preexponential factors are incorrect in this case and values of 10^{15}–10^{18} s^{-1} should be used for CO desorbing from a Fe surface, thereby leading to the higher desorption energies. The present study validates the higher 1.39 eV value obtained by Whitman *et al.*, as shown in Fig. 6.6. Meanwhile, all three studies found that a secondary activated adsorption mechanism occurs at temperatures above 400 K where adsorbed C and O recombine and then desorb around 800 K. This corresponds to a desorption enthalpy of 2.08–2.17 eV, where the lower value is from Whitman *et al*.

As noted above, the correlation shown in Fig. 6.6 for the primary Fe_n^+-CO bond energies utilizes E_{bulk} = 1.39 eV, the value determined by Whitman *et al.* for the shallow hollow site. A key observation for the purposes of the present study is that at low surface coverages, the shallow hollow and deep hollow sites are occupied on the Fe(111) surface and that the barriers for movement between sites are small, 0.20 ± 0.02 eV. In addition, they find that the sticking probability at the shallow hollow site is about twice that for the deep hollow site. Finally, the deep hollow site corresponds to interaction of CO with Fe atoms in the third layer. BWH[52] calculate that this means the C atom is ~0.4 Å *below* the surface, whereas the shallow hollow places the C atom only ~0.5 Å above the surface with atop sites having metal-C distances of ~1.3 Å.[52] From this, it seems unlikely that small iron clusters have enough structural rigidity or size to support the deep hollow site.

Thus, the correspondence of our data with the bulk-phase desorption energy for the shallow hollow site seems appropriate.

The correlation shown in Fig. 6.6 for the secondary bond energies utilizes E_{bulk} = 2.08 eV, associated with dissociative recombination (DR). There is evidence that the shallow hollow[54,55] and deep hollow sites[52] are the precursors to dissociative chemisorption at room temperature. Seip *et al.* note that occupation of the shallow hollow site disappears upon heating the Fe(111) surface over 350–400 K leading to dissociative chemisorption. Likewise, MDB show that their most strongly bound molecular adsorption site was the precursor to dissociative chemisorption. This process may parallel our observation of the dissociative state observed at higher collision energies. If the hollow sites are required for dissociation, this could explain why the extent of dissociative chemisorption on the clusters is relatively minor, 0.3%–10%, of the total adsorption probability. Clearly, larger clusters have a higher probability of supporting sites that mimic the three-fold symmetries of the hollow sites, Fig. 6.7, thus explaining the general increase in this probability with n, σ_0 values in Table 6.1. Given the 2.08 eV value for dissociative recombination, we can return to the question of whether dissociation channels other than CO loss should be available to a CFe_nO^+ complex. Examination of the $D_0(Fe_{n-1}^+–Fe)$ bond energies for n = 2–18[48] shows that they all exceed 2.4 eV except for n = 3 at 1.67 ± 0.12 eV and n = 4 at 2.11 ± 0.20 eV. Thus, dissociation of CFe_nO^+ by Fe atom loss is unlikely to be competitive with dissociative recombination of CO except for the smallest clusters where the extent of dissociation is a minor channel, < 1%.

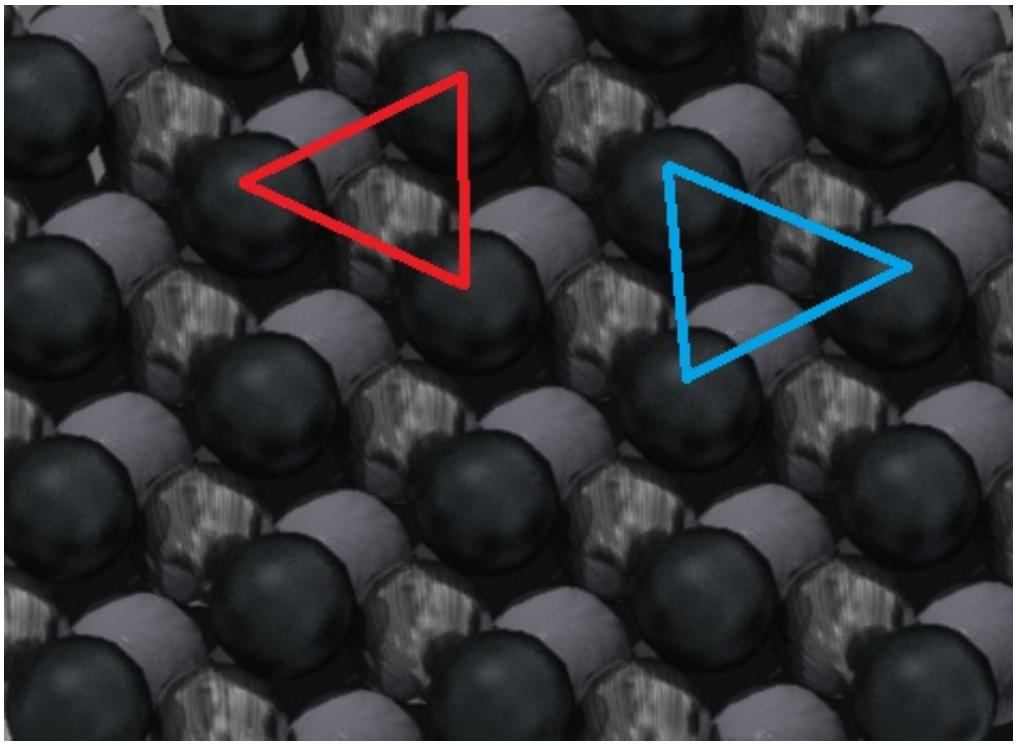

Fig. 6.7. Rendering of a Fe(111) surface according to a base vector length of 4.05 Å from Refs. 53 and 54. This surface exhibits three types of highly symmetric sites: atop (first layer, black), shallow hollow (second layer, silver and outlined by the red triangle), and deep hollow (third layer, gray and outlined by the blue triangle).

6.5.2 Comparison of Gas Phase and Bulk Phase Spectroscopic Measurements

On the basis of the desorption energies, Fig. 6.6 suggests that the primary binding motif for CO to small iron cluster cations is molecular in sites similar to the shallow hollow site on Fe(111). This assignment appears to be in conflict with the infrared multiple photon dissociation (IRMPD) studies of Lyon *et al*.[41] in which they concluded that CO binds to neutral iron clusters only at atop sites. This assignment is based on a C–O stretching frequency of ≈1865 cm^{-1} (with very broad bands, nearly 100 cm^{-1} in full width at half-maximum), which showed little to no change as the cluster size increased from 18–23. They suggested that if CO were to occupy other sites, such as bridge or hollow sites, the C–O stretching frequency should redshift by ~150 cm^{-1} with each additional metal–CO bond,[58] again referring to the Blyholder model.[4] Perhaps importantly, Lyon *et al.* comment that because their experiments did not achieve 100% depletion, 20 – 40% of their clusters could correspond to alternative isomers that do not absorb in the 1775 – 1950 cm^{-1} region examined.

In their studies of the interactions between CO and Fe(111) surfaces, Seip *et al.* observed three CO stretching frequencies of 2000, 1805, and 1530 cm^{-1}, which they assigned to atop, shallow hollow, and deep hollow sites, respectively. These assignments relied on the ranges provided by Sheppard and Nguyen[59] who suggested that CO bound at an atop site should have a vibrational frequency of 2000–2130 cm^{-1}, two-fold sites should have 1880–2000 cm^{-1}, and multifold sites should be 1650–1880 cm^{-1}. Likewise BWH observe CO frequencies ranging from 1760 at low coverages to 1860 cm^{-1} at high coverages that they attribute to the shallow hollow site, noting “that the observed frequency is lower than expected for a twofold bridge” and that the atop site has

frequencies of 1940–2015 cm^{-1}. The deep hollow site is assigned to CO frequencies of 1530–1575 cm^{-1}. As noted above, it is also important to remember that the surface studies find that the shallow hollow site is occupied preferentially at low coverages on Fe(111), with a similar site preferentially occupied on Fe(100). Thus, our single collision studies should match these conditions.

Recapping, Lyon *et al.* concluded CO binds at atop sites on neutral iron clusters,[41] whereas the surface studies concluded that CO prefers to occupy the shallow hollow sites at 300 K and low coverage.[52-55,60] Fig. 6.6 suggests that the iron cluster cations in our experiments behave comparably to the surface. There are two plausible explanations to explain this discrepancy. One is that the ~1865 cm^{-1} band actually does correspond to the CO stretching frequency when bound to a multifold site, as suggested by the ranges given by Sheppard and Nguyen[59] and adopted by BWH and Seip *et al*. Certainly, this frequency falls outside the range for the atop site according to this work, although it is not quite as low as the 1760–1805 cm^{-1} frequency observed on the low-coverage Fe(111) surface. Another explanation focuses on how the CO bound clusters are formed in the two gas-phase experiments. Lyon *et al*. create their iron clusters by pulsed gas laser vaporization followed by introduction of the CO into the clustering region of their source. Clearly, this can lead to multiple collisions, which could lead to CO occupying multiple sites including atop sites as a result of collisional stabilization. This region of multiple collisions may be analogous to the high coverage environment in the surface studies, where the CO prefers occupying atop sites and this stretch dominates the observed spectra. In the present work, bare mass-selected cluster cations are collided with CO under single collision conditions to form the association complex, such that no

stabilization can occur, directly analogous to the low-coverage limit of the surface studies.

6.6 Conclusions

The kinetic energy dependences for the association reaction of CO to bare gas-phase iron cluster cations ranging in size from 4 to 17 atoms are studied using guided ion beam mass spectrometry. The data are analyzed using a model that assumes the lifetimes of the association complexes are limited by passage over a loose, orbiting (PSL) transition state and explicitly conserves orbital angular momentum. This method involves the careful treatments of lifetime effects, kinetic energy distributions of the cluster ion and neutral reactants, reactant internal energy distributions, and angular momentum distributions. The resulting modeled cross sections can reproduce the kinetic energy dependences and absolute magnitudes of our experimental cross sections in detail using only a single adjustable parameter, E_0. For many cluster sizes, there is strong evidence for a second higher energy feature that indicates a separate process, and this feature is independently analyzed as well, although the parameters are no longer constrained as well. The end result is the determination of quantitative binding energies of CO to iron cluster cations for two possible sites.

Comparison of these gas-phase binding energies with bulk-phase measurements[53,55,60] leads to the conclusion that CO primarily occupies a shallow hollow binding site on small iron cluster cations and that the secondary higher energy feature is likely associated with a dissociative chemisorption process. Smaller clusters exhibit larger binding energies than the bulk, which can be explained using a simple Coulomb

model.[17] A good correlation between the asymptotic gas-phase binding energies obtained from this study and those from Whitman *et al*.[53] helps validate their absolute values. Notably, the present values are the first experimentally determined binding energies for CO to gas-phase metal clusters in any charge state. As in many of our previous thermodynamic studies of small cationic transition metal clusters,[5-14] it is perhaps surprising that bulk-phase-like thermochemistry is obtained for such modest sized clusters. As in these previous studies, we rationalize this as a direct consequence that ligand-surface bonds are relatively local phenomena, namely any ligand can bind to only 1–4 surface atoms (of a cluster or the bulk). Once the cluster is sufficiently large to allow adequate electronic "flexibility", the cluster-adsorbate bonds approximate the surface-adsorbate bonds.

6.7 Electronic Supplementary Material

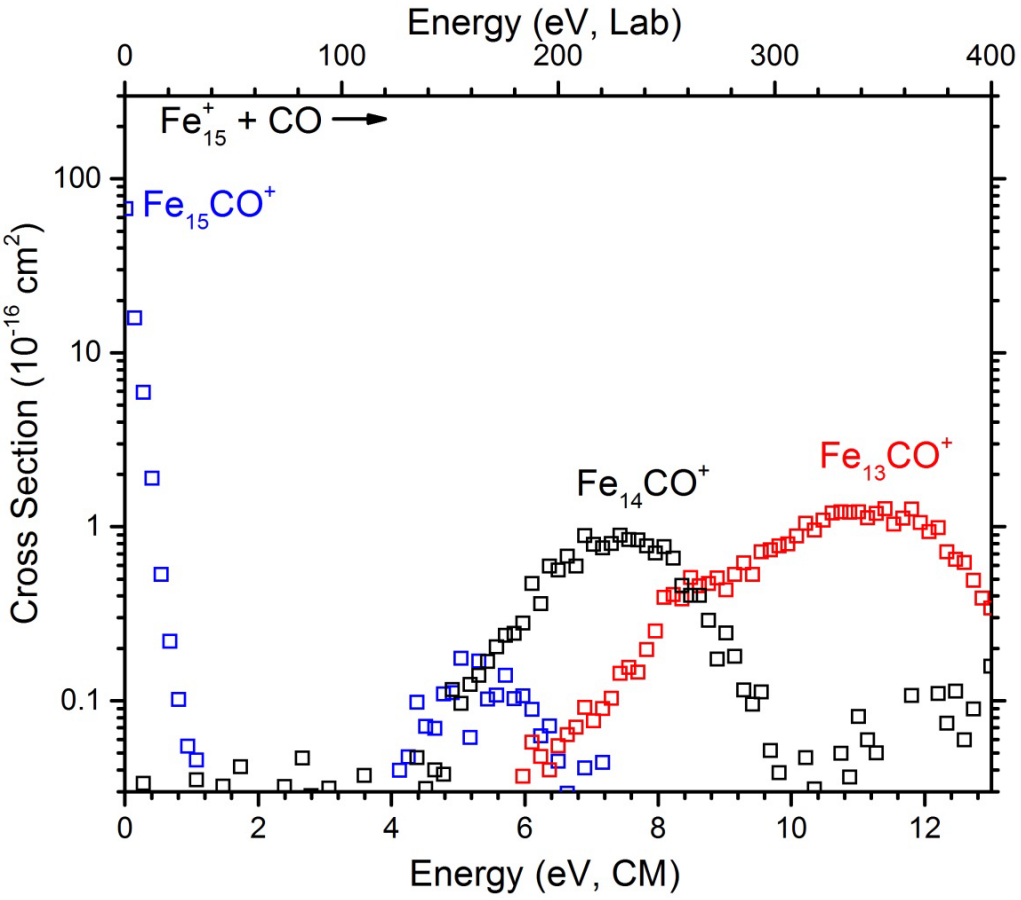

Fig. 6.S1. Experimental cross sections for the reaction of Fe_{15}^+ with CO as a function of kinetic energy in the lab frame (upper axis) and center-of-mass frame (lower axis)

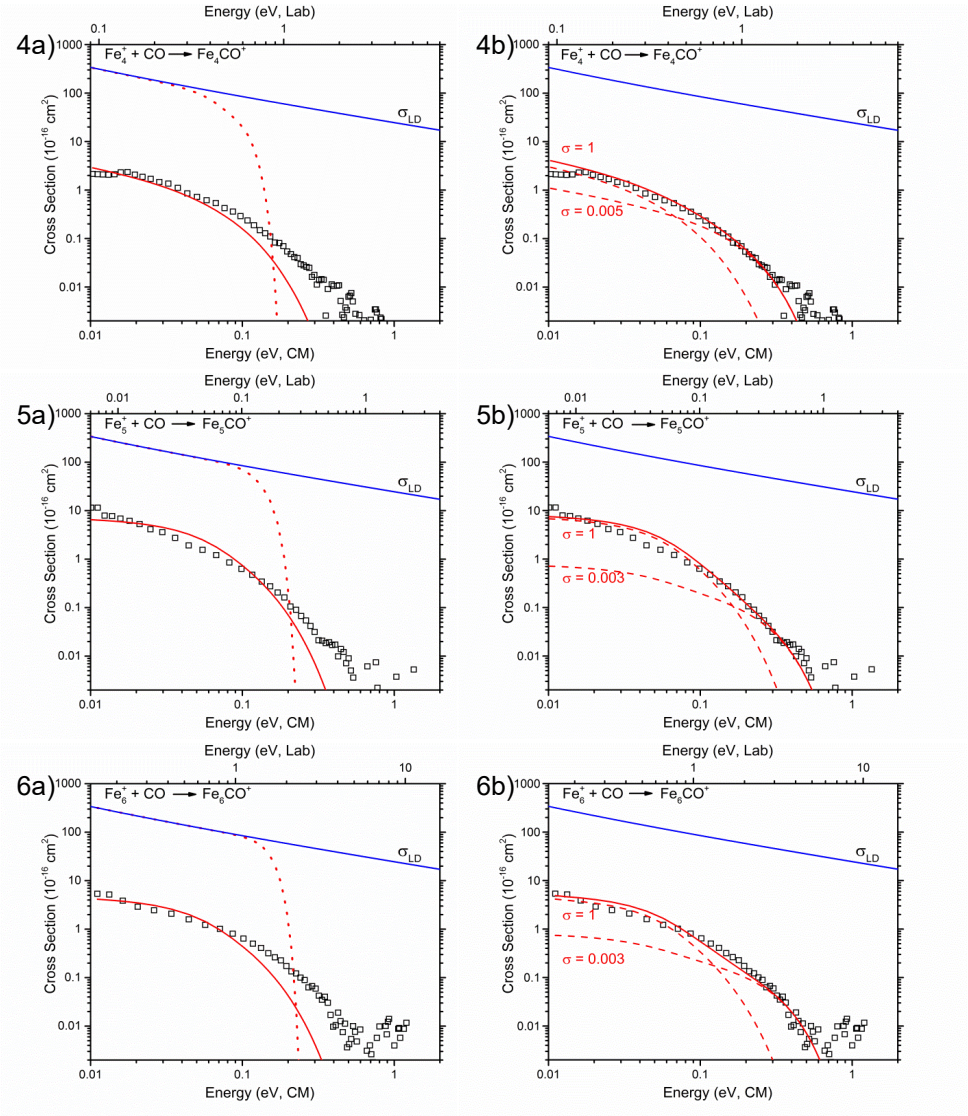

Fig. 6.S2. Zero-pressure extrapolated experimental cross sections (symbols) for the association reactions of Fe_n^+ where n = 4–17 (parts *n*a–*n*b) with CO as a function of kinetic energy in the center-of-mass frame. The red line in parts *n*a is the model of eqn (6.1) using the single model parameters in Table 6.1. Dashed lines in parts *nb* represent models of eqn (6.1) for the primary and secondary features and the red line shows their sum using the dual model parameters in Table 6.1**.** The locked dipole cross section of eqn (6.3) is also indicated.

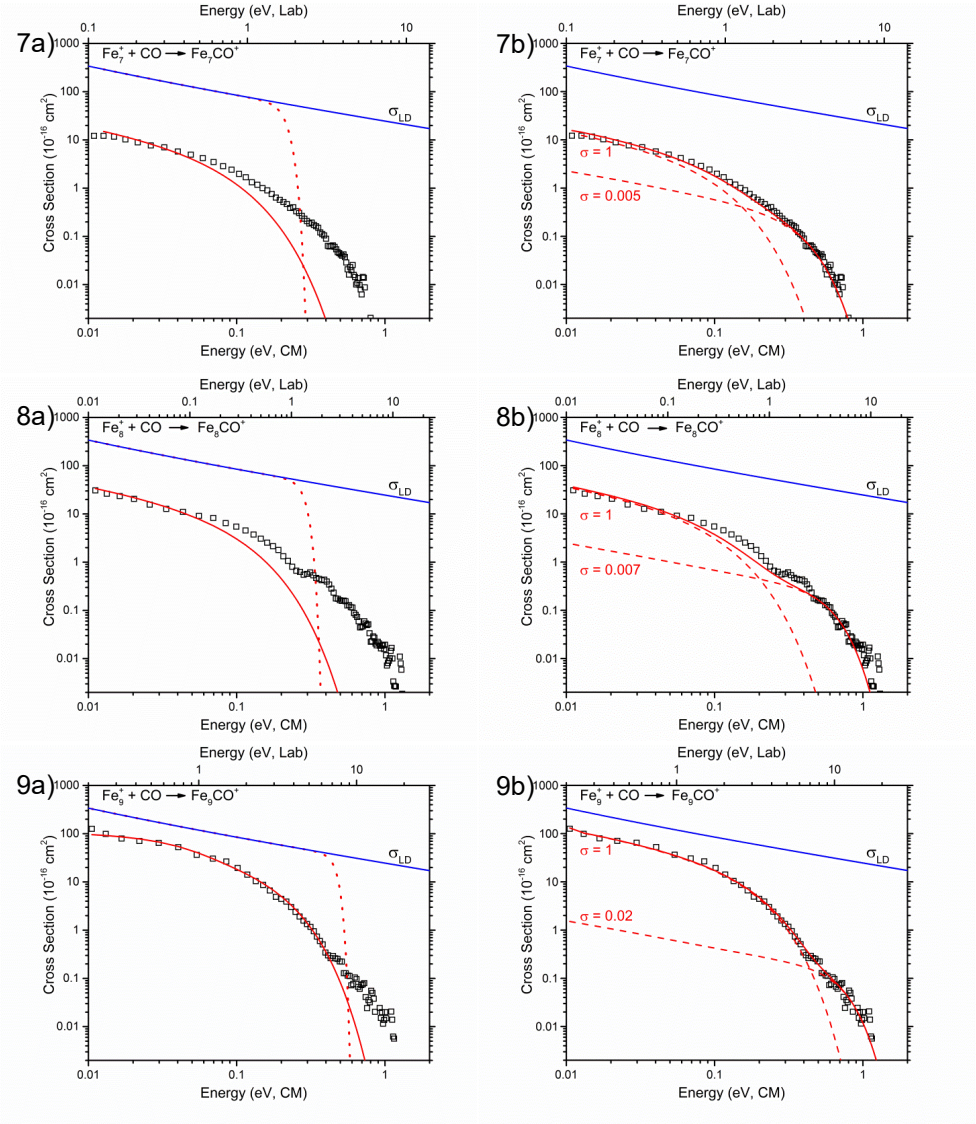

Fig. 6.S2. (Continued)

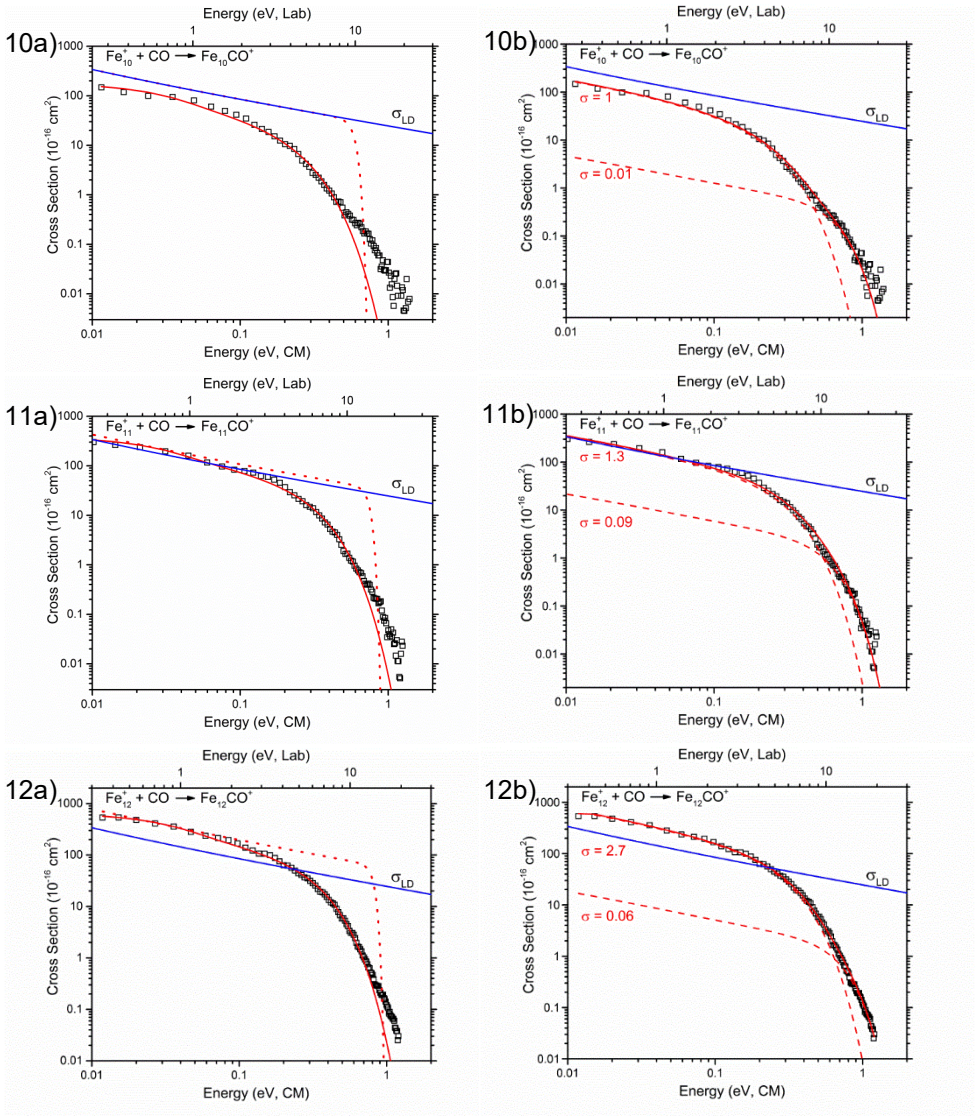

Fig. 6.S2. (Continued)

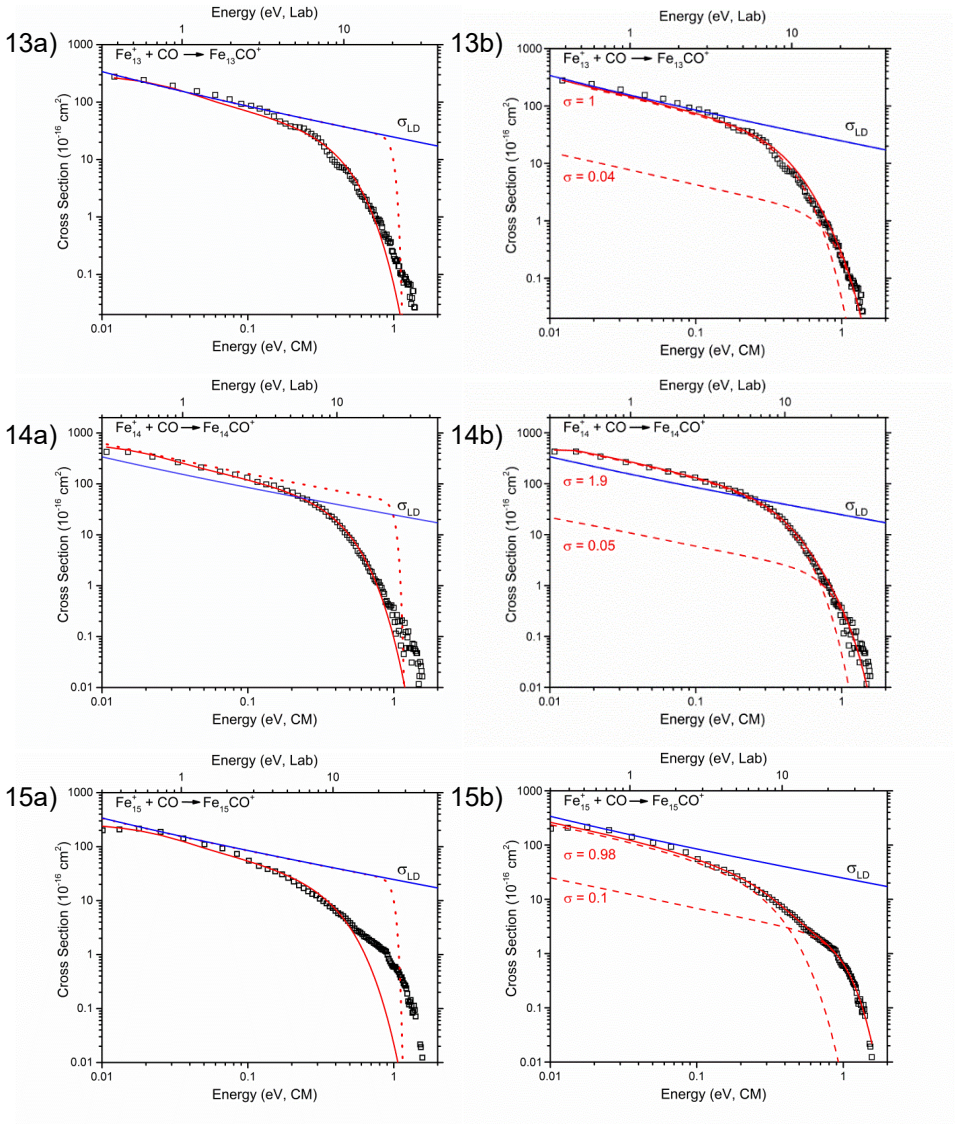

Fig. 6.S2. (Continued)

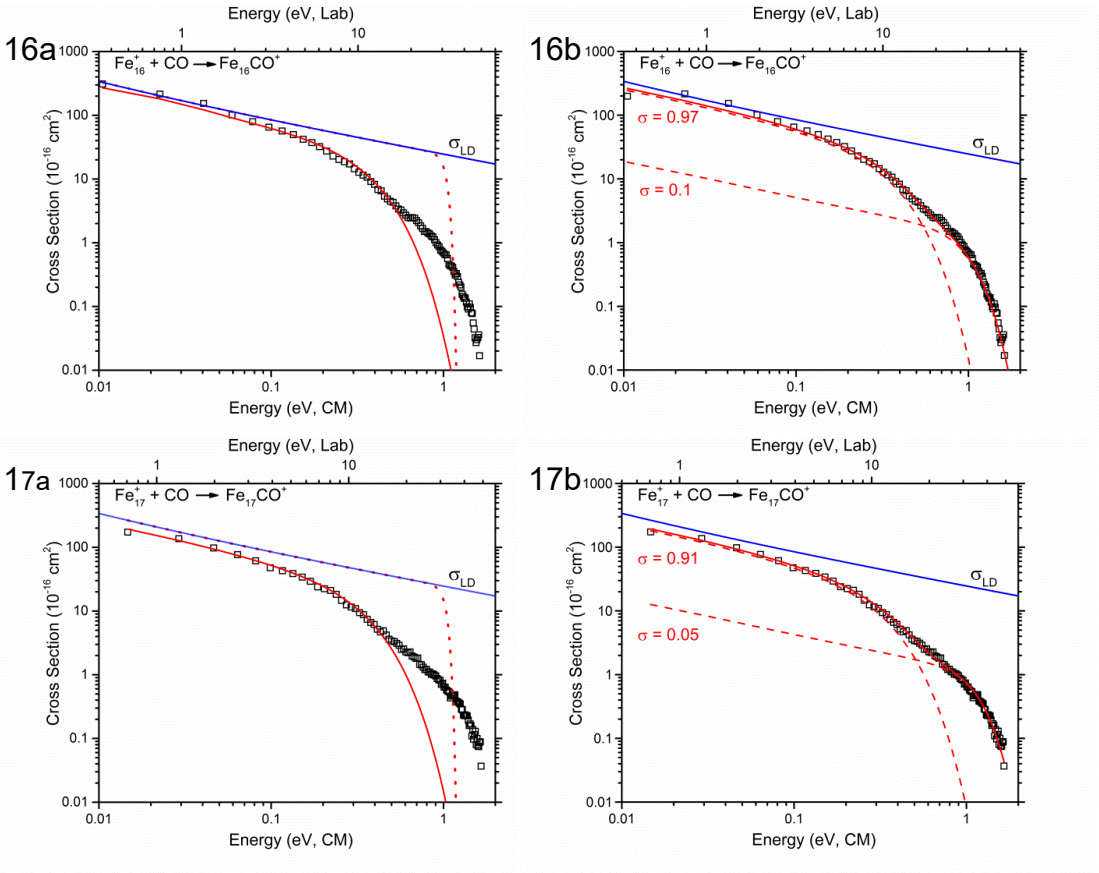

Fig. 6.S2. (Continued)

6.8 References

1. M. E. Dry, *Catal. Today*, 2002, 71, 227.

2. M. J. Bronikowski, P. A. Willis, D. T. Colbert, K. A. Smith and R. E. Smalley, *J. Vac. Sci. Technol., A*, 2001, 19, 1800-1805.

3. P. Plonjes, P. Palm, G. B. Viswanathan, V. V. Subramaniam, I. V. Adamovich, W. R. Lempert, H. L. Fraser and J. W. Rich, *Chem. Phys. Lett.*, 2002, 352, 342-354.

4. G. Blyholder, *J. Phys. Chem.*, 1964, 68, 2772-2777.

5. J. Conceição, S. K. Loh, L. Lian and P. B. Armentrout, *J. Chem. Phys.*, 1996, 104, 3976-3988.

6. J. B. Griffin and P. B. Armentrout, *J. Chem. Phys.*, 1997, 106, 4448-4462.

7. J. B. Griffin and P. B. Armentrout, *J. Chem. Phys.*, 1997, 107, 5345-5355.

8. R. Liyanage, X. G. Zhang and P. B. Armentrout, *J. Chem. Phys.*, 2001, 115, 9747-9763.

9. R. Liyanage, J. B. Griffin and P. B. Armentrout, *J. Chem. Phys.*, 2003, 119, 8979-8995.

10. L. Tan, F. Liu and P. B. Armentrout, *J. Chem. Phys.*, 2006, 124, 084302-084301-084314.

11. P. B. Armentrout, *Eur. J. Mass Spectrom.*, 2003, 9, 531-538.

12. P. B. Armentrout, *Ann. Rev. Phys. Chem.*, 2001, 52, 423-461.

13. P. B. Armentrout, in *Nanoclusters: A Bridge across Disciplines*, eds. P. Jena and A. W. Castleman, Elsevier, Amsterdam, 2010, pp. 269-297.

14. P. B. Armentrout, *Caalt. Sci. Tech.*, 2014, 4, 2741-2755

15. H. Koizumi and P. B. Armentrout, *J. Chem. Phys.*, 2003, 119, 12819-12829.

16. D. M. Cox, K. C. Reichmann, D. J. Trevor and A. Kaldor, *J. Chem. Phys.*, 1988, 88, 111-119.

17. R. E. Leuchtner, A. C. Harms and A. W. Castleman Jr., *J. Chem. Phys.*, 1990, 92, 6527-6537.

18. B. C. Guo, K. P. Kerns and A. W. Castleman Jr., *J. Chem. Phys.*, 1992, 96, 8177-8186.

19. E. K. Parks, K. P. Kerns and S. J. Riley, *J. Chem. Phys.*, 2000, 112, 3384-3393.

20. E. K. Parks, K. P. Kerns and S. J. Riley, *J. Chem. Phys.*, 2000, 112, 3394-3407.

21. I. Balteanu, U. Achatz, O. P. Balaj, B. S. Fox, M. K. Beyer and V. E. Bondybey, *Int. J. Mass Spectrom.*, 2003, 229, 61-65.

22. G. Kummerlowe and M. K. Beyer, *Int. J. Mass Spectrom.*, 2005, 244, 84-90.

23. K. M. Ervin and P. B. Armentrout, *J. Chem. Phys.*, 1985, 83, 166-189.

24. S. K. Loh, D. A. Hales and P. B. Armentrout, *Chem. Phys. Lett.*, 1986, 129, 527-532.

25. S. K. Loh, D. A. Hales, L. Lian and P. B. Armentrout, *J. Chem. Phys.*, 1989, 90, 5466-5485.

26. D. Gerlich, *Adv. Chem. Phys.*, 1992, 82, 1-176.

27. N. R. Daly, *Rev. Sci. Instrum.*, 1960, 31, 264-267.

28. M. T. Rodgers, K. M. Ervin and P. B. Armentrout, *J. Chem. Phys.*, 1997, 106, 4499-4508.

29. P. B. Armentrout, K. M. Ervin and M. T. Rodgers, *J. Phys. Chem. A*, 2008, 112, 10071-10085.

30. W. J. Chesnavich and M. T. Bower, *J. Am. Chem. Soc.*, 1976, 98, 8301-8309.

31. T. Beyer and D. F. Swinehart, *Comm. ACM*, 1973, 16, 379.

32. S. E. Stein and B. S. Rabinovitch, *J. Chem. Phys.*, 1973, 58, 2438-2445.

33. A. A. Shvartsburg, K. M. Ervin and J. H. Frederick, *J. Chem. Phys.*, 1996, 104, 8458-8470.

34. G. A. Parker and R. T. Pack, *J. Chem. Phys.*, 1976, 64, 2010-2012.

35. J. S. Muenter, *J. Mol. Spectrosc.*, 1975, 55, 490-491.

36. R. G. Gilbert and S. C. Smith, *Theory of Unimolecular and Recombination Reactions*, Blackwell Scientific, London, 1990.

37. P. J. Robinson and K. A. Holbrook, *Unimolecular Reactions*, Wiley Interscience, New York, 1972.

38. D. G. Truhlar, B. C. Garrett and S. J. Klippenstein, *J. Phys. Chem.*, 1996, 100, 12771-12800.

39. G. L. Gutsev and C. W. Bauschlicher Jr., *J. Phys. Chem. A*, 2003, 107, 7013-7023.

40. G. L. Gutsev, C. W. Bauschlicher and L. Andrews, *J. Chem. Phys.*, 2003, 119, 3681-3690.

41. J. T. Lyon, P. Gruene, A. Fielicke, G. Meijer and D. M. Rayner, *J. Chem. Phys.*, 2009, 131, 184706-184701-184707

42. D. A. Hales, L. Lian and P. B. Armentrout, *Int. J. Mass Spectrom. Ion Processes*, 1990, 102, 269-301.

43. G. Gioumousis and D. P. Stevenson, *J. Chem. Phys.*, 1958, 29, 294.

44. T. Su and M. T. Bower, *Gas Phase Ion Chemistry*, Academic, New York, 1979.

45. T. Su and M. T. Bowers, *Int. J. Mass Spectrom.*, 1973, 12, 347-356.

46. T. Su, *J. Chem. Phys.*, 1994, 100, 4703-4703.

47. *CRC Handbook of Chemistry and Physics*, CRC Press, Boca Raton, 2002.

48. L. Lian, C. X. Su and P. B. Armentrout, *J. Chem. Phys.*, 1992, 97, 4072-4083.

49. S. Peredkov, M. Neeb, W. Eberhardt, J. Meyer, M. Tombers, H. Kampschulte and G. Niedner-Schatteburg, *Phys. Rev. Lett.*, 2011, 107, 233401.

50. M. Niemeyer, K. Hirsch, V. Zamudio-Bayer, A. Langenberg, M. Vogel, et al., *Phys. Rev. Lett.*, 2012, 108, 057201.

51. R. H. Schultz, K. C. Crellin and P. B. Armentrout, *J. Am. Chem. Soc.*, 1991, 113, 8590-8601.

52. C. E. Bartosch, L. J. Whitman and W. Ho, *J. Chem. Phys.*, 1986, 85, 1052-1060.

53. L. J. Whitman, L. J. Richter, B. A. Gurney, J. S. Villarrubia and W. Ho, *J. Chem. Phys.*, 1989, 90, 2050-2062.

54. U. Seip, M.-C. Tsai, K. Christmann, J. Küppers and G. Ertl, *Surf. Sci.*, 1984, 139, 29-42.

55. D. W. Moon, S. L. Bernasek, J. P. Lu, J. L. Gland and D. J. Dwyer, *Surf. Sci.*, 1987, 184, 90-108.

56. P. A. Redhead, *Vac.*, 1962, 12, 203-211.

57. E. G. Seebauer, A. C. F. Kong and L. D. sSchmidt, *Surf. Sci.*, 1988, 193.

58. A. Fielicke, P. Gruene, G. Meijer and D. M. Rayner, *Surf. Sci.*, 2009, 603, 1427-1433.

59. N. Sheppard and T. T. Nguyen, *in: Advances in Infrared and Raman Spectroscopy*, Heyden, London, 1978.

60. D. C. Sorescu, D. L. Thompson, M. M. Hurley and C. F. Chabalowshi, *Phy. Rev. B*, 2002, 66, 035416-035411-035413.